Gamma-ray spectroscopic studies of ^{155}Ho and ^{156}Er

Thesis submitted in accordance with the requirements of the University of Liverpool for the degree of Doctor in Philosophy

by

Joseph Michael Rees

Department of Physics

January 2014

Abstract

Excited states in ^{155}Ho and ^{156}Er extending to high spin have been populated as part of two experiments performed at the ATLAS facility of Argonne National Laboratory. In both experiments high-fold γ-ray coincidence data were recorded in a high-statistics experiment with the Gammasphere spectrometer.

In $^{156}_{68}\mathrm{Er}_{88}$, weakly populated band structures have been established at low to medium spins, following the ^{114}Cd(^{48}Ca,6nγ) reaction at 215 MeV. Bands built on the second 0^+ state and 2^+ (γ-vibrational) states have been established. A large staggering between the even- and odd-spin members of the γ-vibrational band suggests a γ-soft nature of this nucleus. An additional band is discussed as being based on a rotationally aligned $\nu h_{9/2}/f_{7/2}$ structure, coexisting with the systematically observed, more favourable $(\nu i_{13/2})^2$ alignment seen in this mass region. At high spin, new transitions above the 42^+ terminating state have been observed, establishing the presence of a further excited state, which is interpreted as the predicted terminating 46^+ state built on a $\pi(d_{5/2}/g_{7/2} \rightarrow d_{3/2})$ particle-hole excitation across the $Z = 64$ shell gap.

New states in $^{155}_{67}\mathrm{Ho}_{88}$ have been observed following the ^{124}Sn(^{37}Cl,6nγ) reaction at 180 MeV. At low spin, a positive-parity $\pi g_{7/2}$ rotational band, observed for the first time in this nucleus, has been established up to $(33/2^+)$. The $\pi h_{11/2}$ band has been extended to higher spins, and the large signature splitting it exhibits interpreted as evidence of triaxiality at low spin. In addition, a positive-parity rotational structure has been extended to $I^\pi = 57/2^-$ and discussed as being based on a $\nu(i_{13/2}h_{9/2})$ structure coupled to the $h_{11/2}$ proton. $B(M1)/B(E2)$ ratios of reduced transition probabilities have been calculated from observed branching ratios for all three bands and compared with theoretical calculations for specific particle configurations. Above spin $\sim 59/2$ the behaviour of the nucleus is discussed in the context of band termination. An energetically favoured state at $I^\pi = 79/2^-$ has been established, which corresponds to valence-space band termination in ^{155}Ho. Weak, high-energy core-breaking excitations feeding this state have been observed. New states with $I^\pi = (87/2^+), (89/2^+)$ are thought to be further predicted favoured terminating states at oblate shape, built on $\pi(d_{5/2}/g_{7/2} \rightarrow h_{11/2})$ particle-hole excitations across the $Z = 64$ shell gap. The newly observed high-spin states are compared to Cranked Nilsson Strutinsky calculations, and presented in the context of known band terminating states in the region.

Contents

Acknowledgements

I would like to express my deep appreciation to the all the people who made this effort possible: my supervisors Eddie Paul and Andy Boston; John Simpson at STFC Daresbury and Mark Riley at Florida State University; Ingemar Ragnarsson at Lund for performing the theoretical calculations; and the people at the ATLAS facility of Argonne National Laboratory where the experiments were performed, as well as all the members of our collaboration.

Many thanks to past and present members of the Nuclear Structure group at the University of Liverpool for all their support, and special thanks to those of you I now count amongst my best friends.

Thank you to my family, especially Joanne Rees for putting up with the perpetual student that is her son.

Finally, I am very grateful to the STFC for funding my research.

Chapter 1

Introduction

This thesis documents γ-ray spectroscopic studies of two nuclides: erbium-156 ($^{156}_{68}\mathrm{Er}_{88}$), and holmium-155 ($^{155}_{67}\mathrm{Ho}_{88}$). In two separate but similar experiments they were produced in highly excited states following fusion-evaporation reactions. During the rapid decay to their stable ground states they occupied many discrete states of decreasing energy and angular momentum, and the γ rays emitted during this process were detected using the Gammasphere spectrometer and subsequently analysed. In this way, the states the nuclei occupied during their decay were recreated schematically in the form of level schemes. Information about the quite varied behaviour of the nuclides can be gleaned from these level schemes, of which Fig. 1.1 is an example, from a previous study of ^{155}Ho [1]. Nuclear structure models and calculations inform this process of interpretation of the observed states, and in turn, the new experimental information provides a test for these models. The development over recent decades of large germanium detector arrays like the Gammasphere has brought ever higher spin states, and other similarly weakly populated structures, into the realm of experimental sensitivity [2].

The nuclide ^{156}Er was already known to exhibit a large assortment of excitations, which included: rotational alignments due to the breaking of nucleon pairs; several

rotational bands built on various neutron configurations; a rotational band coupled to the γ-vibration, established from spin $16\hbar$ to $28\hbar$; a favoured 42^+ terminating state, and several core-breaking excitations above it; and even evidence for octupole collectivity [3]. The work presented here contributes even more modes of excitation to this growing list [4]. A band built on the second 0^+ state, i.e. what is often referred to as the β-vibrational band, has been established up to spin (22^+). Previously, the low spin levels of the γ-vibrational band were not well known; both the even- and odd- spin members of this band have now been been established. Their relative energies suggest that the nucleus is 'soft' to axially asymmetric, or 'triaxial', shapes. Another newly observed band is discussed as being based on a rotationally aligned $\nu h_{9/2}/f_{7/2}$ structure not typically seen in this mass region.

States of spins the highest reported to date in ^{155}Ho and ^{156}Er have been seen, revealing aspects of their behaviour at valence-space band termination. The way in which the atomic nucleus generates excited states and increasing angular momentum represents a delicate interplay between single-particle and collective degrees of freedom, and the phenomenon of band termination is a good example of this [5]. It is tempting to think of the generation of angular momentum through collective rotation as separate from the behaviour of individual nucleons inhabiting specific shells, that while a rotational band may be built on a particular orbital, the single particle contribution to the total angular momentum is limited to the K contribution of the band-head. Band termination shows this not to be the case. Outside the spherical core, a nucleus has a limited number of valence nucleons. The nuclides being studied here, ^{155}Ho and ^{156}Er, have outside the ^{146}Gd core only nine and ten valence nucleons, respectively. As the maximum spin achievable by filling specific shell orbitals with these valence nucleons comes close to being reached, the ascent to high spin is marked by an often abrupt loss in collectivity, culminating in terminating states with the maximum allowed value of spin [6, 7]. Above the terminating

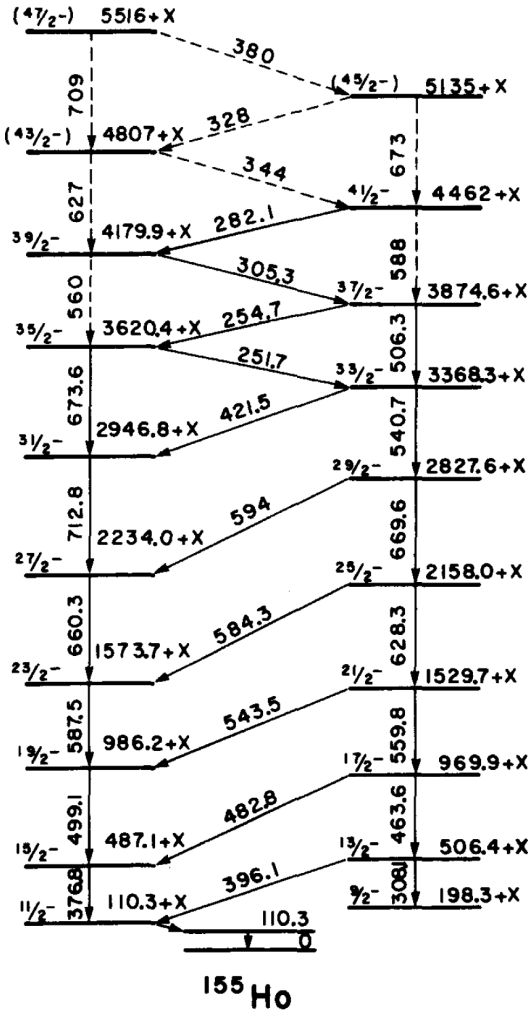

FIGURE 1.1: Level scheme for ^{155}Ho published by Hagemann *et al.* [1]

states particle-hole excitations of the spherical nuclear core can generate states of higher angular momentum, but these core-excited configurations can be energetically expensive, characterized by high energy transitions (∼1–2.5 MeV) feeding the favoured terminating states. In heavy nuclei, evidence for band termination was first seen in nuclei around ^{155}Ho and ^{156}Er [7-11] and in recent years high-energy transitions feeding the terminating states in ^{156,157,158}Er have been reported [12, 13]. Similar transitions have been seen feeding the newly established $79/2^-$ terminating state in ^{155}Ho.

In addition to these terminating states and core-breaking excitations at high spin, the rest of the ^{155}Ho level scheme has also been extended considerably. Two competing rotational bands built on single-proton configurations are seen, and evidence is presented for these configurations of the nucleus having different shapes at low spin, one being axially symmetric, the other favouring triaxial deformation. Other bands, too, are discussed in terms of specific proton and neutron configurations. These configurations are tested through the comparison of measured $B(M1)/B(E2)$ ratios of reduced transition probabilities to geometric calculations [14].

In the next chapter an introduction is given to the physics concepts discussed in this thesis. This is followed in Chapter 3 with a description of the experimental techniques employed to gather the γ-ray coincidence data analysed in this work. Also detailed in Chapter 3 are the methods used to build the level schemes and determine the spins and parities of the deduced states. The two nuclei of interest, ^{156}Er and ^{155}Ho, are then addressed in turn in Chapters 4 and 5. The analysis of the γ-ray data is discussed, as is the subsequent interpretation of the excited states that have been established. Calculations and predictions based on various models will be presented, and systematic trends in behaviour in this region of the nuclear chart will be explored.

Chapter 2

Physics Background

In studying the γ-ray decays of states in ^{156}Er and ^{156}Ho, new excited structures have been revealed. It is the aim of this thesis to use this new information to better understand the structure of these nuclides. The complexity of the nuclear system, which can consist of hundreds of interacting particles (i.e. protons and neutrons) means that mathematical models which simplify the problem usually form the basis of any theoretical approach. A brief introduction to some of these models will be given here, and the simple assumptions upon which they are based explained. No single model describes all kinds of nuclear excitations. Even within an individual nuclide, there can be seen several types on behaviour best described by multiple models. Those relevant to this work concern collective excitations of the nucleus, namely rotation and vibration, as well as single-particle behaviour, which is discussed in terms of shell models.

2.1 Shapes

Much of the discussion in this thesis, and in the field of nuclear structure studies in general, concerns the shape of the atomic nucleus. Both nuclides studied in this work

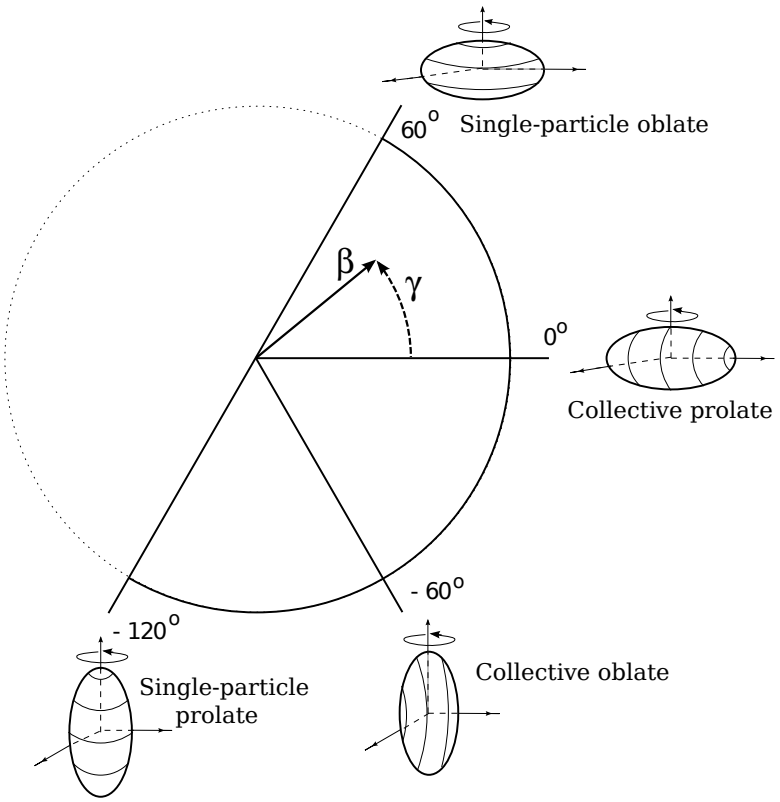

FIGURE 2.1: The Lund convention.

are discussed in terms of the *prolate*, *oblate* and *triaxial* shapes they are thought to adopt at different excitation energies and spins. Accordingly, these terms will be briefly explained and their geometric description given.

The shape of a nucleus can be described as a surface $R(\theta, \phi)$ and expressed as a sum over spherical harmonics, $Y_{\lambda\mu}(\theta, \phi)$,

$$R(\theta, \phi) = C(\alpha_{\lambda\mu}) R_0 \left[1 + \sum_{\lambda=0}^{\infty} \sum_{\mu=-\lambda}^{\lambda} \alpha_{\lambda\mu} Y_{\lambda\mu}(\theta, \phi) \right]. \tag{2.1}$$

The distortion from a spherical shape of radius R_0 is represented by the α coefficients. In reality many nuclides are deformed, having a prolate, 'rugby ball', or oblate, 'discus', shape. Given such a deformed but axially symmetric shape, limited to quadrupole and hexadecapole ($\lambda = 2, 4$) degrees of freedom with $\mu = 0$,

the description of the nuclear shape can be simplified in terms of β_λ deformation parameters. Eq. 2.1 then becomes

$$R(\theta) = C(\alpha_{\lambda\mu})R_0 \left[1 + \sqrt{\frac{5}{4\pi}}\beta_2 P_2(\cos\theta) + \sqrt{\frac{9}{4\pi}}\beta_4 P_4(\cos\theta)\right], \tag{2.2}$$

where the P_λ terms are Legendre polynomials, and the C term satisfies the condition of conservation of volume.

Axially asymmetric or, more specifically, triaxial shapes are also considered in this thesis. A triaxial shape has three principal axes; x, y, z, where $x \neq y \neq z$. Prolate and oblate shapes can be thought of as special cases where $x = y < z$ and $x = y > z$, respectively. To account for triaxial shapes, Eq. 2.1 can be written as

$$R = C(\alpha_{\lambda\mu})R_0 \left[1 + \sqrt{\frac{5}{16\pi}}\beta_2\{3\cos\gamma(3\cos^2\theta - 1) + \sqrt{3}\sin\gamma\sin^2\theta\cos 2\phi\}\right], \tag{2.3}$$

where β_2 is the deformation parameter, and γ is a measure of the triaxiality of the nucleus, determining the lengths along the three principal axes:

$$\begin{aligned}
\delta R_x &= \sqrt{\frac{5}{4\pi}}\beta_2 R_0 \cos(\gamma - \frac{2\pi}{3}), \\
\delta R_y &= \sqrt{\frac{5}{4\pi}}\beta_2 R_0 \cos(\gamma - \frac{4\pi}{3}), \\
\delta R_z &= \sqrt{\frac{5}{4\pi}}\beta_2 R_0 \cos(\gamma).
\end{aligned} \tag{2.4}$$

Prolate shapes have $\gamma = 0°$, and $\gamma = 60°$ describes an oblate shape. Values of γ between these limits correspond to triaxiality. In the Lund convention [15] of Fig. 2.1, the range of γ values is extended to $-120° \leq \gamma \leq 60°$, and the value also indicates about which axis the nucleus rotates; short, intermediate, or long. For example, in the $0° \leq \gamma \leq 60°$ regime, the nucleus rotates about the short axis, and in the $-60° \leq \gamma \leq 0°$ (or collective regime) it rotates about the intermediate axis.

2.2 The shell model

In certain measurable properties of nuclei, sharp discontinuities are seen at particular numbers of protons, Z, and neutrons, N. By contrast, the semi-empirical mass formula of the liquid drop model predicts that these properties should evolve smoothly with increasing mass [16]. For example, nuclei with a 'magic' number of protons or neutrons or both have higher binding energies than would otherwise be expected. The magic numbers are

$$2,\ 8,\ 20,\ 28,\ 50 \text{ and } 82,$$

and are understood to represent energy gaps between clusters, or shells, of discrete energy levels. The idea is analogous to the closed shells of atomic theory, which give rise to periodic trends in chemistry, such as the particularly stable noble gases. In atomic theory, discrete orbitals, and closed shells, appear when each electron is treated as moving, independently of the other electrons, in a Coulomb potential set up by the positive charge of the nucleus.

For the nucleons themselves, the situation is complicated slightly by the fact that the forces they experience are due to *other nucleons*. This problem is overcome by ignoring the interactions between individual nucleons, and approximating the net attractive force of the other nucleons as a *mean field* potential. The exact form this potential takes will now be considered.

2.2.1 The Simple Harmonic Oscillator potential

As a starting point, a simple approximation of the mean field potential is the Harmonic Oscillator potential, which is given by

$$V_{osc} = \tfrac{1}{2} m\omega_0^2 r^2, \tag{2.5}$$

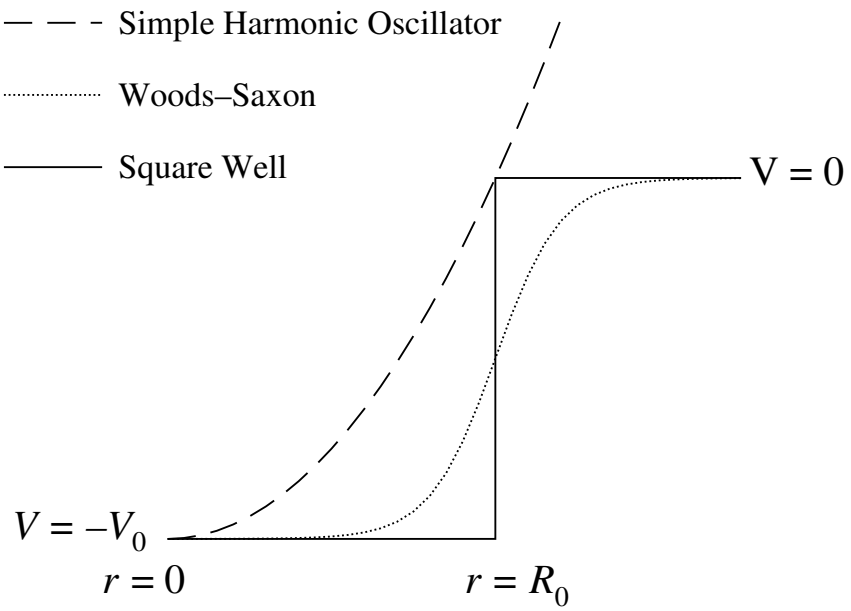

FIGURE 2.2: Comparison between a Simple Harmonic Oscillator of the form $V(r) = -V_0[1-(r/R_0)^2]$, a Woods-Saxon of the form given in Eq. 2.10, and a square well potential.

where r is the distance from the centre of the potential, m is mass, and ω_0 is the Harmonic Oscillator frequency. In order to calculate the energy levels produced by this potential the Hamiltonian must be solved. After incorporating the oscillator potential $V_{osc}(r)$, the Hamiltonian becomes

$$H = -\frac{\hbar^2}{2M}\Delta + \frac{1}{2}m\omega_0^2 r^2, \tag{2.6}$$

where the first term is the kinetic energy of a single nucleon. The energy eigenvalues are given by

$$E_N = (N + \tfrac{3}{2})\hbar\omega_0, \quad N \leq 0 \tag{2.7}$$

where N is the oscillator quantum number. The energy levels are evenly spaced, and each level consists of multiple eigenstates, i.e. they are degenerate. The degeneracy is given by $(N + 1)(N + 2)$. With respect to a reflection of spatial coordinates through the origin, the wavefunctions of even-N solutions are symmetric, and odd-

N solutions antisymmetric. In other words, the levels have alternating parity, given by

$$\pi = (-1)^N = (-1)^\ell. \tag{2.8}$$

The principal quantum number, n, and the angular momentum quantum number, ℓ, define the harmonic oscillator orbital, and their allowed values are governed by the rules

$$2(n-1) + \ell = N, \quad N \geq 0, \quad 0 \leq \ell \leq N. \tag{2.9}$$

The levels for N = 1-6 are shown in Fig. 2.3, labelled with their constituent $n\ell$ degenerate orbitals.

Though the first three magic numbers, 2, 8, and 20 are reproduced by the Harmonic Oscillator potential, it is not a good description of the actual nuclear potential, and fails to reproduce the higher magic numbers. A more realistic potential lies somewhere between the square well and the harmonic oscillator. In nuclei much larger than the range R_N of the nuclear force ($\sim$1 fm), a nucleon towards the centre should experience no net force and as such, away from the surface of the nucleus, the potential is expected to be flat. A central attraction will be felt at the boundary, where the local distribution of nucleons is less symmetric.

In these terms, it is easy to see why the Woods-Saxon potential in Fig. 2.2 better reproduces nuclear properties. The Woods-Saxon potential is defined as

$$V_{\text{W.S.}} = \frac{-V_0}{1 + \exp[\frac{r-R_0}{a}]}, \tag{2.10}$$

where a represents the surface diffuseness. A Woods-Saxon potential is often used in shell model calculations, and has been used in Chapter 5 of this thesis, as the basis of cranked shell model calculations [17, 18]. Another common approach is to apply modifications to the Harmonic Oscillator potential, namely the addition of $\mathbf{l}\cdot\mathbf{s}$

and $\mathbf{l^2}$ terms to the potential [19, 20]. These modifications are described in the next section.

2.2.2 The Modified Harmonic Oscillator potential

The Modified Harmonic Oscillator (MHO) potential represents an improvement to the harmonic oscillator, introducing additional terms to make it more realistic, so that

$$V_{MHO} = \tfrac{1}{2}m\omega_0^2 r^2 - \kappa\hbar\omega_0 \left[2\mathbf{l}\cdot\mathbf{s} + \mu(\mathbf{l}^2 - \langle\mathbf{l}^2\rangle_N)\right]. \tag{2.11}$$

The κ and μ parameters are adjustable and determine the strength of the $\mathbf{l}\cdot\mathbf{s}$ (spin-orbit) and $\mathbf{l^2}$ interactions. The exact values used are based on empirical observations, and usually depend on the region of the nuclear chart being investigated. In this work the $A = 150$ κ and μ parameters of Ref. [21] have been used. The oscillator frequency, ω_0, is defined as

$$\hbar\omega_0 = 41A^{-1/3}\left(1 \pm \frac{N-Z}{3A}\right) \text{ MeV}. \tag{2.12}$$

The $\mathbf{l^2}$ term has the effect of modifying the shape of the potential to something that resembles a Woods-Saxon potential, flattening it out. It lifts the degeneracy of the N shells, with higher-ℓ orbitals being affected more, and thus being lowered more in energy.

Nucleons have an intrinsic angular momentum $\mathbf{s}$ of magnitude $\frac{1}{2}$, and can be aligned or anti-aligned with $\mathbf{l}$. The two sum together to give the total angular momentum j, so that $j = \ell \pm s$. The spin-orbit $\mathbf{l}\cdot\mathbf{s}$ term is attractive but affects $j = \ell + \frac{1}{2}$ and $j = \ell - \frac{1}{2}$ differently, resulting in more tightly bound $j = l+1$ states. As can be seen in Fig. 2.3 the $\mathbf{l}\cdot\mathbf{s}$ term has the effect of breaking the degeneracy of each nl orbital into their $j = \ell + \frac{1}{2}$ and $j = \ell - \frac{1}{2}$ components. The effect can be sufficiently large for some orbitals to 'intrude' into the lower N shells, in the process giving rise

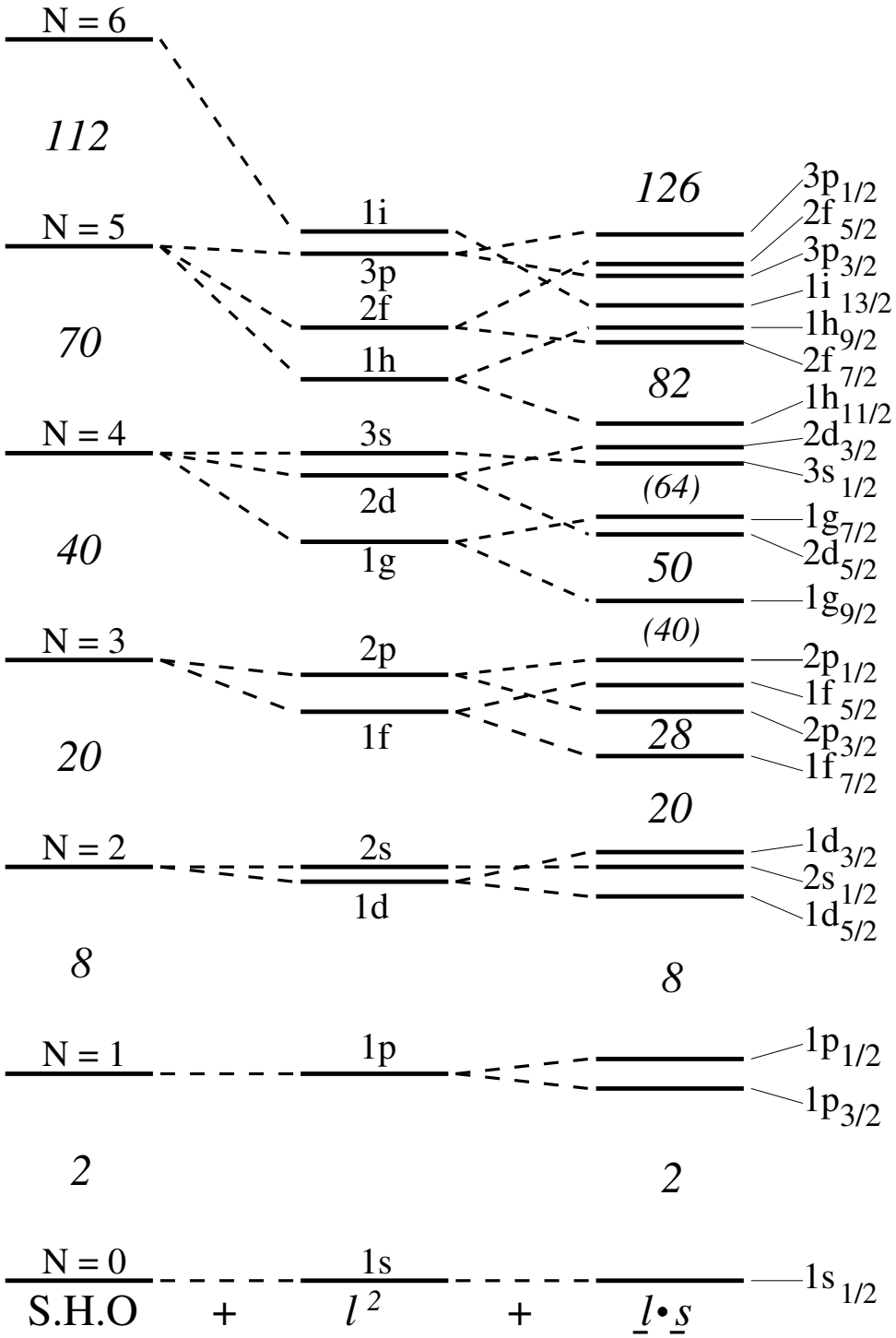

FIGURE 2.3: Single-particle energies for a simple harmonic oscillator (SHO), a modified harmonic oscillator with $\mathbf{l}^2$ term, and a realistic shell model potential with $\mathbf{l}^2$ and $\mathbf{l}\cdot\mathbf{s}$ terms. N labels the oscillator shell. Adapted from Ref. [22].

to new energy gaps, and the familiar, experimentally observed magic numbers. In addition to the numbers listed previously, in Fig. 2.3 two extra magic numbers are shown in parentheses, 40 and 64. In some cases, over limited ranges of N and Z, these are weakly magic [22]. The shell gap that opens above the $1g_{7/2}/1d_{5/2}$ $n\ell j$ orbitals at a proton or neutron number of 64 is particularly important for this work, since ^{155}Ho and ^{156}Er have $Z = 67$ and $Z = 68$ respectively. Terminating configurations, for example, are given relative to the 'doubly magic' $^{146}_{64}\mathrm{Gd}_{82}$ core. Furthermore, having only ten valence nucleons outside the 'doubly magic' spherical core, ^{156}Er is discussed as representing a 'transitional' nucleus where nuclear collectivity rapidly changes from vibrational to rotational motion [22].

2.2.3 The Anisotropic Harmonic Oscillator potential

Although the MHO potential successfully reproduced the observed shell gaps seen in nature, it does not take into account the effect of deformation. Away from shell gaps, the usual shape for a nucleus, including those studied in this thesis, is not spherical, but quadrupole deformed.

The short-range effects of nucleon pairing favour radial symmetry, but the long-range component of the nucleon-nucleon residual interaction, namely the quadrupole-quadrupole interaction, favours a deformed shape. At closed shells pairing dominates — it is in the mid-shell regions that the long-range interaction becomes more important. The resulting nuclear shape is a result of competition between these two effects. These long-range interactions are not considered in the potentials discussed so far.

The Anisotropic Harmonic Oscillator (AHO) potential models the mean field potential of an axially deformed (prolate or oblate) nucleus:

$$V_{osc} = \tfrac{1}{2}[\omega_{\perp}^2(x^2 + y^2) + \omega_z^2 z^2]. \tag{2.13}$$

A 'stretched' coordinate system [23] is used to parametrise the deformation,

$$\xi = x\sqrt{\frac{m\omega_x}{\hbar}}; \quad \eta = y\sqrt{\frac{m\omega_y}{\hbar}}; \quad \zeta = z\sqrt{\frac{m\omega_z}{\hbar}}; \tag{2.14}$$

where $\omega_x = \omega_y = \omega_\perp$. The ρ and θ_t terms are then defined as

$$\rho^2 = \xi^2 + \eta^2 + \zeta^2; \quad \cos\theta_t = \zeta/\rho. \tag{2.15}$$

The potential can now be expressed in terms of the deformation parameter, ε_2 [24],

$$V_{osc} = \tfrac{1}{2}\hbar\omega_0\rho^2\left[1 - \tfrac{2}{3}\varepsilon_2 P_2(\cos\theta_t)\right]. \tag{2.16}$$

The deformation parameter, ε_2, is almost the same as the β_2 quadrupole deformation parameter, which was introduced earlier. For small deformations the two terms are related by

$$\varepsilon_2 \approx \frac{3}{2}\left(\frac{5}{4\pi}\right)^{1/2}\beta_2 \approx 0.95\beta_2. \tag{2.17}$$

When discussing deformation in general terms, the two are often used interchangeably and both parameters will be referred to in this thesis. Only quadrupole deformation ($\lambda = 2$) has been considered up to this point, though terms corresponding to higher multipoles of deformation can be added to Eq. 2.17 and calculations presented here generally include small hexadecapole ($\lambda = 4$) deformation, given by $\varepsilon_4 = \frac{1}{6}\varepsilon_2^2$. The relation between the hexadecapole parameters are approximately

$$\varepsilon_4 \approx -\left(\frac{9}{4\pi}\right)^{1/2}\beta_4 \approx -0.85\beta_4, \tag{2.18}$$

and it should be noted that, while similar in magnitude, ε_4 is opposite in sign to β_4. The spin-orbit $\mathbf{l}\cdot\mathbf{s}$ term of the MHO potential is also added to the potential. It has already been shown how introducing the spin-orbit and $\mathbf{l}^2$ modifications to the

harmonic oscillator potential lifts the degeneracy of the N_{osc} shells into separate $n\ell j$ orbitals (for example the $N_{osc} = 3$ splits into four orbitals; $1f_{5/2}$, $1f_{7/2}$, $2p_{1/2}$, $2p_{3/2}$). Introducing deformation to the potential has the effect of lifting the degeneracy even further.

Another consequence of introducing deformation to the system is that the $n\ell j$ quantum numbers are no longer 'good' quantum numbers – they are not conserved as deformation is varied. The solutions to the AHO potential are therefore labelled by the Nilsson asymptotic quantum numbers as follows,

$$\Omega^{\pi}[N_{osc} n_z \Lambda], \tag{2.19}$$

where π is parity and Ω the single-particle projection of the total angular momentum on the symmetry axis. A related quantity to Ω is K, the projection of the total angular momentum on the symmetry axis. Provided the rotation axis is perpendicular to the symmetry axis, as is the case with a prolate rotating nucleus the two terms can be used interchangeably [22]. Inside the brackets the three quantum numbers are: N_{osc}, the oscillator quantum number denoting the major shell; n_z, the number of oscillator quanta along the symmetry axis; and Λ, the single-particle orbital angular momentum along the symmetry axis. As illustrated in Fig. 2.4, $\Omega = \Lambda + \Sigma$, with Σ being the single-particle spin angular momentum along the z-axis. It can be seen that a high-Ω orbital will have a very different orientation with respect to the nuclear symmetry system to a low-Ω orbital, and as such the two will have different energies. In general, low-Ω Nilsson orbitals prefer prolate deformation, and high-Ω orbitals prefer oblate deformation.

The potential in Eq. 2.13 is axially symmetric about the z-axis. However, it will be seen there is reason to believe that the nuclides of interest here sometimes adopt

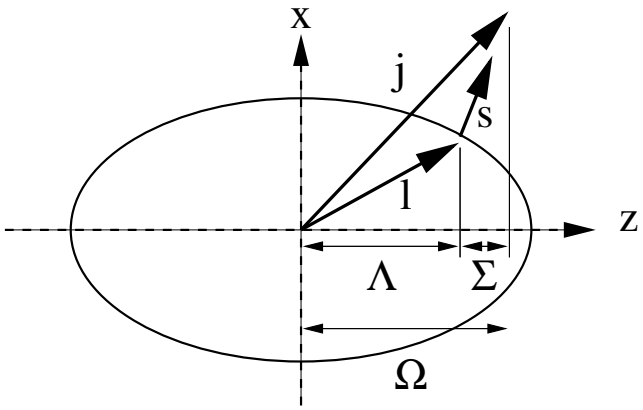

FIGURE 2.4: Nilsson orbital quantum numbers. The nucleus has positive quadrupole (prolate) deformation, z being the symmetry axis, and x the axis of rotation. Reprinted from Ref. [34].

an axially asymmetric shape. The AHO model can be generalised, and orbitals calculated as a function of γ as well as β_2, using the Lund convention of Fig. 2.1.

2.2.4 Cranked Shell Model

A further extension to the shell model can be made that introduces a further degree of freedom, rotational frequency, $\hbar\omega$. Cranking models take into the account the response of nucleons to the rotation of the nuclear potential [25]. The cranking Hamiltonian can be expressed as

$$H_\omega = H_0 - \omega \hat{I}_x. \tag{2.20}$$

H_0 is the static Hamiltonian in the laboratory system, for example the Anisotropic Harmonic Oscillator Hamiltonian of the previous section, and ωI_x is the quantum operator corresponding to the effects of the classical Coriolis and centrifugal forces.

The modifications made to the harmonic oscillator potential so far, first the inclusion of an $\mathbf{l^2}$ and spin-orbit term term, then allowing the potential to assume a radially asymmetric form, have seen successive degeneracies of the N_{osc} shells

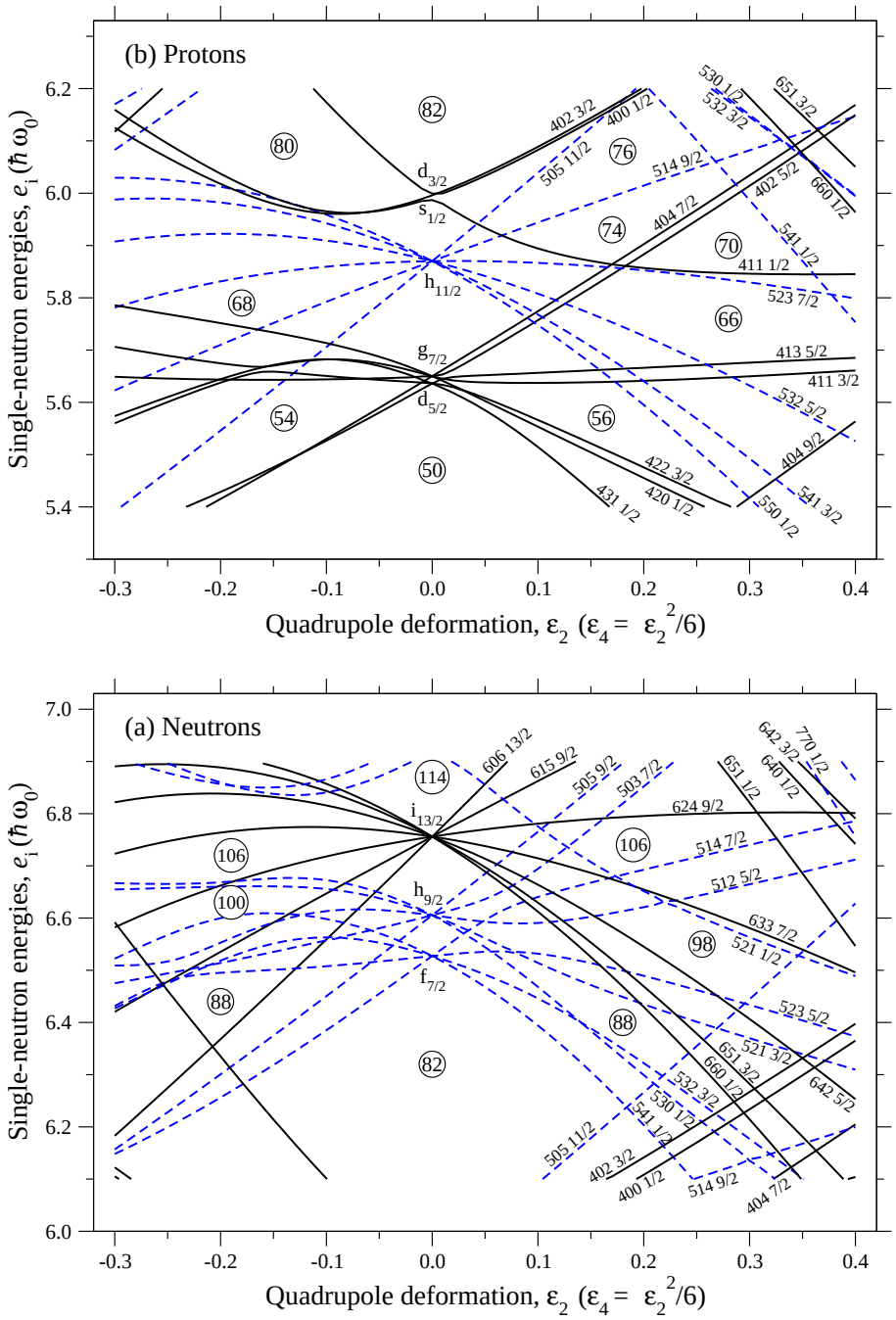

FIGURE 2.5: Nilsson diagram for (a) protons and (b) neutrons, using the AHO potential, calculated with the $A = 150$ parameters [21] for the region of interest for ^{155}Ho and ^{156}Er. Positive-parity levels are denoted by solid (black) lines and negative-parity levels by dashed (blue) lines, respectively. Reprinted from Ref. [3].

being lifted. The onset of rotation sees the final, two-fold, degeneracy of the Nilsson orbitals being broken.

The two-fold degeneracy of each Nilsson orbital when stationary corresponds to a pair of nucleons moving in symmetrical *time reversed* orbits. Once in a rotating frame, the effect of the ωI_x depends on whether the nucleon is moving with or against the collective rotation, and this symmetry is broken. The result is states of opposite signature, α. The ωI_x term depends on the spatial orientation of the nucleon's orbit with the core so the behaviour of a nucleon under rotation is dependent on which orbital it occupies. Unfavoured configurations at $\omega = 0$ can become competitive with increasing rotational frequency.

The calculated energies are called Routhians, and are labelled by their parity and signature, (π, α). Under rotation the $n\ell j$ quantum numbers and Nilsson labels are no longer 'good' quantum numbers, and a single (π, α) orbital will represent a mix of Nilsson configurations. However, if an orbital is composed principally of a particular Nilsson configuration, it often will be labelled as such.

2.2.5 Quasiparticles

Cranking calculations are presented in this thesis in the form of quasiparticle energies. Quasiparticles are mathematical constructions that describe excitations in terms of linear combinations of particle and hole occupation probabilities. Using the quasiparticle construct the particles can be replaced by non-interacting quasiparticles whose energies are additive. For each single-particle level there are two quasiparticle levels, one positive and one negative, reflections of each other about the Fermi surface. The Hartree-Fock-Bogoliubov (HFB) formalism can be applied to the cranking Hamiltonian to give quasiparticle excitations in the rotating frame [26].

Presented in Fig. 2.6 are the results of cranking calculations for ^{156}Er. The Routhians plotted are for quasineutron levels. The AB crossing has been marked

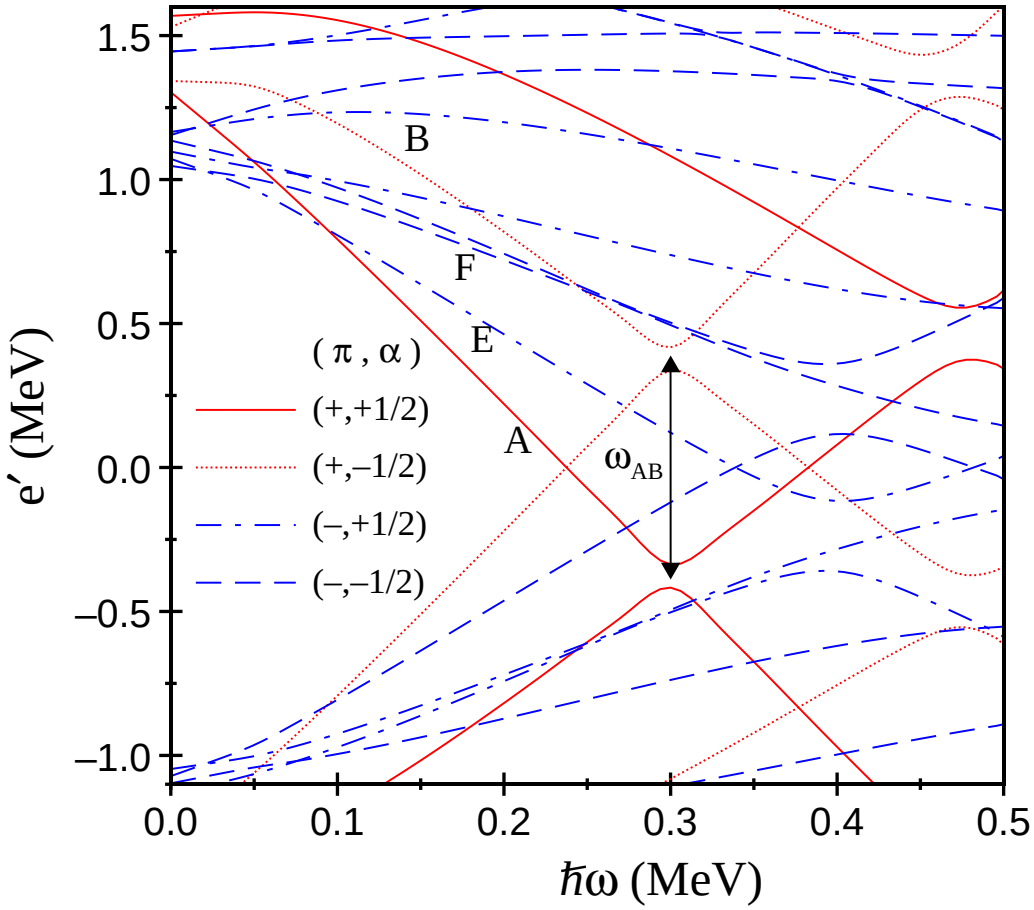

FIGURE 2.6: Quasineutron Routhians for ^{156}Er, the result of cranking calculations using a MHO potential [27, 28]. Deformation parameters $\beta_2 = 0.175$, $\beta_4 = -0.13$ [29] have been used. The AB neutron crossing at $\hbar\omega_{AB} \approx 0.3$ MeV is shown.

on the plot. The frequency ω_{AB} indicates the critical frequency at which the Coriolis force, acting in the opposite direction on a pair of neutrons in *time-reversed* orbits, causes the pair to break and align along the rotation axis [27, 28]. Consequently, a single particle contribution is added to the total angular momentum of the nucleus.

2.2.6 Potential energy surfaces and the Strutinsky method

Fig. 2.7 represents a plane in deformation space, using the Lund convention of Fig. 2.1. It is possible to calculate the potential energy of a nucleus, at a given spin, for a 'mesh' of points on the (ϵ_2, γ) plane and plot the result as a potential

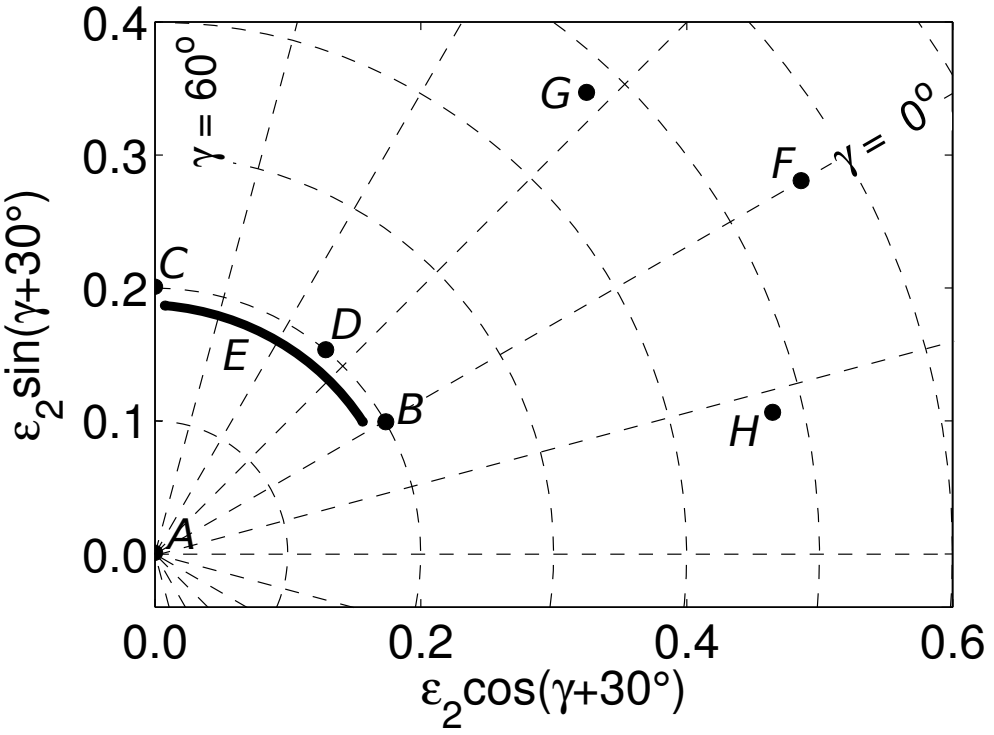

FIGURE 2.7: A-H represent minima of potential energy surfaces for different nuclear shapes. A is a spherical nucleus, B a normally deformed, prolate rotating nucleus, and C a non-collective oblate nucleus. D represents the potential energy minimum of a nucleus with rigid triaxial deformation, and E a γ-soft nucleus described by a Wilets-Jean type potential. F, G, and H are the minima for a superdeformed (SD) and two triaxial superdeformed (TSD) shapes.

energy surface (PES). The minima on such a surface represent favoured shapes that the nucleus is likely to adopt. Different minima and the shapes they represent are shown in Fig. 2.7. While these are just examples, actual calculated PES plots for ^{156}Er are presented in Chapter 4. Such PES calculations, described in Ref. [30] are used in Cranked Nilsson Strutinsky (CNS) calculations. Configurations are specified by the number of particles in different oscillator N-shells of signature $\alpha = \pm 1/2$ and the minima that are found on the (ϵ_2, γ) mesh reveal favoured configurations, and form the basis for further calculations [5]. Presented in Chapter 5 are the results of Cranked Nilsson Strutinsky (CNS) calculations for terminating configurations in ^{155}Ho.

2.3 Collective rotation

A nucleus must be deformed to exhibit rotational behaviour since in spherical nuclei rotational excitations are quantum mechanically forbidden. For this reason nuclei tend to be rotational away from closed shells. For bands with intrinsic angular momentum, $K = 0$, such as the ground-state band of even-even nuclei, the rotational energy has the simple form [26]

$$E(I) = \frac{\hbar^2}{2\mathcal{J}} I(I+1), \tag{2.21}$$

which is the expression obtained by quantizing the classical Hamiltonian for a symmetric rotating system. $\mathcal{J}$ is the effective moment of inertia. For good rotors, deviations from (2.21) may be viewed as a dependence of the moment of inertia on the rotational angular momentum. The ratios between the energies of excited states that this relationship gives rise to can be good indicator of the rotational nature of a nucleus.

$$\frac{E(4^+)}{E(2^+)} = 3.33, \qquad \frac{E(6^+)}{E(2^+)} = 7.00. \tag{2.22}$$

2.3.1 Analysing rotational behaviour

Almost all the excited levels discussed in this thesis belong to rotational bands. Indeed, it is often the deviations from the rotational behaviour characterized by Eq. 2.21 which are instructive in deducing the underlying shell configuration of band structures. Experimentally, for $\Delta I = 2$ transitions, the rotational frequency is

$$\hbar\omega = \frac{dE(I)}{dI_x} \approx \frac{E_\gamma}{2}, \tag{2.23}$$

i.e. half the γ-ray energy. Experimental alignments, I_x can be used to investigate the rotational properties of a nucleus. At a given spin I, the aligned spin is $I_{\mathrm{x}} = \sqrt{I(I+1) - K^2}$. The additivity of the contributions of energy and aligned spin contributions from individual orbitals is useful when analysing the data. At a given frequency, the difference in alignment between rotational bands will be due to the difference in the underlying particle configurations of the bands. To aid measuring increases in alignment and the differences in alignment between bands, a rotating reference based on Eq. 2.21 is subtracted from the aligned spin to give the experimental alignment, i_{x}:

$$i_{\mathrm{x}}(\omega) = I_{\mathrm{x}}(\omega) - \omega(\mathcal{J}_0 + \mathcal{J}_1\omega^2), \tag{2.24}$$

where $\mathcal{J}_0$ and $\mathcal{J}_1$ are Harris parameters that characterize the rotational reference, and are chosen to give approximately zero experimental alignment for the ground-state band at low rotational frequency [31].

When discussing the quasineutron Routhian calculations of Fig. 2.6 it was noted that an AB neutron crossing should occur at a frequency of $\hbar\omega \approx 0.3$ MeV. Experimentally this is seen as an increase in aligned angular momentum, I_x, called a backbend.

A similar technique to plotting aligned angular momentum as a function of frequency is the use of rigid rotor plots. They can be useful to see which structures are yrast at a given spin, and are particularly useful when investigating favoured oblate band terminating states, which are discussed in more detail in Chapters 4 and 5. Energy is plotted as a function of spin relative to a rigid-rotor, or rotating liquid drop. Here, two different forms of the reference have been used. The first is given by

$$E_{ref} = C \cdot I(I+1), \tag{2.25}$$

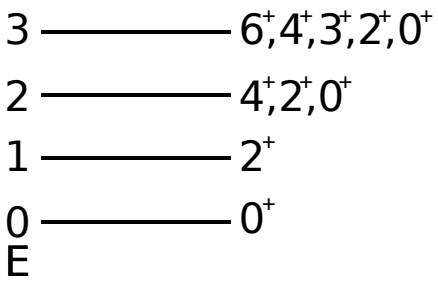

FIGURE 2.8: Low-lying levels of a spherical harmonic vibrator nucleus.

where the constant C scales with mass as $A^{-5/3}$ and is generally given the value 0.007 MeV for $A = 158$ [5, 32]. The second form is the rotating liquid drop reference of Ref. [33] and is given by

$$E_{rld}(Z, n, I, \varepsilon_i) = E_{ld}(Z, n, \varepsilon_i) + \frac{\hbar^2 I(I+1)}{2\mathcal{J}_{\text{rig.}}(Z, n, \varepsilon_i)}, \tag{2.26}$$

where E_{ld} is the static liquid drop energy, ε_i indicates the deformation parameters, and $\mathcal{J}_{\text{rig.}}$ is the rigid-body moment of inertia. This reference is preferable when comparing high-spin states of different nucleus, since it takes into account the mass excess of the nucleus and is not dependent on the shell energy of the ground state.

2.4 Vibrational modes of excitation

Another mode of collective excitation is vibration. A simple vibrational mode to consider is quadrupole vibration of spherical even-even nuclei, due to harmonic oscillations of the nuclear surface. The resulting low-lying energy levels, shown in Fig. 2.8 are evenly spaced, and characterised by phonon multiplets $(0^+), (2^+), (0^+, 2^+, 4^+)$, $(0^+, 2^+, 3^+, 4^+, 6^+)$ [22]. Each state is classified by quantum numbers n_β, representing oscillations in β, and a phonon-like quantum number, Λ. The energies of the states are determined by $E(n_\beta, \Lambda) = E_0 + (2n_\beta + \Lambda)\hbar\omega$, which results in the given degeneracies [34].

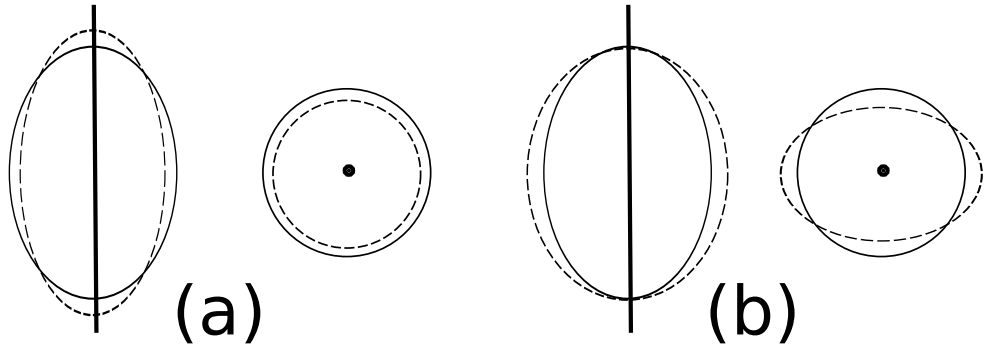

FIGURE 2.9: (a) β vibrations and (b) γ vibrations of prolate deformed nuclei. The solid lines depict the nuclear shape 'at rest' in directions perpendicular and parallel to the symmetry axis. The dashed lines show the oscillations in shape due to the vibrational modes. For (b) a γ-vibration, axial symmetry is lost. Adapted from Ref. [26].

It has been noted that a prolate rotational nucleus will have a $E(4_1^+)/E(2_1^+)$ ratio of 3.33. Similarly, the equal spacing of the vibrational levels means that for spherical vibrating nuclei the relation $E(4_1^+)/E(2_1^+) = 2$ is expected.

2.4.1 β and γ vibrations

Two modes of vibrational excitations that are available to a nucleus with quadrupole deformation, β-vibrations and γ-vibrations, will now be considered. When discussing the concept of deformation, β and γ were introduced as deformation parameters. Their definitions relate directly to the oscillations in nuclear shape that β- and γ-vibrations represent. Vibrational excitations which preserve the axial symmetry of the nucleus are known as β-vibrations, so called because they correspond to an oscillation in the β-deformation of the nucleus. Similarly, a γ-vibration corresponds to a change in γ-deformation, causing a prolate nucleus to temporarily lose its axial symmetry. The breaking of the axial symmetry of the nucleus is the reason why γ vibrations are always associated with a projection of angular momentum along the symmetry axis of $K = 2$. A comparison of β and γ vibrational modes is shown Fig. 2.9.

2.4.2 Rotation Vibration Model

The Rotation Vibration Model (RVM) considers a well deformed, axially symmetric even-even nucleus, allowing small dynamic fluctuations about the equilibrium shape. The energies of the resulting levels are given as

$$E = \epsilon_R[I(I+1) - K^2] + \epsilon_\beta n_\beta + \epsilon_\gamma n_\gamma, \tag{2.27}$$

where $\epsilon_R = \hbar^2/2\mathcal{J}$ (see Eq. 2.21). The quantum numbers are constrained such that:

$$\begin{aligned} K &= 0, 2, 4... \\ I &= 0, 2, 4, ... \text{ for } K = 0 \\ &= K, K+1, K+2, ... \text{ for } K \neq 0 \\ n_\beta &= 0, 1, 2, ... \\ n_\gamma &= K/2, K/2+2, K/2+4, ... \end{aligned} \tag{2.28}$$

The ground-state band is reproduced for $K = n_\beta = n_\gamma = 0$,

$$E = \epsilon_R I(I+1), \tag{2.29}$$

with the familiar $I = 0, 2, 4, ...$ rotational levels. For $n_\beta = 1$ and $K = 0$, a rotational band built on a β-vibration is produced with energy levels

$$E = \epsilon_\beta + \epsilon_R I(I+1), \tag{2.30}$$

again with $I = 0, 2, 4, ...$ levels. Rotational bands built on the second 0^+ state are often interpreted as β bands. A γ vibration requires that $K = 2$ and $n_\gamma = 1$, which forms the set of levels

$$E = \epsilon_\gamma + \epsilon_R[I(I+1) - 4], \tag{2.31}$$

this time with even- and odd spin-members, $I = 2, 3, 4, ...$, forming the γ band.

The relative energies of the even- and odd-spin members of the γ-vibrational band (signature splitting) give an insight into the nature of the triaxiality of the nucleus. Two theoretical approaches are considered here, the γ-rigid Asymmetric Rotor Model [35], and the γ-soft, Wilets-Jean model [36].

2.4.3 Triaxiality and γ bands

The Asymmetric Rotor Model (ARM) investigates rigid, or static triaxial nuclear shapes ($\gamma \neq 0°$) [35]. In this model, the relative level energies of the ground-state and the γ-vibrational band are sensitive to the degree of triaxiality of the nucleus. In particular, it makes predictions for the following relations between energy levels in the ground-state band ($E_{g.s.}$) and the γ-vibrational band (E_γ):

$$\begin{aligned} E_\gamma(3^+) &= E_{g.s.}(2^+) + E_\gamma(2^+) \\ E_\gamma(5^+) &= 4E_{g.s.}(2^+) + E_\gamma(2^+). \end{aligned} \tag{2.32}$$

Whereas the predictions of the Asymmetric Rotor Model are for shapes with definite, rigid triaxial deformation, another approach considers a γ-soft shape [36]. The Wilets-Jean potential has a finite β deformation, but is completely flat with respect to γ and describes a dynamic triaxial deformation. Such a γ-soft nucleus would oscillate uniformly between $\gamma = 0°$ (prolate) and $\gamma = 60°$ (oblate). The form a rigid triaxial and γ-soft potential would take are illustrated in Fig. 2.7. Many of the predictions of the two potentials yield similar results, provided their effective average asymmetry is the same [22]. However, the relative energies of the even- and odd-spin members of the γ-vibrational band can provide a distinct signature capable of distinguishing between γ-soft and rigidly triaxial shapes. In the rigid triaxial case, γ-band levels appear in doublets as $(2^+_\gamma - 3^+_\gamma)$, $(4^+_\gamma - 5^+_\gamma)$, $(6^+_\gamma - 7^+_\gamma)\ldots$,

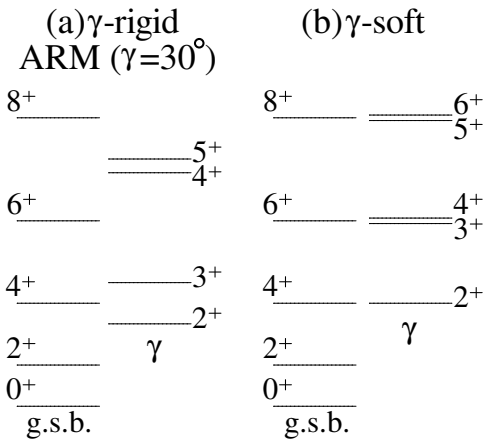

FIGURE 2.10: Predicted γ-band energy levels using (a) the γ-rigid ARM model of Davydov [35] and (b) a Wilets-Jean γ-soft potential [36].

but the γ-soft case results in a 2^+_γ, $(3^+_\gamma - 4^+_\gamma)$, $(5^+_\gamma - 6^+_\gamma)\ldots$ pattern [37, 38]. The predicted level structures are shown schematically [39] in Fig. 2.10 for the Davydov and Wilets-Jean models. Since for the completely flat γ-soft model the average γ deformation is $\bar{\gamma} = 30°$, a value of $\gamma = 30°$ has been used for the Davydov potential.

2.5 Selection Rules and Transition Strengths

The conservation of angular momentum imposes the following selection rule on the multipolarities of γ-ray transitions between two states, $I_i \rightarrow I_f$, such that,

$$|I_i - I_f| \leq L \leq |I_i + I_f|, \quad (L \neq 0) \tag{2.33}$$

where L denotes the transition multipolarity. The electromagnetic interaction is parity conserving, which imposes the additional selection rule,

$$\pi_i \pi_f = \pi_L \tag{2.34}$$

where π_i and π_f are the parities of the initial and final states. Whether a transition is electric (E) or magnetic (M) in nature depends its multipolarity and the change in parity it represents,

$$\pi(EL) = (-1)^L, \quad \pi(ML) = (-1)^{(L+1)}. \tag{2.35}$$

Considering only the lowest multipolarities, where the initial and final states have the same parity, the transition will be $M1$ or $E2$ in nature, and where there is a change in parity the transition will be an $E1$ or $M2$. Because transition probabilities decrease rapidly with increasing multipolarity, and electric transitions are faster than magnetic transitions of the same order, it is assumed that all the transitions observed in this work are $E1$, $M1$, or $E2$ in nature. When there are several allowed multipolarities a transition can have 'mixed' nature, which means mixed $M1/E2$ transitions will also be considered.

2.5.1 Reduced Transition Probabilities

The reduced probability of a stretched $E2$ transition can be defined as [40],

$$B(E2; I \to I-2) = \frac{5}{16\pi} e^2 Q_0^2 |\langle I_i K_i 20 | I_f K_f \rangle|^2 \quad (eb^2), \tag{2.36}$$

where Q_0 is the quadrupole moment, which is related to the deformation. The term in brackets is a Clebsch-Gordon coefficient. The reduced transition probability of a stretched $M1$ transition is defined as [40],

$$B(M1; I \to I-1) = \frac{3}{4\pi} (g_K - g_R)^2 K^2 |\langle I_i K_i 10 | I_f K_f \rangle|^2 \quad (\mu_N^2), \tag{2.37}$$

where g_R is the collective g-factor and g_K the single-particle g-factor, which depends on the intrinsic shell configuration of the state. Again, the term in brackets is a

Clebsch-Gordon coupling coefficient, and $B(M1)$ values are given in units of the nuclear magneton, μ_N. The two equations, 2.36 and 2.37, form the basis for the geometric model calculations of Dönau and Frauendorf [14], which are compared to measured $B(M1)/B(E2)$ ratios in Chapter 5.

Chapter 3

Methods

All of the data used in this work are detections of γ rays emitted by excited nuclei following heavy-ion fusion-evaporation reactions. Data from two experiments have been analysed here, both performed at the ATLAS facility of Argonne National Laboratory, using the Gammasphere γ-ray spectrometer. Presented in Table 3.1 are the details for both experiments. In this type of analysis the presence of excited stated is inferred from the γ rays emitted when the nucleus decays from one state to another. This chapter outlines the techniques used to extract nuclear structure information from the experimental data.

3.1 The reaction

Fusion evaporation reactions were used to populated states of high angular momentum in the nuclides of interest. The time scale of compound-nucleus reactions (like fusion-evaporation reactions) is around 10^{-18}s. This is shorter than the time scale of γ-ray transitions, which ranges from approximately 10^{-15}s to 10^{-9}s [41]. For this reason, γ-ray spectroscopy is mostly concerned with the excited nuclei produced

TABLE 3.1: Comparison of the two experiments.

	^{156}Er	^{155}Ho
Experiment name	GSFMA229	GSFMA269
Projectile nucleus	^{48}Ca	^{37}Cl
Beam energy	215 MeV	180 MeV
Target nucleus	^{114}Cd	^{124}Sn
Thickness	1.0 mg/cm^2	1.1 mg/cm^2
Target type	Au backed, 13 mg/cm^2	Self supporting
Reaction channel	6n	6n
Duration	$\sim$ 12 days	$\sim$ 6 days
Events collected	$\sim 4.8 \times 10^{10}$	$\sim 1.6 \times 10^{10}$
γ-ray trigger	4	5

after the nuclear reaction processes induced by the strong interaction have taken place.

In a fusion evaporation reaction, the projectile nucleus is accelerated to sufficient energies to form a highly excited compound nucleus with the target. Because the line of stability falls below the $N - Z$ line, the composite nucleus formed during a fusion evaporation reaction is normally located on the neutron-deficient side of the $N - Z$ plane. The compound nucleus subsequently loses excitation energy through the evaporation of neutrons and, to a lesser extent, protons and α particles. The particle evaporation tends to carry away much excitation energy but relatively little angular momentum. In most cases the residual nucleus is left in an excited state, which is below the threshold for further particle evaporation [42]. The residual nucleus first de-excites by emitting statistical γ-rays until states near the yrast line are reached. Decay to the ground state then occurs along, or near to, the yrast line via generally spin-stretched transitions between discrete states. It is these transitions

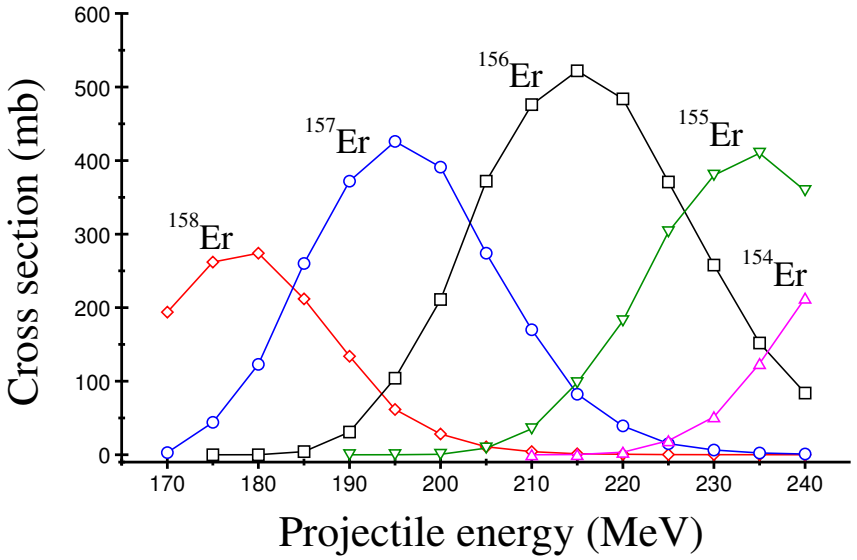

FIGURE 3.1: PACE cross-section calculations for the reaction used in the ^{156}Er experiment, showing the results for the 4n–8n (^{158}Er–^{154}Er) neutron-evaporation reaction channels.

which have been observed in this work and have been used to deduce the structure of ^{156}Er and ^{155}Ho, and the changes in their behaviour with increasing spin and excitation energy.

The yrast line, or competing yrast bands, in the low excitation region accumulate most of the γ-ray flow. This means that the branching ratio for the yrast transitions at low spin approaches 100%, and they can be used to evaluate the total yield of the residual nucleus.

The reaction channels are usually expressed in the form A(a,xn yp zα...,γ)B*, where A is the target, a is the projectile and x, y and z are the number of evaporated protons, neutrons and α particles evaporated to produce B*, the excited residual nucleus. Both nuclides studied here were populated via the 6n evaporation channel.

In high-spin studies the aim is usually to produce residual nuclei of interest with as much excitation energy and angular momentum as possible, that are sufficiently populated to be within experimental observable limits. Statistical model calculations of the fusion evaporation reactions [43] were performed before the experiments, and

the results were used when deciding what the beam energies should be. Presented in Fig. 3.1 are examples of cross-section calculations of this type, performed using the program PACE, which is incorporated in the LISE package [44]. The calculations have been performed for the ^{114}Cd(^{48}Ca,xn)$^{162-x}$Er reaction for a range of bombarding energies.

A beam energy of 215 MeV was used in the ^{156}Er experiment. To a varying extent, the projectile nuclei are slowed slightly by the target, resulting in a 200–215 MeV range of energies at impact with the target nuclei. At these energies ^{156}Er (via the 6n evaporation channel) is predicted to be have the greatest cross section. The primary aim of the experiment was to study ^{157}Er and ^{158}Er, and a lower beam energy would have produced a greater yield of both. However, the higher beam energy results in states of greater spin and excitation energy being populated, including the superdeformed (SD), and triaxial superdeformed (TSD) bands of interest. The result of this is that many states in the normally-deformed level scheme of ^{156}Er nuclei were populated, and new structures have been observed. Similarly, excited states in ^{155}Ho were also produced via the 6n reaction channel and, while they were not populated to as high spins as the 4n and 5n reaction channels (^{156}Ho and ^{157}Ho), enough data were collected for ^{155}Ho that many new transitions have been observed.

3.2 The Gammasphere

A large spherical array of up to 110 Compton suppressed high-purity germanium (HPGe) detectors [45, 46], the Gammasphere detects the γ rays emitted during the decay process. The most important properties of the detectors are: high detection efficiency, good ($<$ 1 keV) energy resolution, high ratio of full-energy to partial-energy events and high granularity. In the MeV range, the best combination of these

FIGURE 3.2: Schematic of a HPGe detector in the Gammasphere array. The principle of Compton suppression is also illustrated: The upper and lower gamma rays are scattered out of the HPGe crystal, but are detected by the BGO suppression shields, meaning their energies can be vetoed. Reprinted from Ref. [47].

properties is given by HPGe semiconductor detectors. The Compton suppression shields are auxiliary detectors used to achieve a better peak-to-total ratio [2]. They consist of Bismuth Germanate (BGO) crystals, chosen for their high efficiency, which detect γ rays scattered from the HPGe detectors. It is desirable to veto detections corresponding to scattered γ rays, since only a fraction of their total energy is registered by the HPGe detector and will thus contribute to the background counts. The HPGe detectors are categorised by their angle θ with respect to the beam axis, and in this way grouped into 17 'rings', which are listed in Table 3.2. Before these experiments, the detectors at 17.3° (ring 1) had been removed to allow access to the

down-beam Fragment Mass Analyzer, which is often used in conjunction with the Gammasphere in other experiments. In total, the 101 HPGe detectors used in these experiments have a solid angle coverage of 42% of 4π [2]. Fig. 3.2 shows a cross section through part of the Gammasphere array.

3.3 Coincidence data analysis

The short timescale of the de-excitation of the residual nuclei following a fusion evaporation reaction means that as far as the detector system is concerned, the decay to stable states is instantaneous. The chain of γ rays emitted as part of a decay will be seen, to adopt the usual nomenclature, in *prompt time coincidence*. An obvious exception to this rule is when a state is particularly long lived. The time window within which detected γ rays are considered to be coincident and recorded as belonging to the same event is $\sim$70 ns. If an isomeric state has a lifetime much longer than this, the γ-rays below it will not be seen in coincidence with those above.

3.3.1 Matrices, cubes, and hypercubes

To facilitate analysis, coincidence data are sorted in formats that make it possible to easily and quickly gate on a transition and see which other γ rays are emitted at the same time and, by implication, as part of the same decay chain. The simplest example of this is a two dimensional histogram, or matrix. The full projection of the matrix shows all the γ rays detected as a function of energy, and setting a gate (i.e. viewing a slice) of the matrix at a particular energy reveals the γ-rays that were detected in coincidence with that energy. For sets of many, high-fold coincidence data, such as the two studied here, this practice is extended to three and four dimensions to produce *cubes* and *hypercubes*, respectively. A hypercube

was built for each data set making it possible to produce spectra of γ rays seen in simultaneous coincidence with three specified energies.

The favoured method of producing and analysing these multidimensional coincidence matrices is to use the RADWARE graphical analysis package [48, 49]. Before filling the coincidence matrices or cubes, the raw Gammasphere data were 'pre-sorted' into Eurogam format [50], at which stage certain γ-ray detections are removed, such as those outside of a given time window after the beam pulse. The RADWARE programs used to produce gated spectra are 'Levit8r' for cubes, and '4dg8r' for hypercubes. The programs also provide the tools to build the level scheme and, for a given gating condition, produce a calculated spectrum based on the current coincidence relations between transitions in the level scheme, and their relative intensities. In this way, obvious discrepancies between the observed coincidences and the proposed level scheme can be quickly recognized.

A calculated background spectrum is subtracted from every gated spectrum, using the methods of Ref. [51] and the resulting gated, background-subtracted spectra are extremely clean. No techniques are used to isolate specific nuclei other than γ-ray coincidences so being able to set an extra γ-ray gate can often help distinguish between contaminant γ rays and transitions that do belong to the nuclide of interest.

Fig. 3.3 illustrates how the coincidence analysis can show where a transition should be placed in a level scheme. Intensity arguments are also used to order γ rays in a level scheme, particularly in the case of bands of γ rays with few links to other structures. It is usually assumed that due to side feeding, the total intensity of the transitions exiting a state is greater than the total intensity of the feeding transitions. Examples of triple-gated quadruple-coincidence spectra used during the analysis of ^{155}Ho are presented in Fig. 3.4. The spectra show the energies of transitions in 'band 1', a previously unobserved, weakly populated structure. The reduced level

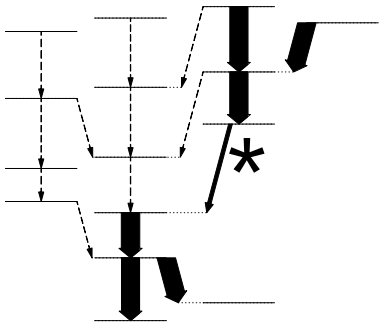

FIGURE 3.3: Example level scheme. The transition marked with the asterisk should be coincident with the thick-arrow transitions, and not the dashed-arrow transitions.

scheme of Fig. 3.4(e), which includes band 1 and some feeding transitions from other bands, is included to illustrate how these gated spectra, and others like them, have been used to build the level schemes for the nuclei of interest.

3.3.2 Multiple-fold sorting

An alternative method used to examine the data was to perform multiple-fold sorts using the MTSort sorting language [52]. This has the benefit of producing spectra quadruple-gated and above, while the hypercube is limited to triple-gated spectra. The data to be sorted are essentially a list of events, with each event consisting of a list of observed γ-ray energies that were detected within a 70 ns time window. Each energy is also labelled by detector number. The sorting procedure takes as its input a list of energy gates and if an event contains at least one energy that lies inside a gate, then the sort program increments the energies of that event into the single-gated (γ^1) spectrum. Likewise, if two energies pass the gating condition, the energies in the event are added to the double-gated (γ^2) spectrum. The process continues for higher numbers of coincidences [53]. With many high-fold data (which is the case here) γ^6 spectra or higher can be produced for gatelists corresponding to well populated structures. All detected energies are added to the γ^0, non-gated spectrum. Examples of the spectra produced by a multiple-fold sort are shown in

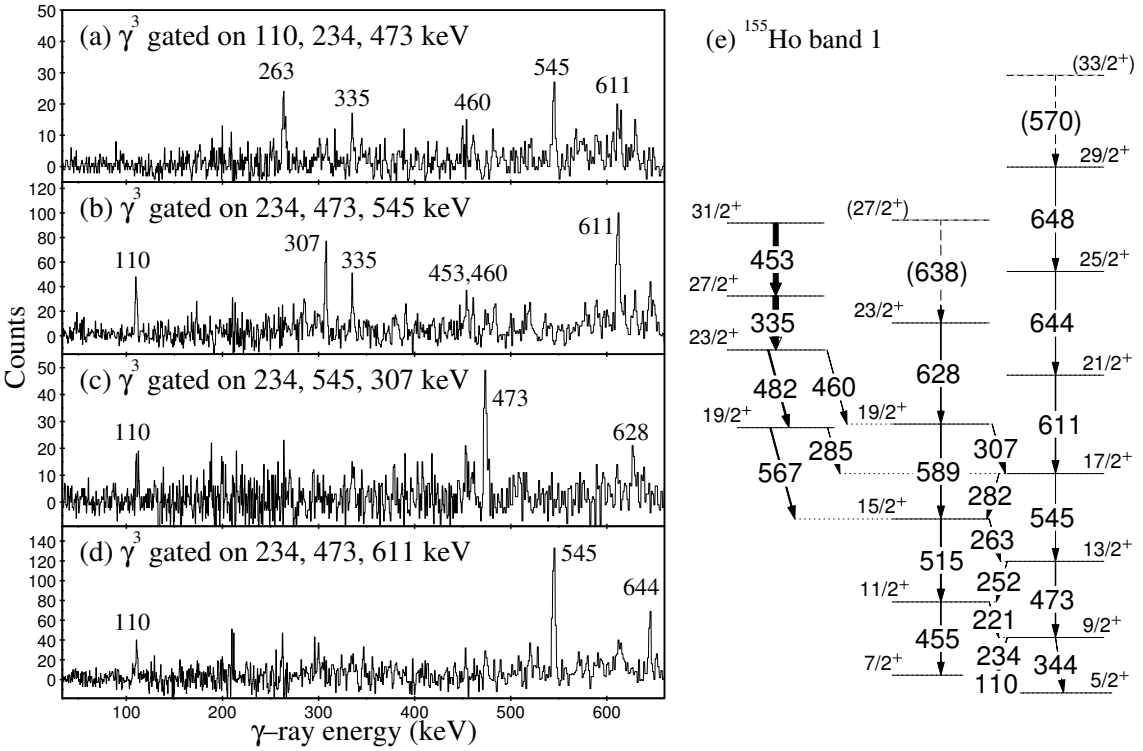

FIGURE 3.4: Triple-gated quadruple-coincidence spectra for ^{155}Ho band 1, and the reduced level scheme (e) for comparison.

Fig. 3.5. A gatelist containing all the ^{156}Er yrast-band energies was used in the sort and the resulting spectra proved useful in confirming previously observed transitions at high spin [3]. These transitions, which are very weak, are marked on the γ^4-gated spectrum. It will be shown that this way of sorting the data also proves useful when performing angular-correlation analyses.

The spectra of Fig, 3.5 have not had a background subtracted from them. When a background subtraction is required for a γ^n-gated spectrum, the γ^{n-1} lower-fold spectrum is often used, having been multiplied by a normalisation factor. The value of the normalisation factor is chosen in order to achieve, on average, zero counts between peaks in the background-subtracted spectrum. This method of background subtraction is usually effective because the γ^n-gated spectrum has a similar shape to the γ^{n-1}-gated spectrum. The peaks that are stronger in the the γ^n-gated spectrum

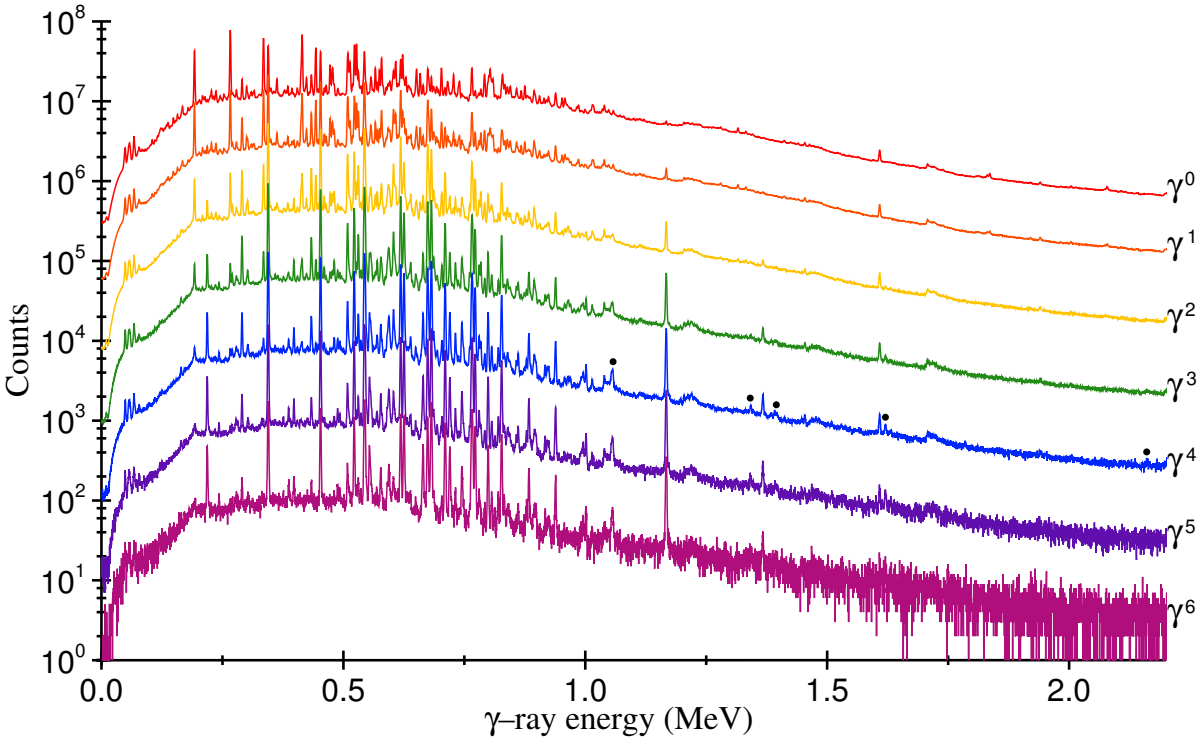

FIGURE 3.5: Multiple-fold gated spectra for the ground-state band of ^{156}Er. The black dots above the γ^4 spectrum denote the five high-energy transitions that feed the 42^+ terminating state; 1057 keV, 1342 keV, 1392 keV, 1621 keV and 2161 keV, reported in Ref. [3] and confirmed here.

correspond to energies that are truly coincident with the gatelist energies, and are accentuated following the subtraction.

3.3.3 Detector efficiency

When calculating the relative intensities of observed γ rays, it is necessary to take into account how the efficiency of the array varies with γ-ray energy. For each experiment, an efficiency calibration of the array was performed using well known γ-ray decays of radioactive sources. In order to measure the efficiency over over a broad range of energies, the sources ^{56}Co, ^{182}Ta, ^{243}Am and ^{152}Eu were used. Fig. 3.6 shows a fitted efficiency curve, $\varepsilon(E_\gamma)$, for the ^{155}Ho experiment, using the empirical

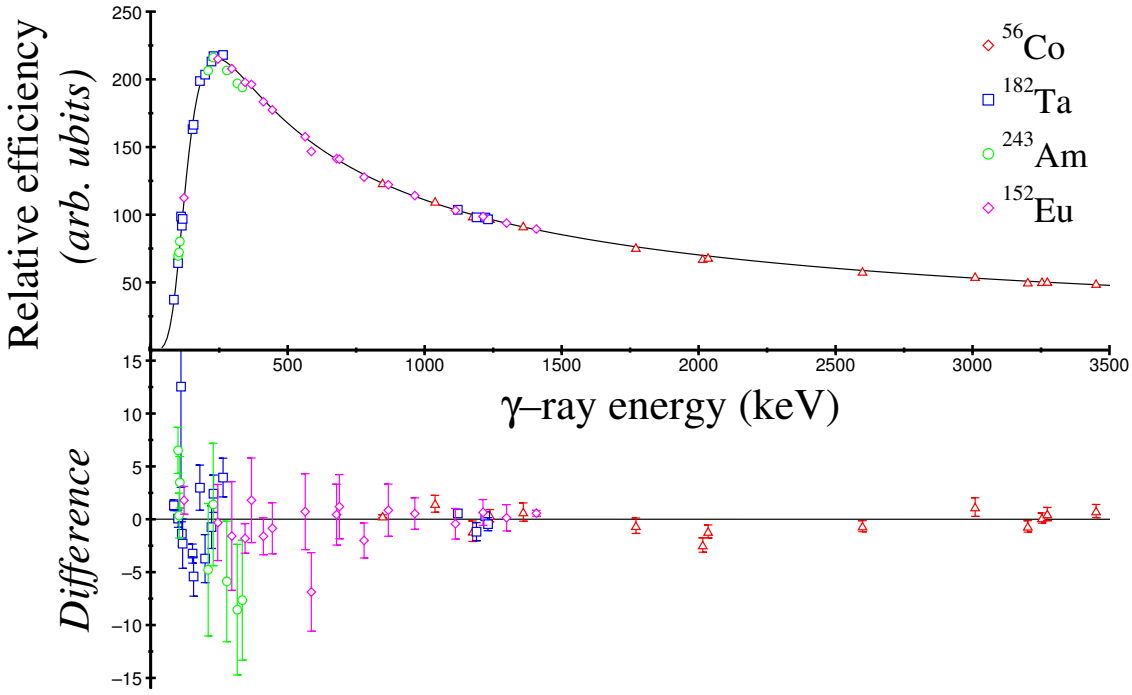

FIGURE 3.6: Fitted efficiency curve for the ^{155}Ho experiment. The lower graph shows the efficiency measurements plotted relative to the fitted curve, i.e. the difference between the two, with errors.

relationship

$$\varepsilon(E_\gamma) = \exp\left\{\left[(A + Bx + Cx^2)^{-G} + (D + Ey + Fy^2)^{-G}\right]^{-1/G}\right\}, \qquad (3.1)$$

where $x = \ln(E_\gamma/100)$ and $y = \ln(E_\gamma/1000)$ with E_γ in keV and the parameters A-G are fitted to the source data [54].

3.4 Targets and Doppler correction

The targets used in the two experiments were not of the same type. In the ^{156}Er experiment a 1.0 mg/cm^2 cadmium foil was backed with a thick (13 mg/cm^2) gold foil. The primary aim of the experiment was to measure quadrupole moments of strongly deformed bands in ^{157,158}Er [55], using the Doppler shift attenuation method [56]. This requires the highly excited residual nuclei to be slowed down

by the target during the short decay times of the highly collective superdeformed states ($\sim 10^{-14}$s) [57]. This means that nuclei are stopped completely by the time γ rays from the decay of the normally deformed level scheme are emitted. These data therefore have the benefit of improved energy resolution resulting from the elimination of the Doppler-broadening component of the photopeak width.

The ^{155}Ho experiment, by contrast, was performed using only self supporting tin foils, of total thickness 1.1 mg/cm^2. The nuclei were not stopped by the target and, during γ-ray emission, were travelling at an appreciable fraction ($\sim 2\%$) of c. The energies detected in the forward direction were therefore Doppler shifted higher in energy and those at the backward direction Doppler shifted to lower energies. The Doppler shifted energy is given by

$$E'_\gamma = E_\gamma(1 + \beta \cos\theta). \tag{3.2}$$

where β is the velocity of the recoiling nuclei v/c, θ the angle with respect to the beam direction, and E_γ the energy of the non-shifted γ-ray. It was therefore required that the detected energies be corrected. Energy spectra were sorted for the individual rings of the Gammasphere array, given in Table 3.2, and from the observed shifts in energy at known angles θ, the speed β of the recoiling nuclei was determined, and using this value a correction applied to the detected γ-ray energies. The average speed of the recoiling nuclei in the ^{155}Ho experiment was measured to be $\beta = 0.0206$.

3.5 Angular-correlation analysis

In order to meaningfully interpret the deduced states of the extended level schemes in terms of collective excitations and specific shell model configurations, it is imperative that their spins and parities are known.

TABLE 3.2: Detector angle θ for the rings of the Gammasphere, 1-17, used in Doppler corrections, and θ_{eff} for the summed rings, 1-9, used in the angular-correlation analysis. The percentage of the total efficiency each summed ring accounts for is also shown.

Ring number (original)	θ (°)	Ring number (summed)	θ_{eff} (°)	% of total detected γ rays
1	17.3	1	17.3	0.0
2	31.7	2	34.5	8.0
3	37.4			
4	50.1	3	54.2	14.8
5	58.3			
6	69.8	4	69.8	9.4
7	79.2	5	90	25.1
8	80.7			
9	90.0			
10	99.3			
11	100.8			
12	110.2	6	110.2	9.2
13	121.7	7	125.8	15.9
14	129.9			
15	142.6	8	145.5	11.6
16	148.3			
17	162.7	9	162.7	5.9

The way this is achieved in this work is through an angular-correlation analysis. Following the fusion-evaporation reaction, the residual nuclei that are produced are highly excited and rapidly rotating. Furthermore, the angular momentum of the nuclei is aligned perpendicular to the beam, which means that any preference in direction of emission exhibited by a γ ray can be readily identified. Usefully, this preference is sensitive to the I^{π} values of the initial and final states of the transition. The angular dependence of the intensity of a γ-ray transition can be expressed in terms of the angular distribution function,

$$W(\theta) = 1 + A_2 P_2(\cos\theta) + A_4 P_4(\cos\theta) \tag{3.3}$$

where $P_K(\cos\theta)$ are Legendre polynomials, and θ is the angle with respect to the beam axis. The angular distribution coefficients, A_K^{max}, can be calculated from theory, as described in Ref. [58]. A_K^{max} corresponds to the A_K for a nucleus that is maximally aligned perpendicular to the beam. In reality though, alignment is incomplete and states are assumed to form a Gaussian distribution about the perfectly aligned state. The attenuation parameter, α_K, is introduced to take this into account so that

$$A_K = \alpha_K A_K^{max}, \quad \alpha_2 \sim 0.8, \quad \alpha_4 \sim 0.5. \tag{3.4}$$

The α_K parameters may be determined experimentally, estimated empirically, or evaluated on the basis of a specific model [58].

For a transition between states I_i and I_f with competing multipolarities λ and λ' of multipole mixing ratio δ, the coefficient is given in terms of B_K and F_K functions, values of which are tabulated in the literature [58, 59]. The relation can be expressed in full as

$$A_K^{max} = \frac{B_K(I_i)}{1+\delta^2}\left[F_K(I_i\lambda\lambda I_i) + 2\delta F_K(I_i\lambda\lambda' I_i) + \delta^2 F_K(I_i\lambda'\lambda' I_i)\right]. \tag{3.5}$$

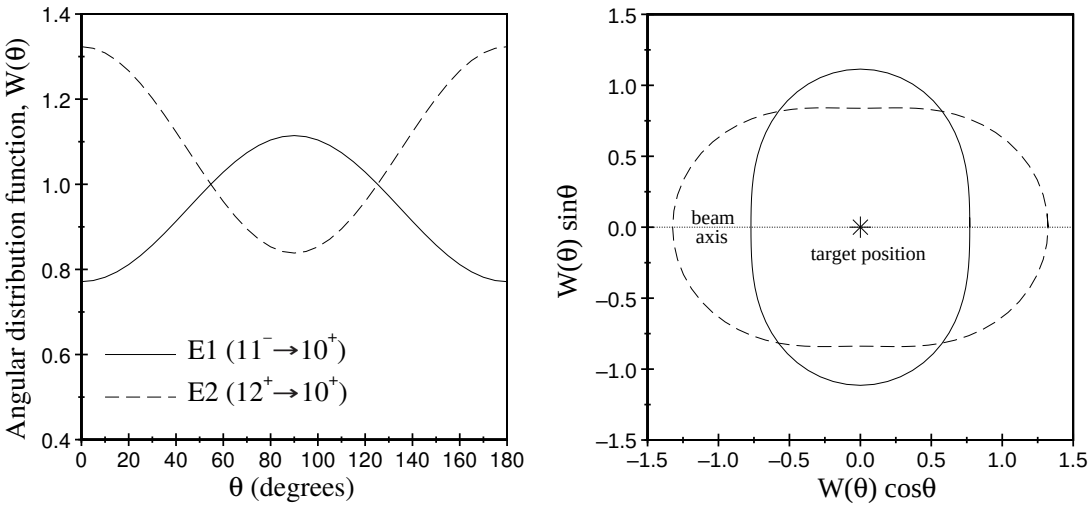

FIGURE 3.7: Angular distributions of typical dipole and quadrupole transitions. From Ref. [58], angular-distribution coefficients of $A_2^{max} = -0.286$ and $A_4^{max} = 0$ have been used for the stretched $E1$ $11^- \rightarrow 10^+$ transition, and for the stretched $E2$ $12^+ \rightarrow 10^+$ transition $A_2^{max} = 0.404$ and $A_4^{max} = -0.161$ have been used. The attenuation coefficients are $\alpha_2 = 0.8$ and $\alpha_4 = 0.5$.

For a mixed $M1/E2$ transition, $\lambda = 1$ and $\lambda' = 2$. For pure $E1$ and $E2$ transitions, $\lambda' = \lambda$, and the multipole mixing ratio δ vanishes. The expression for the angular distribution coefficients can then be simplified to

$$A_K^{max} = B_K(I_i)F_K(I_i\lambda\lambda I_i). \tag{3.6}$$

Examples of the predicted angular distributions for two pure stretched transitions, a dipole and a quadrupole, are shown in Fig. 3.7. They show that the angular distribution of a γ-ray transition can provide a clear experimental signature of its multipolarity. Stretched quadrupoles are most intense along the beam axis, and stretched dipoles at 90° to the the beam axis.

The angular distribution coefficients, A_K, can be extracted from the experimental data by fitting Eq. 3.3 to the intensity seen at different angles, θ. Using the multiple-fold sorting technique already described, gated spectra have been unfolded from the data that correspond to specific rings of detectors in the Gammasphere at a fixed

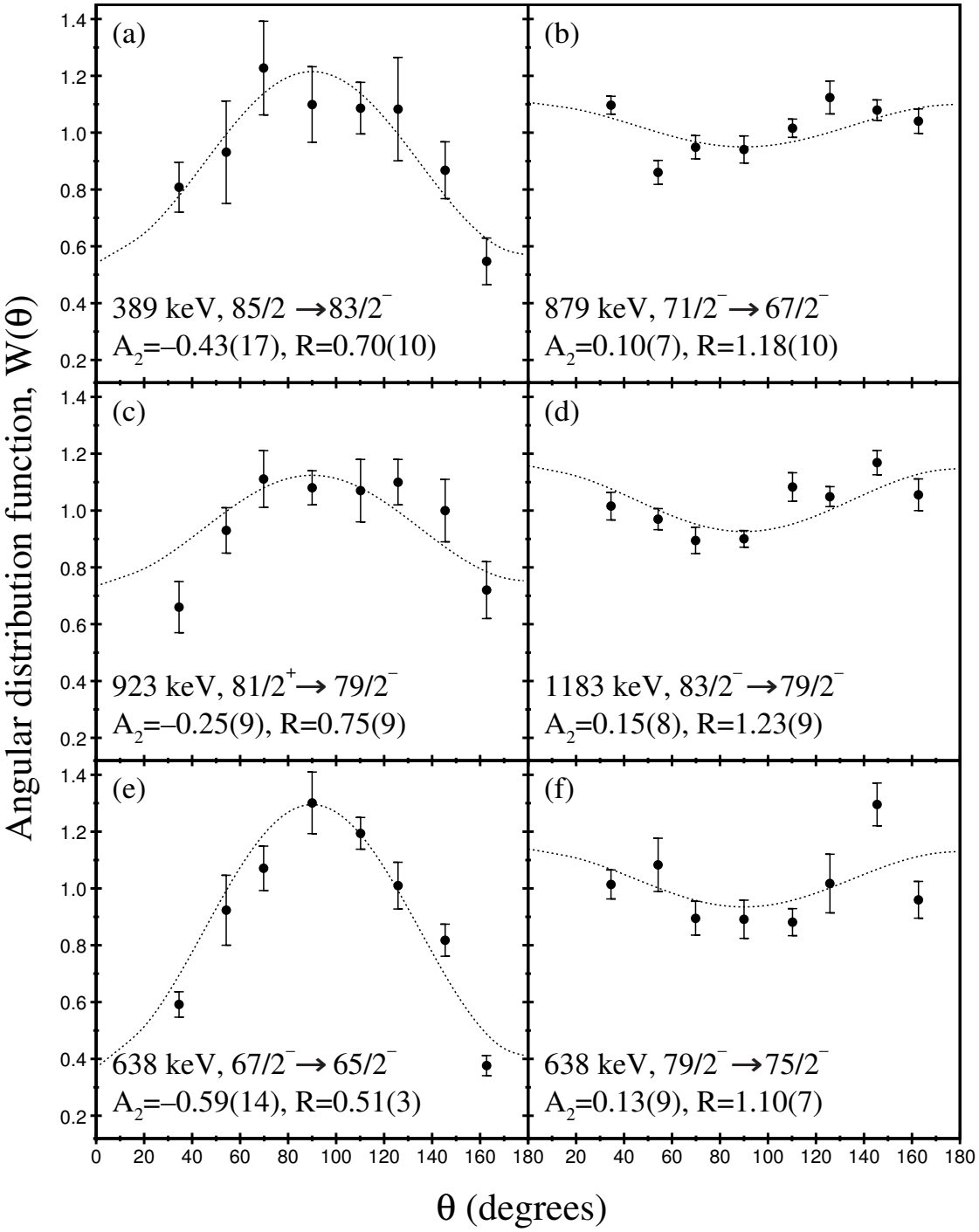

FIGURE 3.8: Examples of angular distributions for transitions in and above band 6 of ^{155}Ho. The curves are fits of the angular-distribution function $W(\theta)$ to the experimental data. As well as the A_2 coefficient corresponding to the fit, the measured angular-intensity ratio, R, is also given for comparison. The plots on the left are for stretched dipole, $I \rightarrow I-1$, transitions, and those on the right are for stretched $E2$, $I \rightarrow I-2$ transitions.

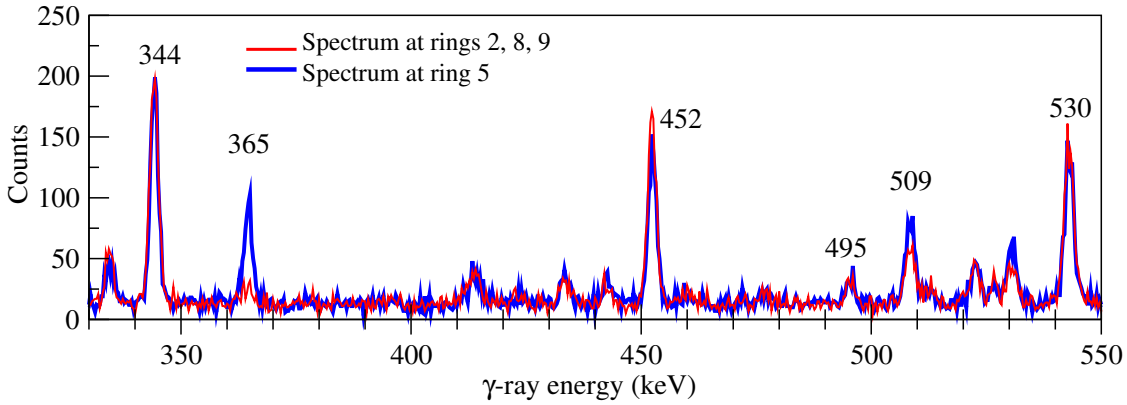

FIGURE 3.9: Comparison of spectra seen at forward and backward rings and at 90°.

angle θ to the beam direction. The rings used are the nine 'summed' rings of Table 3.2. Peak areas for the γ ray of interest are measured for each ring, then normalised to produce experimental $W(\theta)$ values for each ring. To normalise the peak-area measurements, the percentage of the total counts, over all energies, seen at each ring is used. It has been verified that these percentages, shown in Table 3.2, are a good approximation of the relative efficiency of each ring, and that the efficiency of the rings have near identical energy dependence. Examples of measured $W(\theta)$ distributions, and the extracted A_2 values, are shown in Fig. 3.8. For the transitions shown, the A_4 values were set to zero during the fitting process. This is because the experimental uncertainties on the $W(\theta)$ values are too large to reliably fit both parameters, resulting in unphysically large A_4 values regularly being shown to best fit the data.

Rather than extracting the angular-distribution coefficient A_2 in all cases, the preferred method in this work has instead been to measure an angular-intensity ratio, R, for all possible transitions. The spectra of the forward and backward rings 2, 8, and 9 are summed together, then for a particular energy peak the counts seen in this spectrum are divided by the counts seen at ring 5, at $\theta = 90°$. It can be seen from Table 3.2 that the efficiency of these two groups of detectors is approximately equal, meaning no further normalization is required. The angular-intensity ratio is

given by

$$R = \frac{I_\gamma(\text{rings 2, 8 and 9})}{I_\gamma(\text{ring 5})} = \frac{I_\gamma[\theta \approx 150^\circ(30^\circ)]}{I_\gamma[\theta \approx 90^\circ]}. \tag{3.7}$$

Presented alongside the A_2 coefficients in the angular distribution plots of Fig. 3.8 are the measured angular-intensity ratios, R, for each transition. It can be seen that negative angular-distribution coefficients, A_2, generally correspond to ratios R less than unity, and positive A_2 values to R values greater than unity. Experimentally, it is observed that the extracted angular-intensity ratios are typically $\sim$0.7 for a stretched dipole ($\Delta I = 1$) transition, and $\sim$ 1.1 for a stretched quadrupole ($\Delta I = 2$) transition. angular-intensity ratio measurements are presented in Tables 4.1 and 5.1 in the following chapters.

The neat distinction between multipolarities implied by Fig. 3.7 is complicated somewhat the by the presence of mixed transitions. The only mixed transitions of concern in this work are $M1/E2$ transitions, which occur between two states of I and $I - 1$ with the same parity. They typically have a mixing ratio δ approaching zero and, in accordance with Eq. 3.5, have an angular distribution typical of a non-mixed stretched dipole. In some circumstances though, the mixing ratio may be much larger, resulting in a angular distribution more typical of a stretched quadrupole transition. It is also possible to have a negative mixing ratio, which lowers the negative value of the A_2 coefficient further and causes a more exaggerated preference for γ-ray emission along the rotation axis, 90° to the beam. Non-stretched $E1$ transitions ($I \rightarrow I$, with a change in parity), may also cause confusion, having a distribution typical of a stretched quadrupole.

Presented in Fig. 3.9 are spectra for the groups of detectors at the forward and backward positions (rings 2, 8 and 9) and at 90° (ring 5). The sort was performed for transitions in a previously unreported structure in ^{156}Er, band 9. The spectra illustrate how the the angular distribution of transitions can be a good experimental

signature for multipolarity. The 344, 452, 495 and 530 keV transitions all show near equal intensity at the two positions, or a slightly lower intensity at 90°. This is typical of quadrupole transitions with angular-intensity ratios of ~ 1.1. The 509 keV shows a clear preference for emission 90° to the beam, typical of a stretched $E1$ transition, (or mixed $M1/E2$ transition with a small mixing ratio). The intensity of the 365 keV is considerably more intense at 90° than along the beam axis, reflected in its angular-intensity ratio of 0.27, which is much lower than expected for a pure dipole. It has been interpreted as a mixed $M1/E2$ transition with a large negative mixing ratio.

Chapter 4

^{156}Er

Through the observation of γ-ray transitions, many new levels in ^{156}Er are reported in this work, ranging in spin from the lowest to the highest seen in this nucleus. Here, these new states will be interpreted in terms of specific excitations of the ^{156}Er nucleus, in particular bands 2 and 8, which represent the γ-vibrational band and shed light on the nature of the γ deformation of this nucleus.

The nuclide ^{156}Er, with only ten valence particles outside the ^{146}Gd doubly magic core, lies in a 'transitional' region where nuclear collectivity rapidly changes from vibrational to rotational motion [60]. This is reflected in a sharp change in the experimental $E(4^+)/E(2^+)$ energy ratios between $N = 86$ and $N = 96$ nuclei for isotopes with Z around 64, as shown in Fig. 4.1. $E(4^+)/E(2^+)$ ratios of 2.00 and 3.33 are expected for pure vibrational and rotational behaviour, respectively. For the erbium isotopes, ^{154}Er has an $E(4^+)/E(2^+)$ ratio that lies close to the vibrational limit, while ^{160}Er, with only six more valence neutrons, already lies close to the rotational limit. The intermediate ^{156}Er isotope has an $E(4^+)/E(2^+)$ ratio approaching 2.50, the value expected for a γ-soft rotor [37], where vibrational modes of excitation couple to rotation [61].

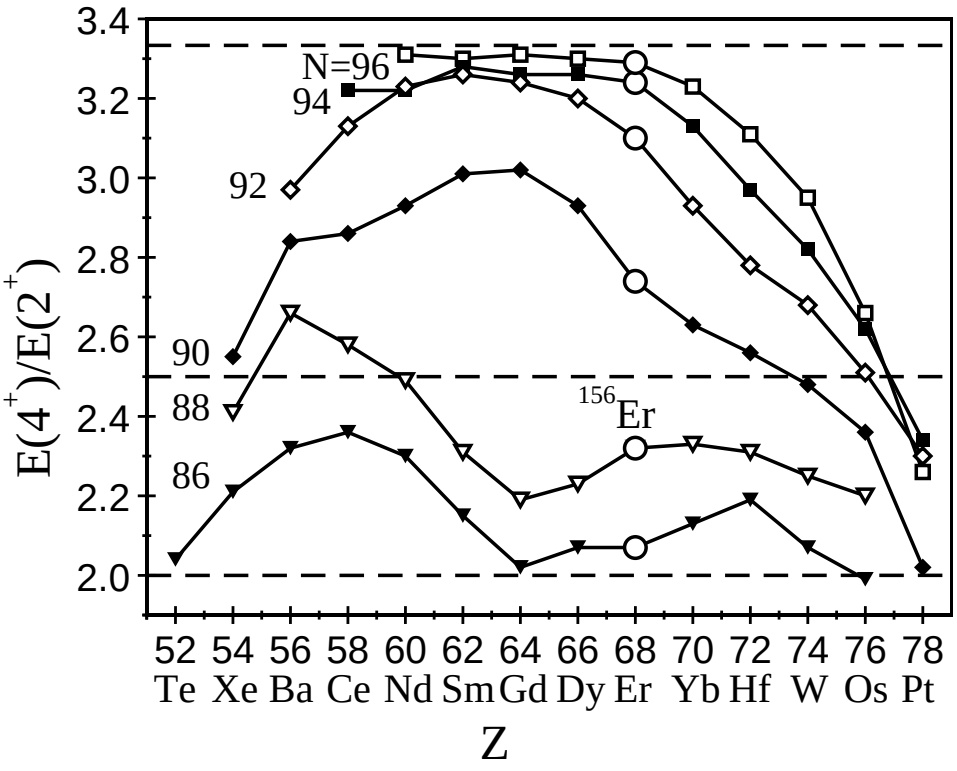

FIGURE 4.1: $E(4^+)/E(2^+)$ energy-ratio systematics for even-even $A \sim 160$ nuclei as a function of atomic number Z. The Er isotopes are denoted by open circles. The horizontal dashed lines represent limits expected for pure vibrational (2.00), rotational (3.33), and γ-soft (2.50) behaviour.

The primary aim of the present experiment was to measure quadrupole moments of superdeformed bands at ultrahigh spin in ^{157,158}Er [55], using the Doppler shift attenuation method [56]. These measurements have been published by Wang *et al.* [62], and have been used to investigate the triaxial nature of strongly deformed bands [63]. Although ^{156}Er nuclei were not excited to such ultrahigh spin states, losing additional angular momentum through the evaporation of an extra neutron, significant new information has also been found in ^{156}Er [4]. The use of a thick, backed target has presented an opportunity to re-evaluate the low-lying ^{156}Er level scheme with the benefit of improved energy resolution resulting from the elimination of the Doppler-broadening component of the photopeak width.

The bulk of the new information has been at relatively low spins, revealing weakly populated non-yrast structures. In particular, a band built on an excited 0^+ state has been established to $(22\hbar)$, while both even and odd signature components of the γ-vibrational band have been identified to $\sim 15\hbar$. The relative energies of the even- and odd- spin states of the γ-vibrational band determine the nature of triaxiality in this nucleus [39], i.e., whether it is γ-rigid or γ-soft. An additional band is discussed as being based on a $\nu h_{9/2}/f_{7/2}$ rotational alignment, coexisting with the systematically observed, more favourable $\nu i_{13/2}$ alignment seen in this mass region. These new low-spin, non-yrast structures are compared with those in neighbouring isotones ($N = 88$) and isotopes ($Z = 68$). They complement a recent, comprehensive high-spin study of ^{156}Er [3], the outcome of a previous, thin target experiment, also performed using the Gammasphere spectrometer.

Also presented here are new transitions found in ^{156}Er at its highest reported angular momentum, above the valence-space terminating state, $I^\pi = 42^+$. These establish the presence of a new high-spin (46^+) state, which is interpreted in terms of particle-hole excitations involving the ^{146}Gd core.

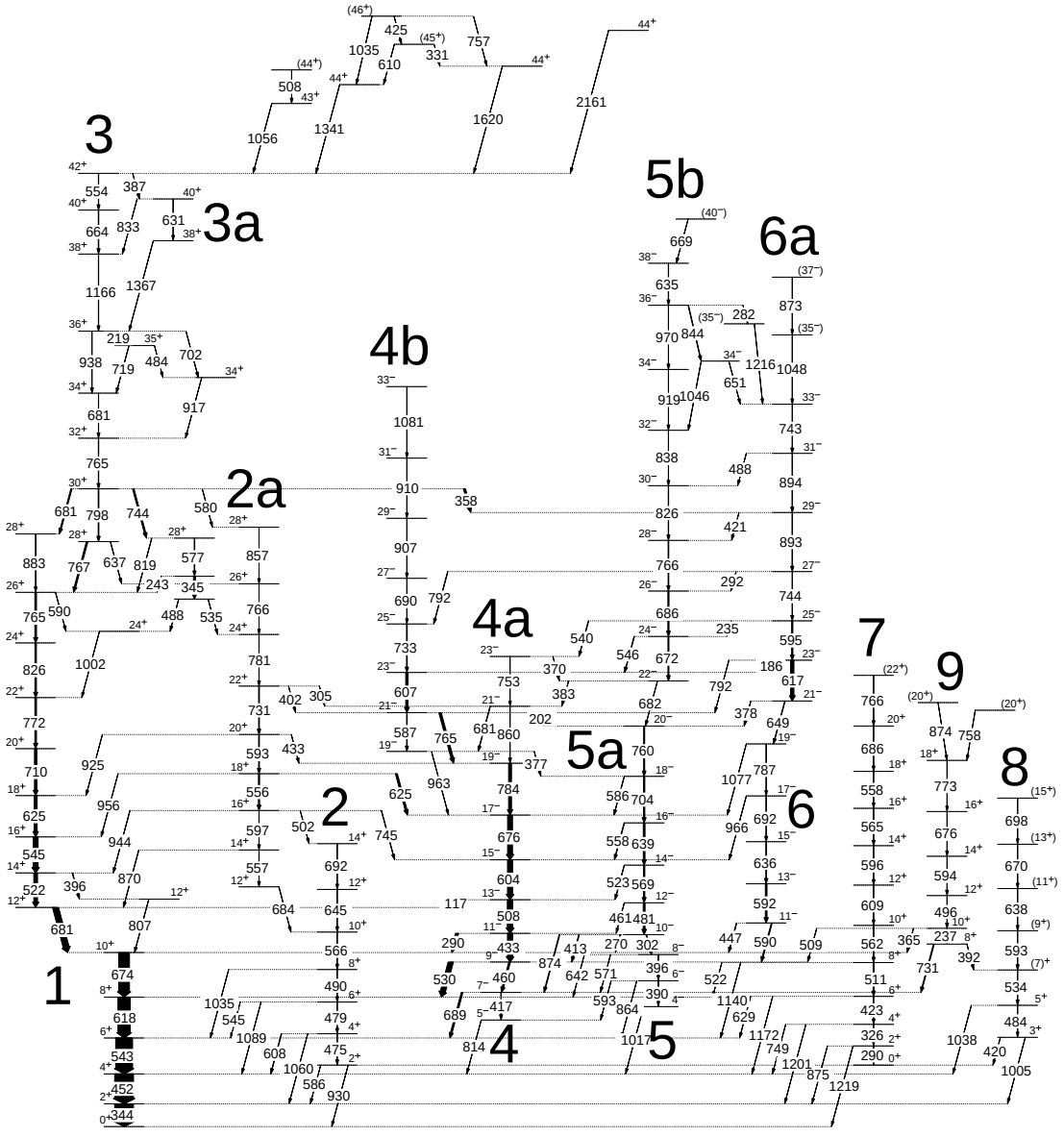

FIGURE 4.2: All levels observed for ^{156}Er from the present work. Energies are labelled in keV and the widths of the arrows are proportional to the transition intensities. The band numbering convention is adopted from Ref. [3].

4.1 Experimental Details and Results

The nucleus ^{156}Er was studied at Argonne National Laboratory, using the Gammasphere spectrometer equipped with 101 HPGe detectors. A ^{48}Ca beam of energy 215 MeV was delivered by the ATLAS facility and used to bombard a 1 mg/cm^2 ^{114}Cd target, backed by a 13 mg/cm^2 layer of ^{197}Au, to produce ^{156}Er via the 6n evaporation channel. An additional 0.07 mg/cm^2 layer of ^{27}Al between the Cd and Au was used to prevent the migration of the target material into the backing. The use of the backed target maintained full γ-ray energy resolution, particularly at low spin, since the vast majority of transitions were emitted after the recoiling nuclei had already stopped and hence were not susceptible to Doppler broadening of the line shapes.

A total of approximately 10^{10} events was accumulated over 12 days of beam time when at least four Compton-suppressed HPGe detectors fired in prompt time coincidence. In the off-line analysis, $\sim 10^{11}$ quadruple-coincident events (γ^4) were unfolded from the raw data and replayed into a RADWARE-format four-dimensional hypercube [48, 49], for subsequent analysis. Transitions corresponding to the three most strongly populated nuclei, ^{156}Er (6n), ^{157}Er (5n), and ^{158}Er (4n) were observed in the hypercube at an approximate ratio of 0.5:1.0:1.0.

4.1.1 New non-yrast levels in ^{156}Er at low to medium spins

The low-lying levels in ^{156}Er are shown in the reduced level scheme, Fig. 4.3. The band numbering convention is adopted from Ref. [3]. Four band structures, labelled 2, 7, 8, and 9 have been established in ^{156}Er with maximum intensities around 0.5% of the 344 keV $2^+ \rightarrow 0^+$ transition. Previously states up to 4^+ were seen in bands 2 and 7 from studies of the radioactive decay of ^{156}Tm; in addition, the 3^+ level of band 8 was identified [64, 65], although subsequent work reassigned this level to 4^+

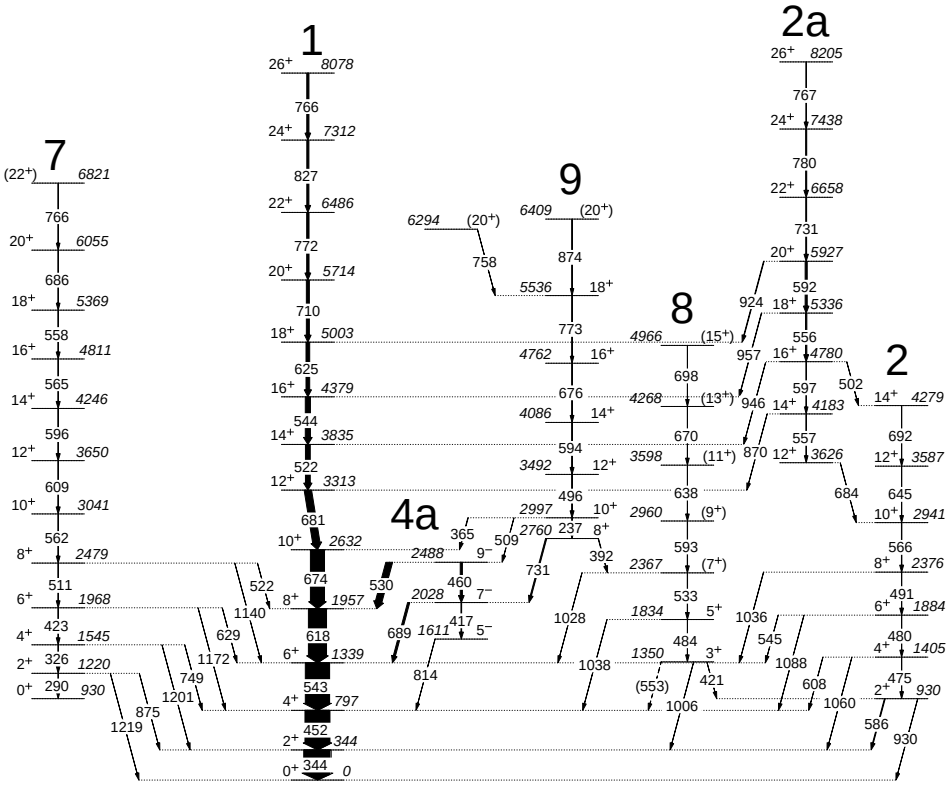

FIGURE 4.3: Partial low-spin level scheme deduced for ^{156}Er from the present work showing new bands 2, 7, 8, and 9 in relation to known bands 1, 2a, and 4a [3]. Energies are labelled in keV and the widths of the arrows are proportional to the transition intensities.

[66]. Band 2 has been extended to $I^\pi = 14^+$ and band 7 to $I^\pi = (22^+)$. Both decay into band 1, the ground-state band, via a series of $\Delta I = 2$ and $\Delta I = 0$ transitions. The levels of band 9 are newly identified in the present study. The coincident γ-ray spectra of Fig. 4.4 show the new transitions in bands 8 and 9, respectively.

To assist in assigning spins and parities in the level scheme, γ-ray multipolarities were extracted from the data by conducting an angular-correlation analysis using the methods described in Chapter 3. An angular-intensity ratio,

$$R = \frac{I_\gamma[\theta \approx 150^\circ(30^\circ)]}{I_\gamma[\theta \approx 90^\circ]}, \tag{4.1}$$

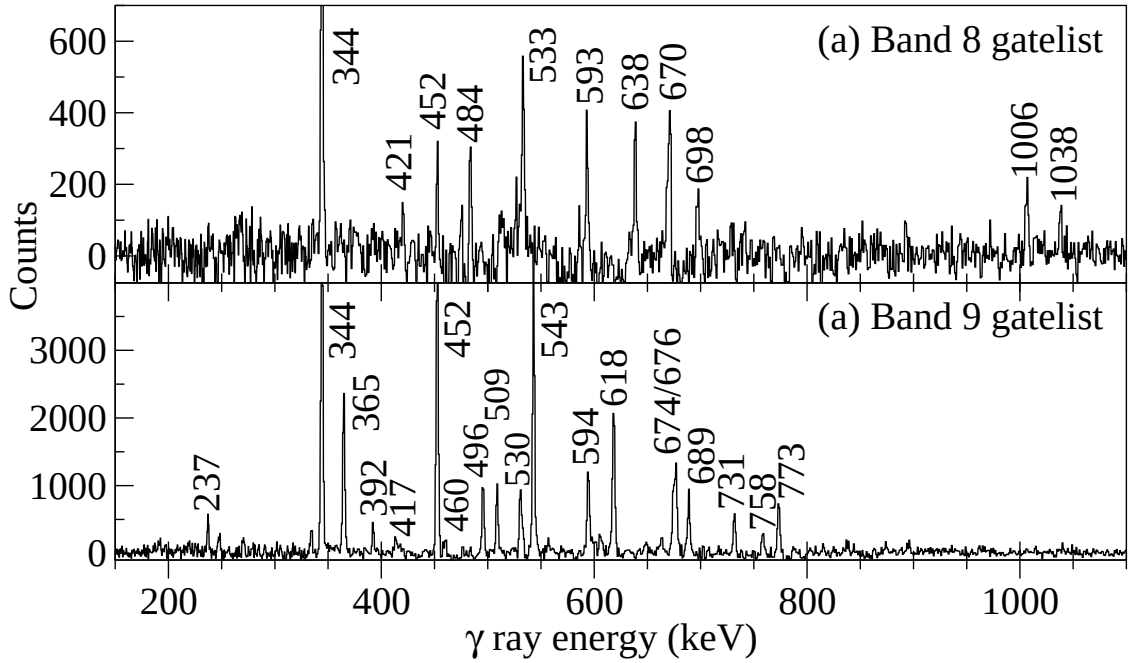

FIGURE 4.4: Triple-gated spectra of quadruple γ-ray events showing transitions in bands 8 and 9.

was evaluated for many of the new γ-ray transitions. Typical angular-intensity ratios extracted from this analysis were $\sim$0.7 for a pure stretched dipole ($\Delta I = 1$) transition, and $\sim$1.1 for a stretched quadrupole ($\Delta I = 2$) transition. Results for the transitions assigned to ^{156}Er reported in this work are listed in Table 4.1.

It has been possible to measure the angular-intensity ratio of most of the band 9 transitions and the 1038 keV transition linking band 8 with the ground-state band, and these are presented in Table 4.1. Angular-intensity ratios of established transitions have been included for reference and comparison. The 0.55 angular-intensity ratio of the 1038 keV transitions strengthens the $I = 5$ assignment of the level at 1834 keV and, by extension, the odd $\alpha = 1$ signature of band 8. The original 3^+ assignment to the level at 1350 keV [64] is therefore confirmed rather than the subsequent 4^+ assignment [66]. This level decays to the 2^+ level of band 2 through a 1006 keV transition, and possibly to the 4^+ level of band 1 through a tentative 553 keV transition.

TABLE 4.1: Intensities, angular-intensity ratios, and spin and parity assignments for transitions in bands 2, 2a, 7, 8 and 9. Results are also included for some known strong E2 and E1 transitions in ^{156}Er.

E_γ (keV)	I_γ	R	Assignment		
	Known $E2$ transitions				
344.2	$\equiv 100$	1.11(5)	2^+	$\rightarrow$	0^+
452.4	61	1.30(6)	4^+	$\rightarrow$	2^+
543.1	57	1.16(6)	6^+	$\rightarrow$	4^+
617.9	54	1.17(9)	8^+	$\rightarrow$	6^+
674.1	47	0.98(19)	10^+	$\rightarrow$	8^+
	Known $E1$ transitions				
530.4	17	0.73(6)	9^-	$\rightarrow$	8^+
688.6	8.3	0.64(19)	7^-	$\rightarrow$	6^+
	Band 2 transitions				
475.0	0.1		4^+	$\rightarrow$	2^+
479.7	0.4		6^+	$\rightarrow$	4^+
490.6	0.5		8^+	$\rightarrow$	6^+
501.6			18^+	$\rightarrow$	16^+
544.7	0.1		6^+	$\rightarrow$	6^+
557.3	0.1		14^+	$\rightarrow$	12^+
565.8	0.4		10^+	$\rightarrow$	8^+
585.5	0.1		2^+	$\rightarrow$	2^+
596.7	0.1		16^+	$\rightarrow$	14^+
608.1	0.3		4^+	$\rightarrow$	4^+
645.2	0.1		12^+	$\rightarrow$	10^+
684.3	0.1		12^+	$\rightarrow$	10^+
692.1	0.1		14^+	$\rightarrow$	12^+
870.4			14^+	$\rightarrow$	12^+
930.4			2^+	$\rightarrow$	0^+
1036.3	0.3		8^+	$\rightarrow$	6^+
1060.0	0.1		4^+	$\rightarrow$	2^+
1088.4	0.1		6^+	$\rightarrow$	4^+

TABLE 4.1 CONTINUED.

E_γ (keV)	I_γ	R	Assignment		
		Band 7 transitions			
289.5			2^+	$\rightarrow$	0^+
325.5			4^+	$\rightarrow$	2^+
422.9	0.6	1.18(12)	4^+	$\rightarrow$	2^+
510.9	0.8		8^+	$\rightarrow$	6^+
521.8	0.1		8^+	$\rightarrow$	8^+
557.7		1.10(13)	18^+	$\rightarrow$	16^+
561.7	0.7	1.04(9)	10^+	$\rightarrow$	8^+
565.4	0.1	1.09(6)	16^+	$\rightarrow$	14^+
596.2	0.2	1.14(11)	14^+	$\rightarrow$	12^+
608.9	0.3		12^+	$\rightarrow$	10^+
628.6	0.3	0.79(20)	6^+	$\rightarrow$	6^+
686.5		1.29(24)	20^+	$\rightarrow$	18^+
748.7	0.2	0.65(23)	4^+	$\rightarrow$	4^+
766.0			$(22)^+$	$\rightarrow$	20^+
875.4			2^+	$\rightarrow$	2^+
1139.7	0.2		8^+	$\rightarrow$	6^+
1172.1	1.1	1.08(43)	6^+	$\rightarrow$	4^+
1201.2	1.0	0.94(26)	4^+	$\rightarrow$	2^+
1219.4			2^+	$\rightarrow$	0^+
		Band 8 transitions			
420.6	0.2		3^+	$\rightarrow$	2^+
483.7	0.6		5^+	$\rightarrow$	3^+
533.5	0.6		(7^+)	$\rightarrow$	5^+
(553.4)	0.1		3^+	$\rightarrow$	4^+
592.7	0.5		$(9^+$	$\rightarrow$	$7^+)$
638.0	0.3		$(11^+$	$\rightarrow$	$9^+)$
670.5	0.2		$(13^+$	$\rightarrow$	$11^+)$
697.6	0.1		$(15^+$	$\rightarrow$	$13^+)$
1006.0	0.4		3^+	$\rightarrow$	2^+
1027.8			(7^+)	$\rightarrow$	5^+
1038.0	1.4	0.55(9)	5^+	$\rightarrow$	4^+

TABLE 4.1 CONTINUED.

E_γ (keV)[a]	I_γ[b]	R[c]	Assignment		
		Band 9 transitions			
237.2	0.1	1.31(24)	10^+	$\rightarrow$	8^+
364.6	0.6	0.27(3)	10^+	$\rightarrow$	10^+
392.4	0.3		8^+	$\rightarrow$	(7^+)
495.6	0.3	1.12(14)	12^+	$\rightarrow$	10^+
508.6	0.3	0.76(5)	10^+	$\rightarrow$	9^-
593.9	0.3	1.28(12)	14^+	$\rightarrow$	12^+
676.4	0.2	0.97(20)	16^+	$\rightarrow$	14^+
731.4	0.8	1.01(14)	8^+	$\rightarrow$	7^-
758.3			(20^+)	$\rightarrow$	18^+
773.1	0.1	1.05(18)	18^+	$\rightarrow$	16^+
873.8			(20^+)	$\rightarrow$	18^+

[a] The γ-ray energies are estimated to be accurate to $\pm$0.3keV.
[b] Intensities quoted as a percentage of the 344 keV ($2^+ \rightarrow 0^+$) γ ray. Errors are estimated to be less than 20% of the quoted values.
[c] Angular intensity ratios, R. Pure stretched dipoles typically have $R = 0.7$, while quadrupoles have $R = 1.1$.

The band 9 transitions of energies 496, 594, 676, and 773 keV all have angular-intensity ratios of around 1.2, which suggests they are stretched quadrupole transitions. The same is true for the 237 keV transition with a ratio of 1.3 although a non-stretched dipole cannot be ruled out. This implies the levels at energies of 2761 and 2998 keV are separated in spin by 0 or 2. The 365 keV transition, connecting the 2998 keV level of band 9 to the yrast 10^+ state of band 1, has a particularly low ratio of 0.27. This value is too low for a pure dipole ($E1$, $\Delta I = 0, 1$) transition, so the transition probably corresponds to an $M1/E2$ transition with a large negative mixing ratio, using the sign convention of Ref. [58]. The state at 2998 keV in band 9 could then be assigned 9^+ or 10^+ or 11^+. The 11^+ assignment can be rejected since band 9 would be too yrast and would have to decay to negative-parity band 4a through hindered stretched $M2$ transitions. The 509 keV transition, feeding the 9^- level of band 4a, has an angular-intensity ratio consistent with a pure stretched

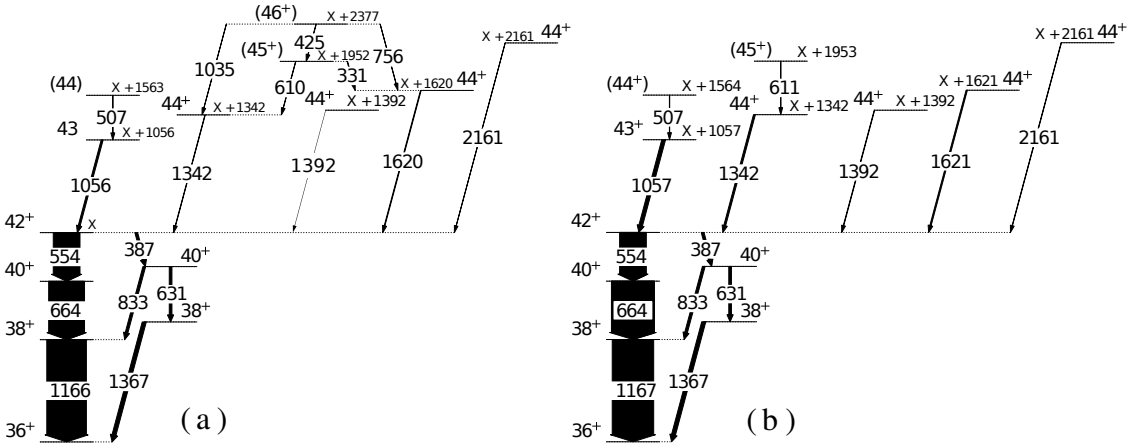

FIGURE 4.5: (a) High-spin level scheme deduced for ^{156}Er from the present work, and (b) previously known level scheme [3]. Energies are labelled in keV, and the level energies are given relative to the 42^+ terminating state. The widths of the arrows are proportional to the transition intensities.

($\Delta I = 1$) dipole and is hence assigned to have $E1$ character. This then fixes the 2998 keV state to have 10^+ and consequently the band-head of band 8 to have spin and parity 8^+. The 731 keV transition which decays from the 8^+ band-head to the 7^- state of band 4a has a high angular-intensity ratio (1.01) but the large error bar means that it is not inconsistent with a stretched $E1$ assignment.

4.1.2 New high-spin information in ^{156}Er

Four previously unreported transitions at high spin have been observed in ^{156}Er as part of this work, of energy 331, 425, 757, and 1035 keV. A reduced level scheme showing the high spin levels in ^{156}Er observed in this work, including the 42^+ terminating state at the top of band 3 and the excitations above it, is shown in Fig. 4.5(a). For comparison, the previously known level scheme from Ref. [3] is shown in Fig. 4.5(b). The newly observed 331 keV transition supports the previous observation of a (45^+) state 1951 keV above the 42^+ terminating state. Seen in coincidence with the 331, 610, 1341, and 1620 keV transitions, there is a γ ray of energy 425 keV, indicating that there exists a further level at 2377 keV above the

TABLE 4.2: Transitions near valence space band termination in ^{156}Er. Intensities are normalized to the 554 keV ($42^+ \rightarrow 40^+$) transition of band 3, which carries 2% of the 344 keV ($2^+ \rightarrow 0^+$) transition.

E_γ (keV)	$I_i^\pi \rightarrow I_f^\pi$			Relative Intensity (%)
		Known transitions		
507	(44)	$\rightarrow$	43	3.6(3)
554	42^+	$\rightarrow$	40^+	$\equiv 100$
610	(45^+)	$\rightarrow$	44^+	< 1
1057	43	$\rightarrow$	42^+	7.2(5)
1341	44^+	$\rightarrow$	42^+	1.38(12)
1620	44^+	$\rightarrow$	42^+	2.45(22)
2161	44^+	$\rightarrow$	42^+	< 1
		New transitions		
331	(45^+)	$\rightarrow$	44^+	1.70(13)
425	(46^+)	$\rightarrow$	(45^+)	< 1
756	(46^+)	$\rightarrow$	44^+	< 1
1035	(46^+)	$\rightarrow$	44^+	< 1

42^+ state, labelled (46^+). Spectra illustrating these coincidence relations are shown in Fig. 4.6. The presence of the (46^+) level is confirmed through the observation of two γ rays of energy 1035 keV and 757 keV, which are seen in coincidence with the 1321 keV and 1620 keV transition, respectively

These newly observed transitions are very weakly populated, with maximum intensities $\sim 1\%$ of the 554 keV $42^+ \rightarrow 40^+$ transition at the top of band 3, which itself only carries around 2% of the intensity of the 344 keV $2^+ \rightarrow 0^+$ transition. Although these transitions were too weak to perform an angular-correlation analysis, the decay of the new state into two 44^+ states – directly and via the (45^+) state – is consistent with a spin-parity assignment of $I^\pi = (46^+)$. The proposed (46^+) assignment is partly based on an assumption that each γ ray represents a decay from a level of higher spin. However, it is possible that the new state is not yrast and the reported transitions are non-stretched, representing decays from less favoured structures of lower angular momentum. The previously observed high-spin transitions were all confirmed here. The hypercube did not extend high enough in

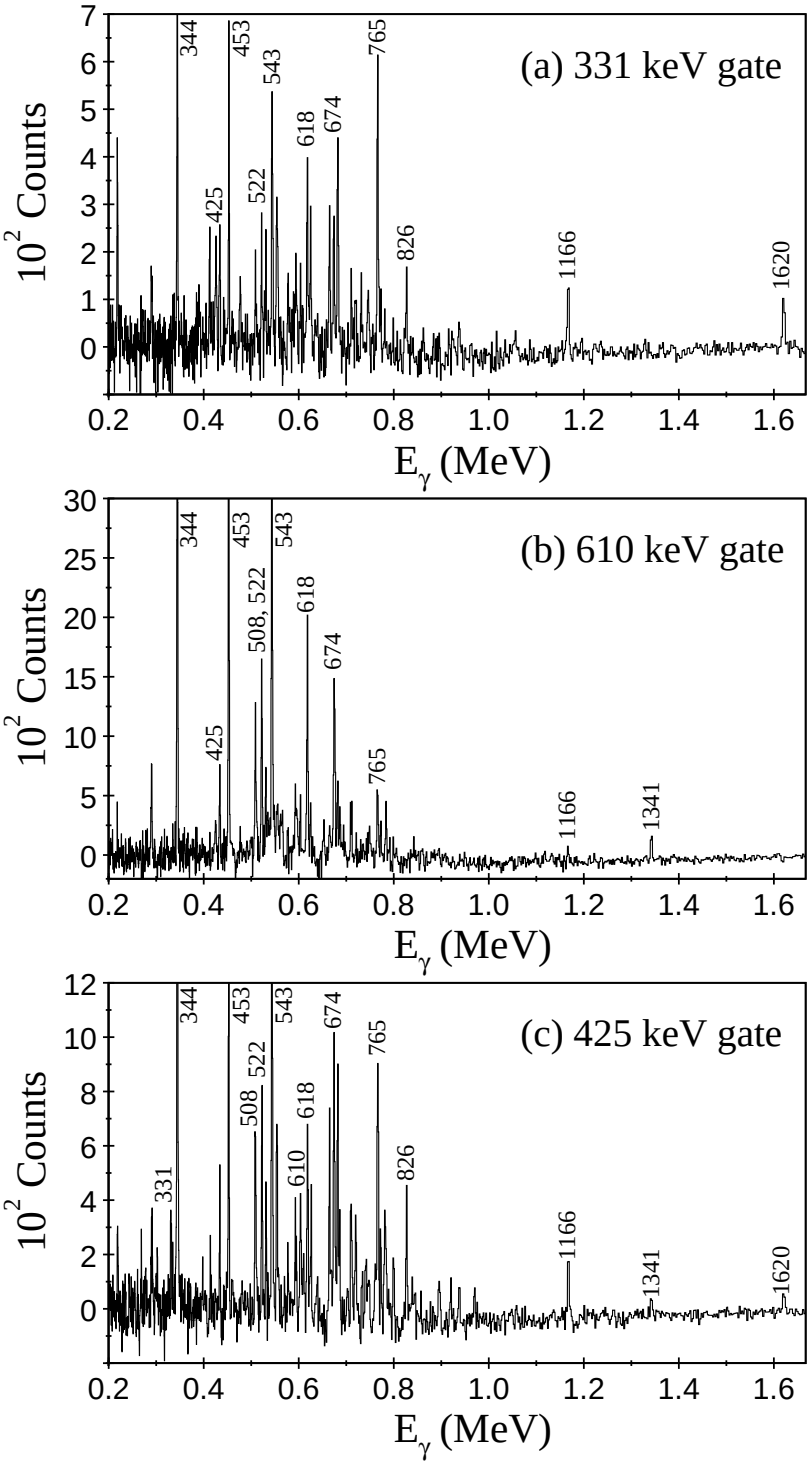

FIGURE 4.6: Triple-gated quadruple-coincidence spectra for ^{156}Er. In all three cases, a list of transitions in bands 1 and 3 has been used as the gating condition on two axes of the hypercube. On the third axis, a gate has been set at (a) 331 keV, (b) 610 keV, and (c) 425 keV. The 331 keV γ ray is coincident with 1620 keV, the 610 keV γ ray with 1341 keV, and 425 keV is seen in coincidence with both. In each spectrum, the transitions are labelled by their energies in keV.

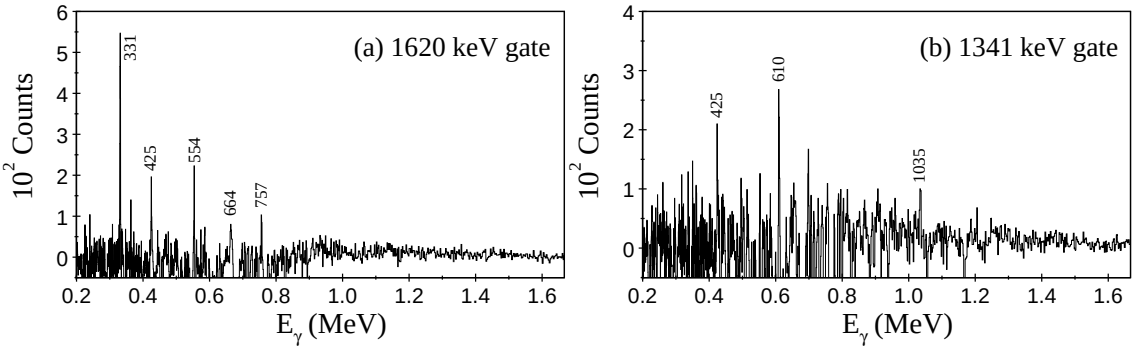

FIGURE 4.7: Triple-gated quadruple-coincidence spectra for ^{156}Er. In both cases, a list of transitions in bands 1 and 3 has been used as the gating condition on two axes of the hypercube. On the third axis, a gate has been set at (a) 1620 keV and (b) 1341 keV. The transitions at the top of the the ^{156}Er level scheme (see Fig. 4.5) can be seen. In each spectrum, the transitions are labelled by their energies in keV.

energy for the 2161 keV transition to be observed, but it was seen in multiple-fold sorted spectra, and is shown in the example presented in Chapter 3, Fig. 3.5. The 1056 keV, 1341 keV, 1392 keV, and 1620 keV transitions can also be seen in these spectra.

4.2 Discussion

The rotational model [26] that couples together both collective rotations and vibrations [61] is appropriate for the description of ^{156}Er. In addition, this nucleus has been discussed [67] in the context of the interacting boson model (IBM) [68].

The $E(4^+)/E(2^+)$ ratio of 2.32 for ^{156}Er (see Fig. 4.1) lies above the U(5) vibrational limit of this model (2.00), but below the SU(3) rotational limit (3.33); the ratio is in fact nearer to the O(6) limit for a γ-soft rotor (2.50). The second 0^+ and 2^+ states are degenerate, at an excitation energy of 930 keV [65]. Moreover, they lie close to the yrast 4^+ energy, as expected for a U(5) vibrator.

Recent theoretical work using the triaxial projected shell model [69] has also focused on the theoretical description of γ-vibrational bands in the light erbium isotopes, where they are predicted to become close to yrast at high spin.

4.2.1 Systematics of second 0^+ states

The lowest levels of band 7 were originally associated with a $K^\pi = 0^+$ β-vibrational band [64]. However, due to the low excitation energy of the 0^+ band-head (930 keV), such an interpretation has subsequently been questioned [70]. Other interpretations have also been proposed for low-lying 0^+ levels, including pairing isomers [71] and a second vacuum formed by particle-hole excitations [72, 73, 74]. Energy systematics of the first excited 0^+ states in $N = 88$ isotones and $Z = 68$ isotopes [75] are shown in Fig. 4.8, where $E(0_2^+)/E(2_1^+)$ ratios are plotted. The lowest-lying second 0^+ state in these particular nuclei occurs in ^{152}Gd, an isotope with a semi-magic $Z = 64$ protons. The largest ratio occurs in ^{166}Er with 98 neutrons.

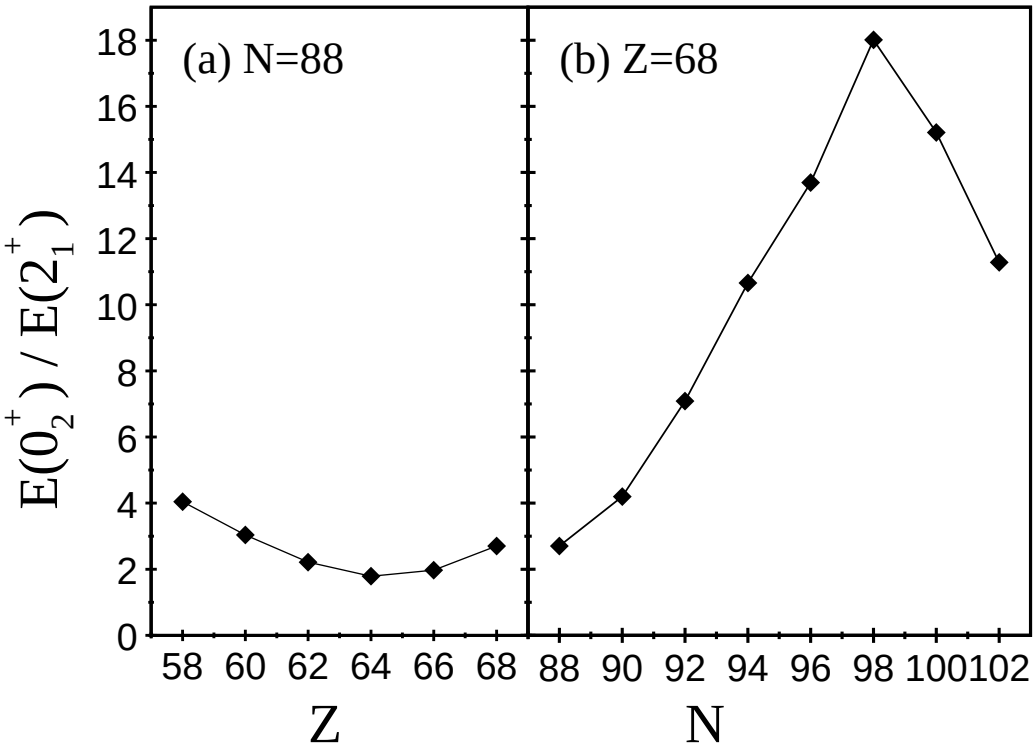

FIGURE 4.8: Energy ratios $E(0_2^+)/E(2_1^+)$ for (a) $N = 88$ isotones and (b) $Z = 68$ isotopes.

4.2.2 Systematics of γ-vibrational states

In this work, bands 2 and 8 are interpreted as the two signature components of the $K^\pi = 2^+$ γ-vibrational band in ^{156}Er. The low-lying γ-vibrational band energies are plotted in Fig. 4.9 for $N = 88$ isotones and the erbium isotopes ($Z = 68$)[75, 77, 78], together with the energies of the first 2_1^+, 4_1^+ and $6+_1$ levels of the ground-state band and the second 0^+ state. For the $N = 88$ isotones, Fig. 4.9(a), the second 0^+ state lies well below the 2_γ^+ band-head, except for ^{156}Er ($Z = 68$), where the two become degenerate. Moreover, the second 0^+ state also falls below the 4^+ state for Z = 62-66 (^{150}Sm, ^{152}Gd and ^{154}Dy). For the erbium isotopes, Fig. 4.9(b), the second 0^+ state and the 2_γ^+ levels remain close together for Z = 88-92 (^{156,158,160}Er), before the second 0^+ state rapidly rises in energy. The second 0^+ energy peaks for N=98 (166Er), which also has the lowest γ-vibrational energies, before dropping

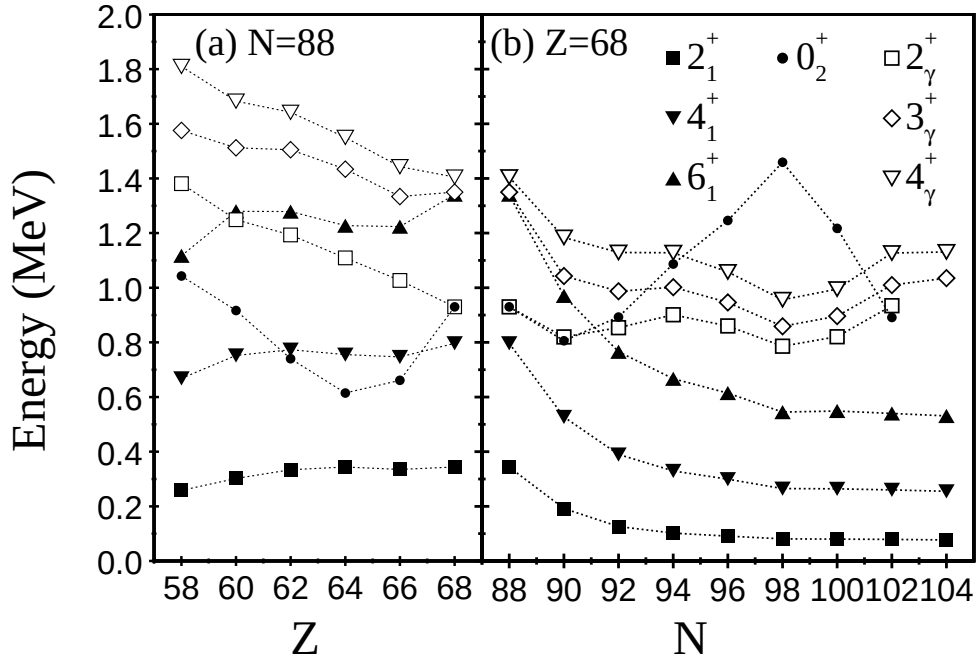

FIGURE 4.9: Systematic energies of the lowest γ-vibrational levels and 0_2^+ states in (a) $N = 88$ isotones and (b) $Z = 68$ isotopes, relative to the nuclear ground state. The 2_1^+, 4_1^+ and 6_1^+ levels of the ground-state band are also included. Note that the 0_2^+ and 2_γ^+ levels are degenerate in ^{156}Er ($Z = 68$, $N = 88$), and also lie close to the 4_1^+ state.

for the heavier isotopes. This could indicate a change of intrinsic structure for the second 0^+ state in these heavier isotopes, e.g., an intruder configuration [79]. The second 0^+ state even falls below the 2_γ^+ level for $N = 102$ (^{170}Er), but has not been experimentally identified for $N = 104$ (^{172}Er). In ^{156}Er, the degenerate 0^+ state and 2_γ^+ states also lie close to the yrast 4^+ state, as expected for a vibrational nucleus [22].

4.2.3 Nature of the triaxiality

The energy staggering between the even- and odd-spin energies of levels in the γ-band can provide an insight into the nature of the nuclear triaxiality [39]. In particular, the energy staggering can distinguish between rigid and γ-soft and triaxial shapes. Rigid triaxial nuclear shapes are described by the asymmetric-rotor model

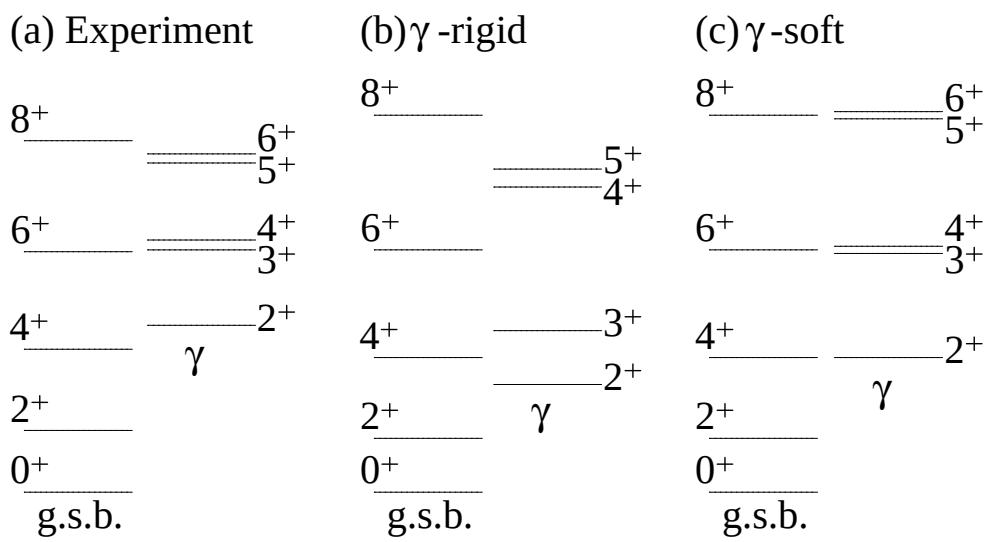

FIGURE 4.10: Comparison of the energy of the ground-state band (g.s.b.) and energy staggering of (a) the experimental γ-band proposed in this work, with schematic staggering [39] predicted by (b) the γ-rigid asymmetric-rotor model and (c) the γ-soft rotor model.

(ARM) of Davydov and Filippov [35], in which the potential has a well-defined minimum at a particular value of γ.

The other possibility, that there is not static triaxial deformation, but instead dynamic oscillations in γ, is described in its most extreme case by the Wilets-Jean model [36]. As discussed in Chapter 2, this model considers complete γ-instability, described by a nuclear potential that has a finite favoured β value, but is completely flat with respect to γ; the nucleus in effect oscillates uniformly between $\gamma = 0°$ (prolate) and $\gamma = 60°$ (oblate).

In the rigid triaxial case, γ-band levels appear in doublets as $(2^+_\gamma - 3^+_\gamma)$, $(4^+_\gamma - 5^+_\gamma)$, $(6^+_\gamma - 7^+_\gamma)\ldots$, but the γ-soft case results in a 2^+_γ, $(3^+_\gamma - 4^+_\gamma)$, $(5^+_\gamma - 6^+_\gamma)\ldots$ pattern [37, 80]. The predicted level structures are shown schematically in Fig. 4.10 for the Davydov model at $\gamma = 30°$ and for the Wilets-Jean model with $\bar{\gamma} = 30°$. The reduced experimental level scheme, Fig. 4.10(a), clearly has the energy staggering predicted by the γ-soft model. A more quantitative approach involves measuring

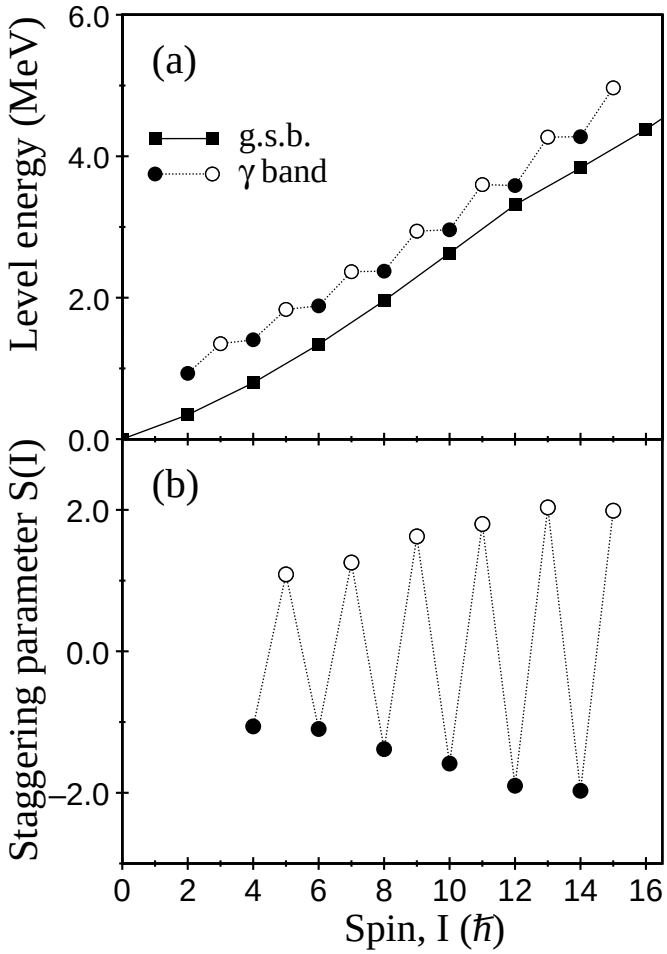

FIGURE 4.11: (a) Level energies of the ground-state band and γ-vibrational band in ^{156}Er, plotted as a function of spin. (b) $S(I)$ values of the γ-vibrational band plotted as a function of spin.

the staggering parameter [22] of the band, defined for spin I as

$$S(I) = \frac{[E(I) - E(I-1)] - [E(I-1) - E(I-2)]}{E(2_1^+)}. \tag{4.2}$$

The ground-state band and γ-vibrational band energies, together with the energy staggering parameter $S(I)$, are shown in Fig. 4.11. It can be seen that the energy staggering persists up to the highest spins.

Systematics of the $S(4)$ values are shown in Fig. 4.12. Rotation of a γ-rigid triaxial shape with $\gamma = 0°$, i.e., an axially symmetric prolate nucleus, yields a value

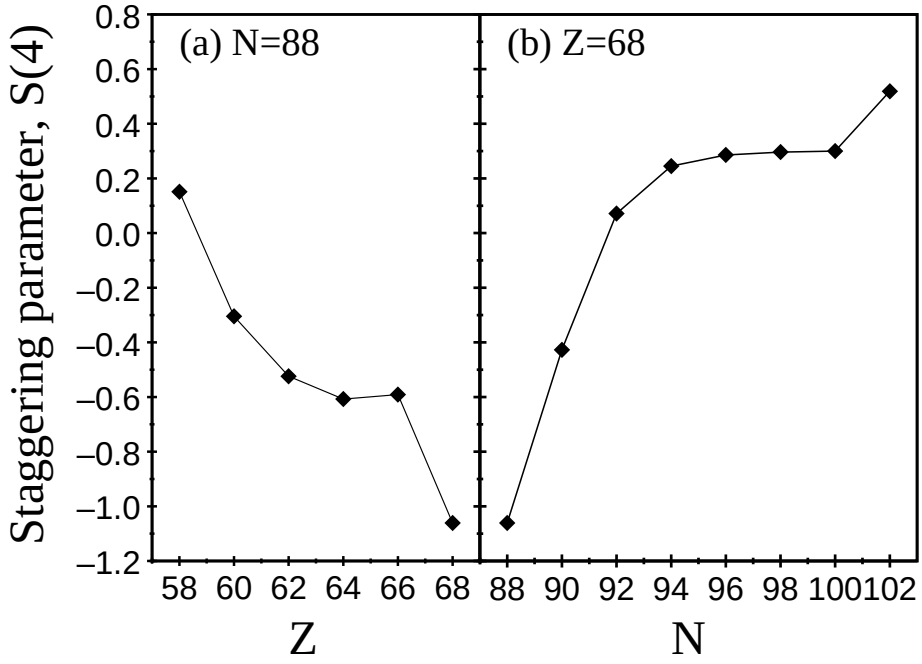

FIGURE 4.12: Measured $S(4)$ values for (a) $N = 88$ isotones and (b) $Z = 68$ isotopes.

of $S(4) = 0.33$. However, a γ-rigid rotor with γ-rigid rotor with $\gamma = 30°$ is predicted to have an $S(4)$ value of +1.67 while a γ-soft rotor with $\bar{\gamma} = 30°$ has an $S(4)$ value ~ -1.0 [39].

It can be seen in Fig. 4.12 that the $S(4)$ value for ^{156}Er is very close to –1.0, and is the lowest amongst these particular erbium isotopes and $N = 88$ isotones. Thus ^{156}Er is an ideal candidate for the archetypal γ-soft rotor. Furthermore, the heavier Er isotopes quickly approach the limit of $S(4) = 0.33$, expected for rigid-γ behaviour. Taken with the energy systematics of Fig. 4.1, this shows that the Er isotopes above ^{156}Er rapidly change from rotation-vibration (γ-soft) behaviour to deformed rotational (prolate) behaviour. This can be explained by the neutron Fermi surface moving into the deformation-driving $\nu i_{13/2}$ subshell. The $S(4)$ value increases above 0.33 for ^{170}Er ($N = 102$), indicating a lowering of the odd-spin γ-vibrational band members relative to the even-spin members. Such a situation suggests the onset of (rigid) triaxiality – see Fig. 4.10(b). It can also be seen in

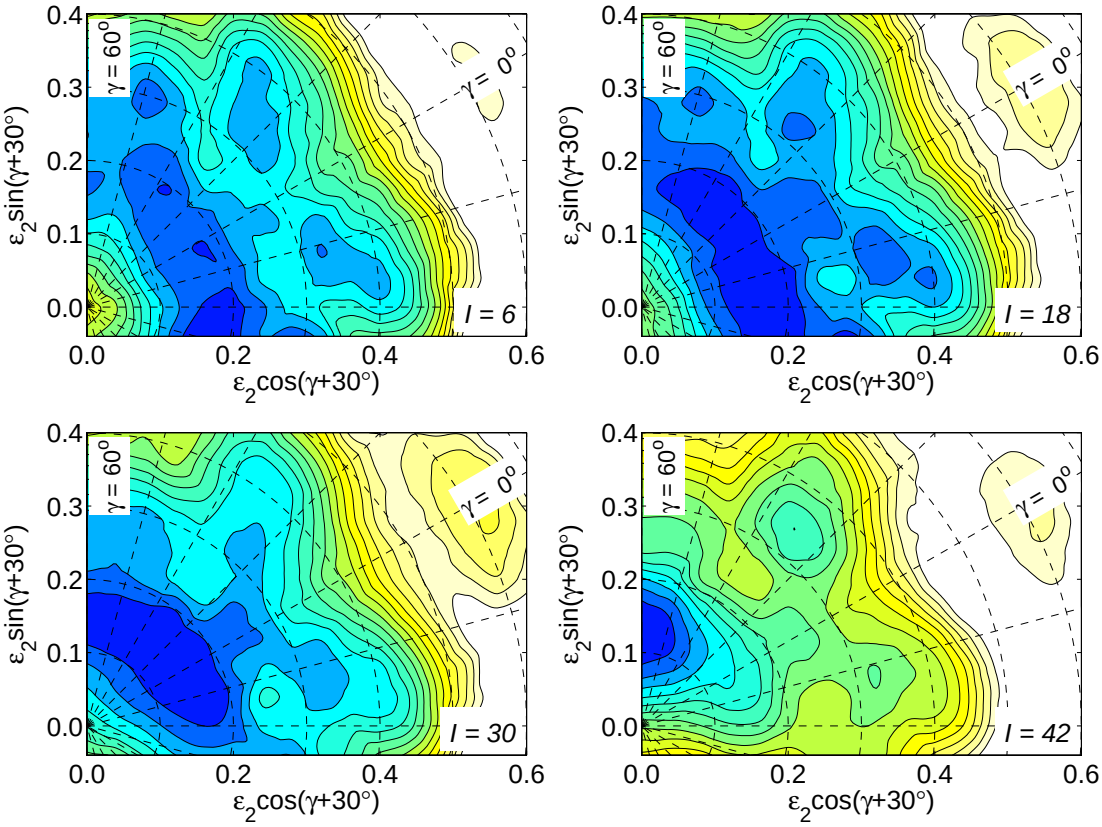

FIGURE 4.13: Calculated potential energy surfaces of ^{156}Er with $(\pi, \alpha) = (+, 0)$ for spin values $I = 6$, 18, 30, and 42. The contour lines are separated by 0.5 MeV, with darker shades (blue) lower in energy than lighter shades (green-yellow). Reprinted from Ref. [3], calculations performed by I. Ragnarsson [76].

Fig. 4.9(b) that the second 0^+ state becomes near degenerate with the 2^+_γ band-head for this isotope.

The calculated potential energy surfaces of Fig. 4.13 show a prolate deformed minimum at low spin, with $\varepsilon_2 \approx 0.2$. However, the potential is markedly flat with respect to γ in the $0^\circ \leq \gamma \leq 60^\circ$ regime, supporting the γ-soft interpretation of ^{156}Er.

4.2.4 Alignment properties of the bands

The energy levels of the new band structures in ^{156}Er are plotted in Fig. 4.14 as a function of spin, where they are compared with those of the ground-state band

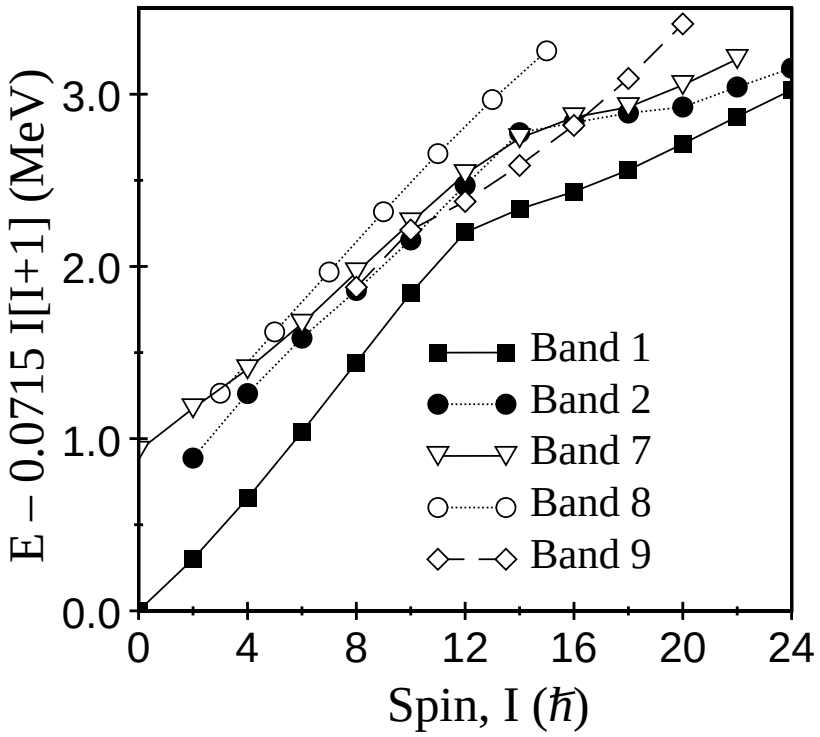

FIGURE 4.14: Energies of the low-spin bands in ^{156}Er, plotted as a function of spin, relative to a rotating liquid-drop reference.

(band 1). A rigid body reference of $C.I(I+1)$ has been subtracted from the total energy, using $C = 0.00715$, the default value of $C = 0.007$ MeV for $A = 158$ scaled according to the rigid body moment of inertia, i.e. as $A^{-5/3}$ [5]. The changes in slope represent rotational alignment of specific quasiparticle pairs.

In order to investigate the rotational properties of the new bands in ^{156}Er, the experimental alignments [27],

$$i_{\mathrm{x}}(\omega) = I_{\mathrm{x}}(\omega) - I_{\mathrm{x,ref}}(\omega), \tag{4.3}$$

are shown in Fig. 4.15, plotted as a function of rotational frequency, $\omega = E_\gamma/\Delta I_x \approx E_\gamma/2\hbar$. At a given spin I, the aligned spin is $I_{\mathrm{x}} = \sqrt{I(I+1) - K^2}$, while the

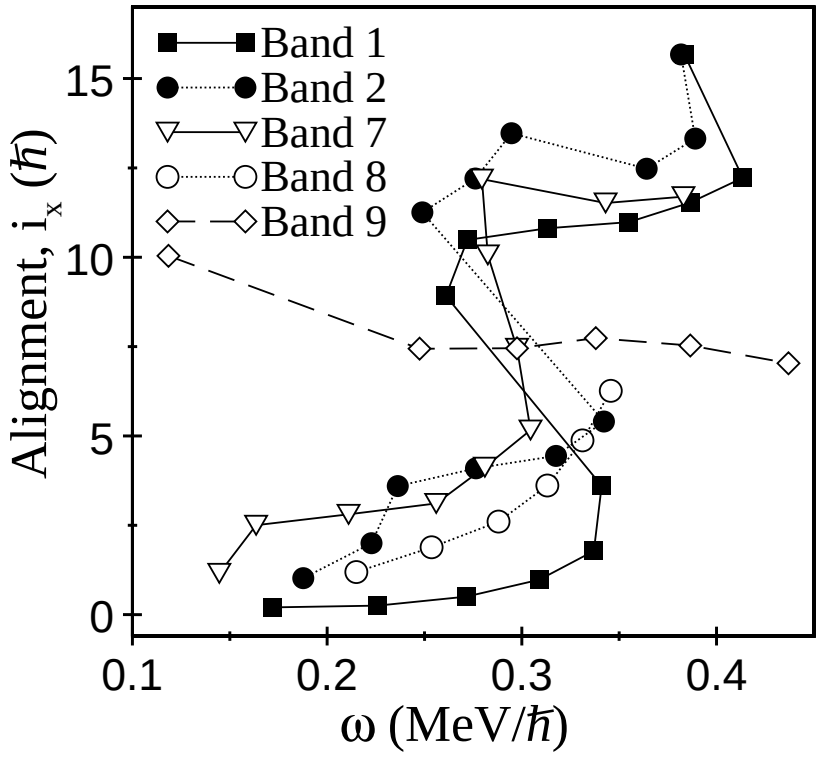

FIGURE 4.15: Experimental alignments, i_x, as a function of rotational frequency, ω, for positive-parity bands in ^{156}Er.

rotational reference, $I_{\mathrm{x,ref}}$, is given by

$$I_{\mathrm{x,ref}}(\omega) = \omega(\mathcal{J}_0 + \mathcal{J}_1\omega^2) - i_0. \tag{4.4}$$

Harris parameters [31] $\mathcal{J}_0 = 32.1\ \hbar^2\mathrm{MeV}^{-1}$ and $\mathcal{J}_1 = 34.0\ \hbar^4\mathrm{MeV}^{-3}$, obtained from ^{157}Ho [81], have been used together with a positive offset $i_0 = 4.4\hbar$ in order to ensure that the ground-state band of ^{156}Er has approximately zero alignment at low rotational frequency [3]. For the γ-vibrational bands (bands 2 and 8), $K = 2$ was used and elsewhere $K = 0$.

Band 1 gains 10-11$\hbar$ of alignment at a rotational frequency of approximately 0.3 MeV/$\hbar$. In addition bands 2 and 7 show a similar alignment gain at this frequency. This alignment gain is due to breaking a pair of $\nu i_{13/2}$ quasineutrons, as typically seen in this mass region. Hence in ^{156}Er, a rotationally aligned $(\nu i_{13/2})^2$ two-quasineutron

configuration is seen coupled to three different intrinsic states, namely the 0^+ ground state, and also the $0+_2$, and 2^+_γ states.

Newly identified band 9 carries less alignment ($\sim 7.5\hbar$) than band 1 above the rotational alignment of $i_{13/2}$ neutrons ($\omega > 0.3$ MeV/$\hbar$). This could be explained if band 9 instead corresponds to a rotationally aligned $(\nu h_{9/2}, f_{7/2})^2$ configuration (the negative-parity $h_{9/2}$ and $f_{7/2}$ orbitals are strongly mixed). Indeed, such an aligned configuration has been identified in the $N = 88$ ^{162}W isotone [82], while competition between $(\nu i_{13/2})^2$ and $(\nu h_{9/2}, f_{7/2})^2$ rotational alignments has recently been observed in $N = 89$ ^{163}W [83] and $N = 88$ ^{161}Ta [84].

4.2.5 High spin behaviour of ^{156}Er

The increase in alignment of bands 1 and 2 at $\omega \sim$0.4 MeV/$\hbar$ represents the onset of a shape change from prolate to oblate in ^{156}Er, culminating in band termination at $I^\pi = 42^+$. Calculated potential energy surfaces are shown in Fig. 4.13 for $(\pi, \alpha) = (+, 0)$ states in ^{156}Er. The energy surfaces suggest that a transition to noncollective oblate states ($\gamma = 60°$) is expected above spin $\sim 30\hbar$.

Fig. 4.16 shows the energies of high-spin, positive-parity levels in ^{156}Er, including the previously unreported (46^+) state. This state appears very favoured, and it is proposed that it is the 46^+ state which is predicted to be energetically favoured in cranked Nilsson Strutinsky calculations [3]. States that are circled in Fig. 4.16 correspond to predicted oblate terminating configurations.

The $I^\pi = 42^+$ state represents the maximum spin achievable involving the 6 valence neutrons and 4 valence protons outside the ^{146}Gd core, and its full configuration, relative to the ^{146}Gd core, can be written as

$$\pi\{(h_{11/2})^4_{16}\}_{16^+} \otimes \nu\{(i_{13/2})^2_{12}(f_{7/2})^2_6(h_{9/2})^2_8\}_{26^+}. \tag{4.5}$$

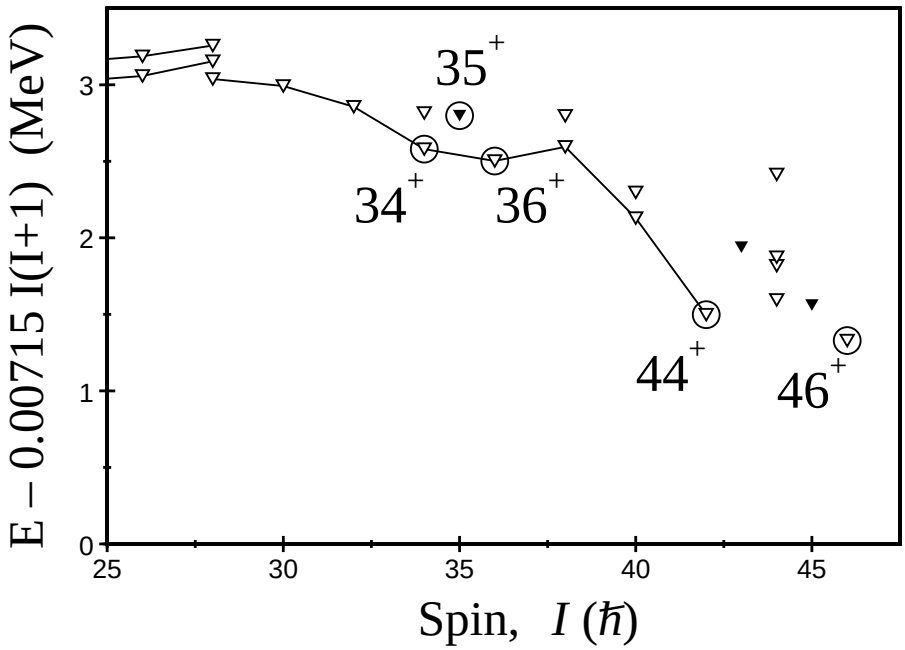

FIGURE 4.16: Energies of the high-spin positive-parity levels in ^{156}Er, plotted as a function of spin, relative to a rotating reference.

The predicted 46^+ configuration involves a proton being excited across the $Z = 64$ shell gap from the $\pi d_{5/2}/g_{7/2}$ to the $d_{3/2}$ subshell. Its configuration, relative to the ^{146}Gd core, can be written in full as

$$\pi\{(d_{5/2}/g_{7/2})^{-1}_{5/2}(h_{11/2})^{4}_{16}(d_{3/2})^{1}_{3/2}\}_{20^+} \otimes \nu\{(i_{13/2})^{2}_{12}(f_{7/2})^{2}_{6}(h_{9/2})^{2}_{8}\}_{26^+}. \qquad (4.6)$$

The tilted Fermi-surface diagrams [15] of Fig. 4.17 illustrate the specific orbitals that are occupied to form the fully aligned 42^+ and 46^+ states.

A negative-parity terminating $I = 46^-$ state is also expected, corresponding to a $\pi(d_{5/2}/g_{7/2} \rightarrow h_{11/2})$ excitation. It is predicted to be very close in energy to the 46^+ state because, at the appropriate oblate deformation, the two $m_i = 3/2$ orbitals belonging to the $h_{11/2}$ and $d_{3/2}$ subshells become near degenerate. The fifth valence proton in the $I^\pi = 20^\pm$ proton configurations lie in either of these orbitals, so the the two configurations are expected to have nearly identical energy. For this reason, it was hoped that both positive- and negative- states of ^{156}Er could be observed up

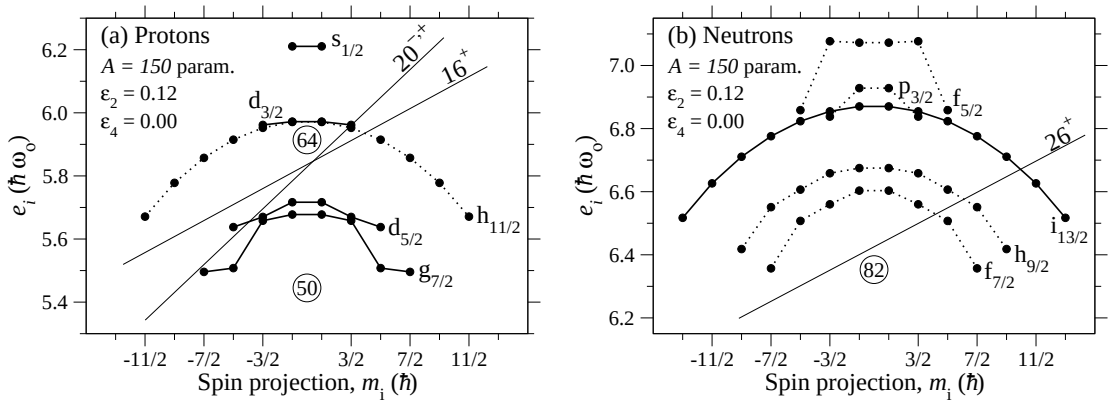

FIGURE 4.17: Tilted Fermi-surface diagrams for (a) protons and (b) neutrons at oblate shape, showing the configurations of the predicted yrast $I^\pi = 42^+$ and $I^\pi = 46^\pm$ terminating states in ^{155}Ho, built from 16^+ and $20^\pm$ proton configurations coupled to a 26^+ neutron configuration.

to $I = 46$, as it would be helpful in fixing the position of the proton subshells around $Z = 64$ in more detail [3]. Other 46^+ states built on different configurations are also predicted, but these involve two protons being excited across the $Z = 64$ shell gap and lie ~ 1 MeV higher in energy. The behaviour of ^{156}Er at band termination is discussed in the next chapter in the context of its isotones, ^{154}Dy and ^{155}Ho.

4.3 Conclusions

A high-statistics experiment with the Gammasphere spectrometer has unearthed new non-yrast structures in ^{156}Er at low spin. A band built on a low-lying second 0^+ state has been established to $I^\pi = 22^+$. This 0^+ state possibly represents a β-vibrational state [64], although, due to its low excitation energy, other modes of excitation have been considered, such as pairing isomers [71] or a second vacuum formed by particle-hole excitations [72]. In addition, both odd- and even-spin components of the γ-vibrational band have been identified, and the energy staggering between them resembles that expected for a γ-soft rotor. A band attributed to an aligned $(\nu h_{9/2}, f_{7/2})^2$ configuration has been followed to $I^\pi = (20^+)$. With this in-

terpretation, ^{156}Er is the first even-even nucleus in which competing $(\nu h_{9/2}, f_{7/2})^2$ and $(\nu i_{13/2})^2$ have been established. Finally, a further state above valence-space band termination has been established. It is proposed this state represents a predicted 46^+ terminating configuration, involving a $\pi(d_{5/2}/g_{7/2} \rightarrow d_{3/2})$ particle-hole excitation across the $Z = 64$ shell gap.

Chapter 5

^{155}Ho

5.1 Experimental Details and Results

The experiment was performed at the ATLAS facility of the Argonne National Laboratory, using the Gammasphere spectrometer described in Chapter 3. A ^{37}Cl beam at 180 MeV was used to bombard two stacked thin self-supporting foils of ^{124}Sn, of total thickness 1.1 mg/cm^2, to produce ^{155}Ho through the ^{124}Sn(^{37}Cl,6n) reaction. Events were recorded when at least five Compton-suppressed HPGe detectors fired in prompt time coincidence, and over the course of six days of beam time a total of approximately 10^{10} events was recorded. In the off-line analysis, approximately 10^{11} quadruple-coincident events (γ^4) were unfolded from the raw data and replayed into a RADWARE-format four-dimensional hypercube [48, 49] for subsequent analysis. The three most strongly populated nuclei were ^{155}Ho (6n), ^{156}Ho (5n), and ^{157}Ho (4n). In the hypercube they were measured to be populated in a ratio of approximately 0.6:1.0:0.3. Some representative coincidence spectra of transitions in ^{155}Ho seen in this work are shown in Figures 5.1–5.3.

To assist in assigning spins and parities to states in the level scheme, γ-ray multipolarities were extracted from the data by conducting an angular-correlation

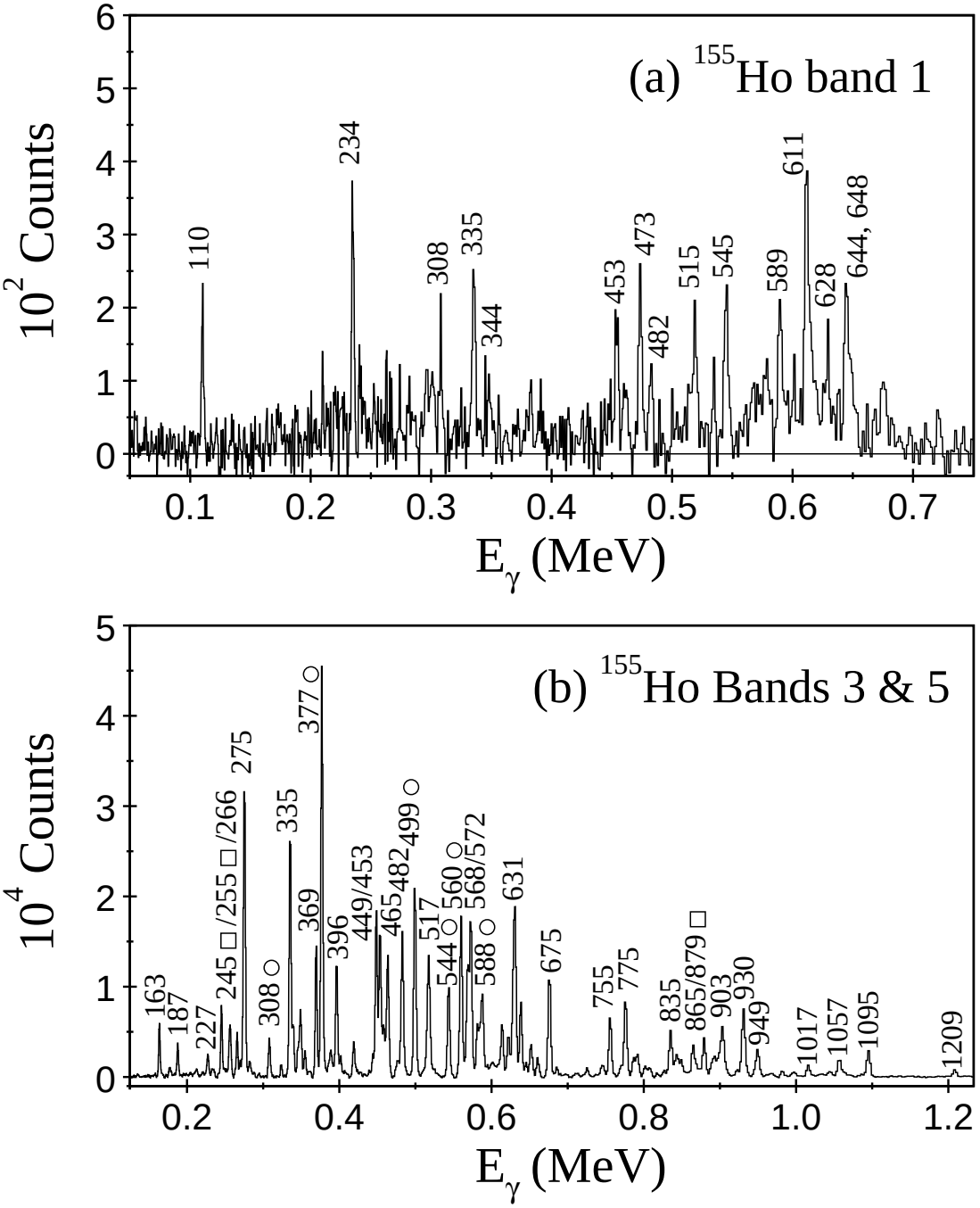

FIGURE 5.1: Triple-gated quadruple-coincidence spectra for positive-parity bands in ^{155}Ho, showing transitions in (a) band 1 and (b) bands 3 and 5. In each case, a sum of 'clean' gates was set on each axis of the hypercube. In each spectrum, the transitions are labelled by their energies in keV.

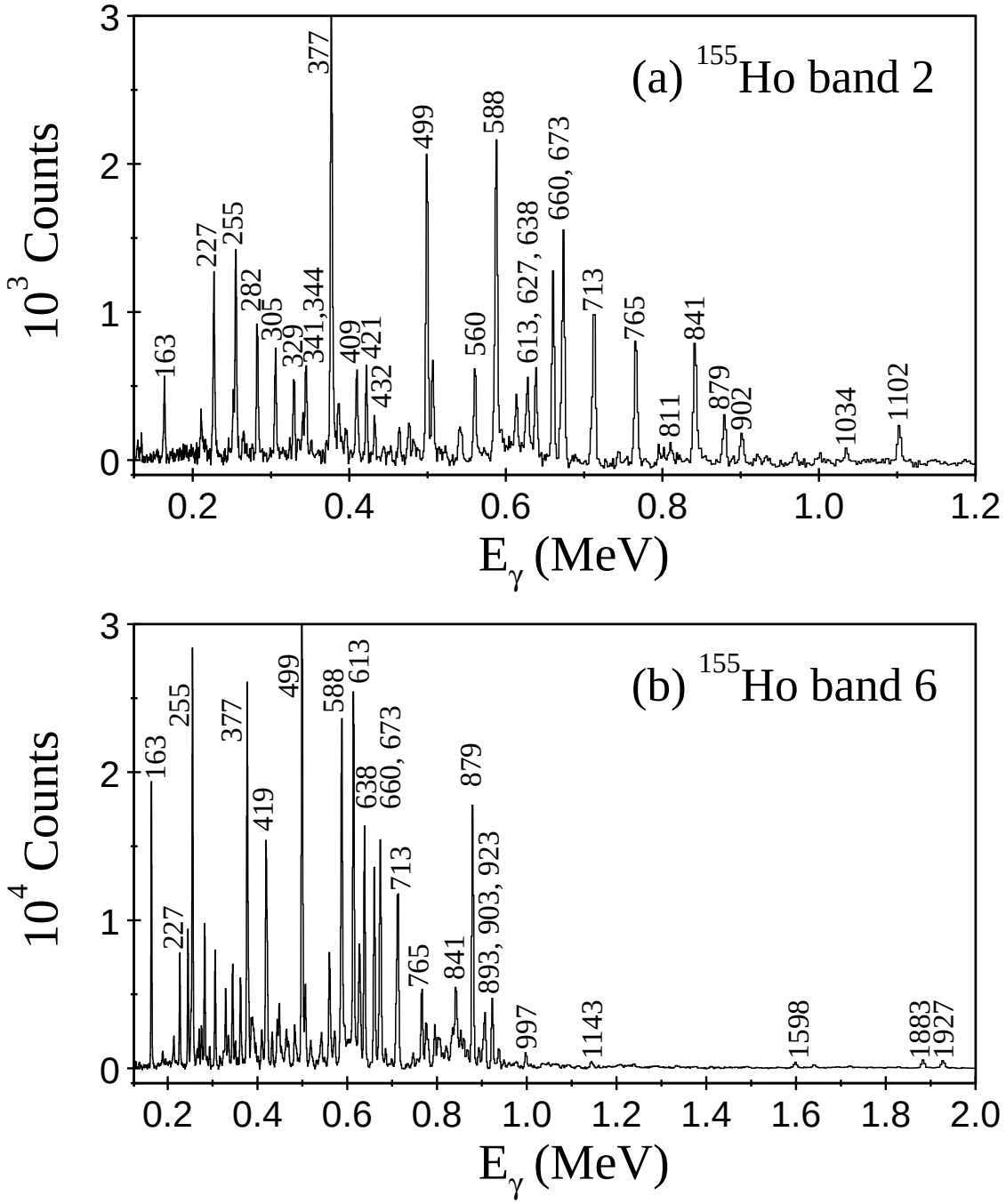

FIGURE 5.2: Triple-gated quadruple-coincidence spectra for bands in ^{155}Ho, showing transitions in (a) band 2 at high spin, and (b) bands 2 and 6. To produce spectrum (b), a gate of 906 keV was set on the first axis of the hypercube, 835 keV on the second, and a gate-list of band 2 transitions on the third. It shows the previously unreported 341, 811, 902, 1034, and 1102 keV transitions of band 2. To produce spectrum (a), a sum of 'clean' gates, consisting of band 2 and 6 transitions was set on each axis of the hypercube. In each spectrum, the transitions are labelled by their energies in keV.

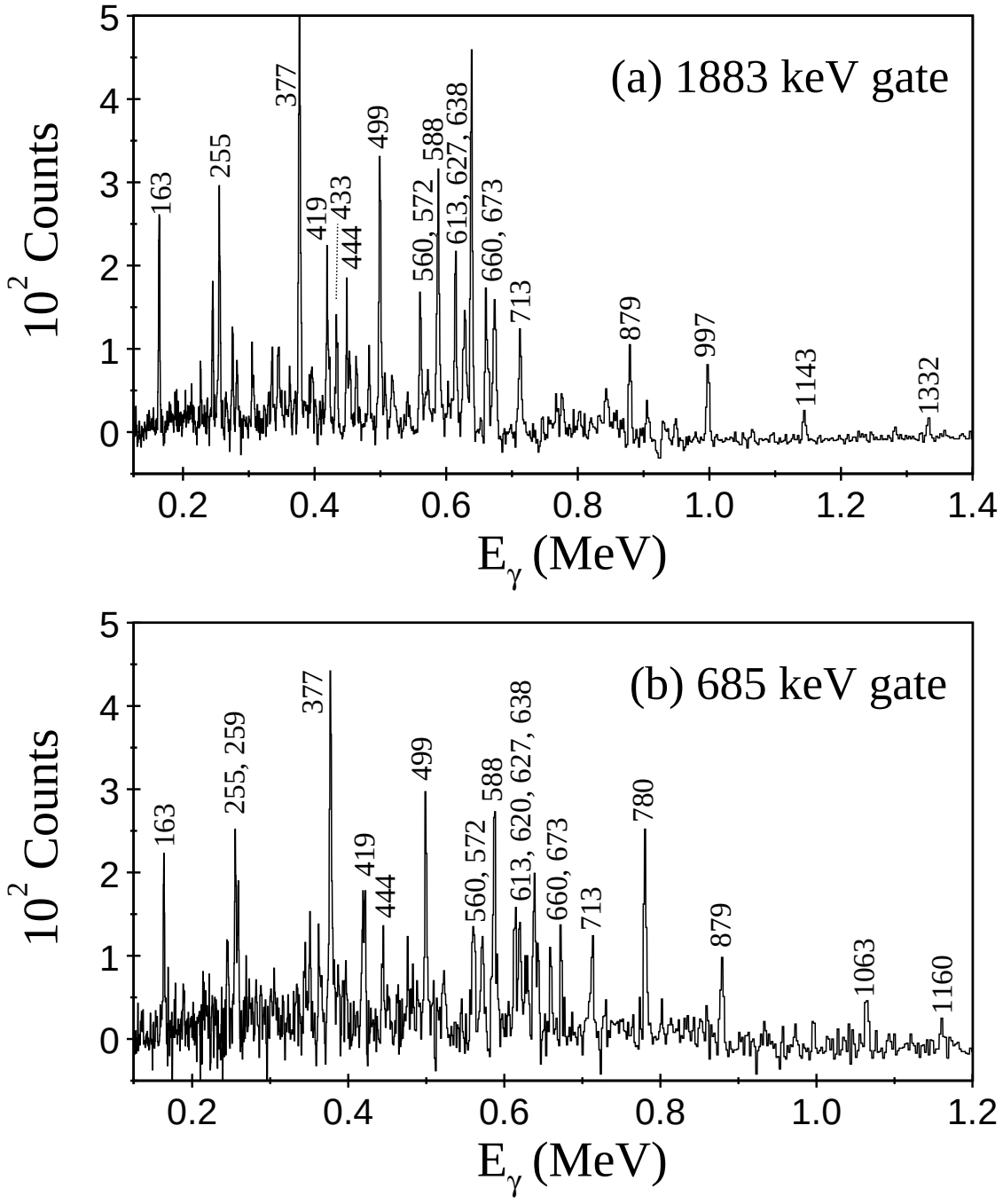

FIGURE 5.3: Triple-gated quadruple-coincidence spectra for ^{155}Ho. To produce spectrum (a) a 1883 keV gate was set on the first axis of the hypercube, and a gate-list of band 6 transitions on the second and third. It shows the 433, 997, 1143, and 1332 keV decays from the negative parity 85/2 and 87/2 levels. Spectrum (b) was generated by setting a 685 keV gate on the first axis of the hypercube, and a gate-list of band 6 transitions on the second and third. It shows the 259, 444, 620, 780, 1063, and 1160 keV transitions, which belong to 7a and 7b. In each spectrum, the transitions are labelled by their energies in keV.

analysis, using the methods described in Chapter 3. It was possible to extract the angular-intensity ratio,

$$R = \frac{I_{\gamma\gamma}[\theta \approx 150^{\circ}(30^{\circ})]}{I_{\gamma\gamma}[\theta \approx 90^{\circ}]}, \tag{5.1}$$

for over half of the reported γ-ray transitions. Typically, the angular-intensity ratios extracted from this analysis were $\sim$0.7 for a stretched dipole ($\Delta I = 1$) transition, and $\sim$1.1 for a stretched quadrupole ($\Delta I = 2$) transition.

Using the techniques detailed here and in Chapter 3, a level scheme for ^{155}Ho has been deduced (see Fig. 5.4). The band structures have been labelled 1-7 to aid discussion. At times it has not been possible to say conclusively whether or not a transition exists due to insufficient counts in the spectra or the presence of contaminants from other reaction products in the spectra. In these cases the arrow indicating the γ ray is dashed, and the energy given in parentheses. By extension, this can mean the existence of particular levels is uncertain, in which case the state is indicated by a dashed line. Insufficient counts, or insufficiently clean spectra, mean angular-correlation analysis is not possible for some transitions. For some levels, multiple possible assignments are consistent with the available data; these assignments are given in parentheses. The theoretical calculations presented in the following section have informed the assignments made for some states. This is especially the case for the levels above the $79/2^{-}$ terminating state of band 6.

All the γ-ray transitions corresponding to ^{155}Ho that have been observed in these data are listed in Table 5.1 with their intensities, which are given relative to the 377 keV transition, the strongest in ^{155}Ho. Also presented in Table 5.1 are the measured angular-intensity ratios of the transitions, their corresponding multipolarities, the spin-parity assignments for initial and final states, and the bands to which the transitions belong.

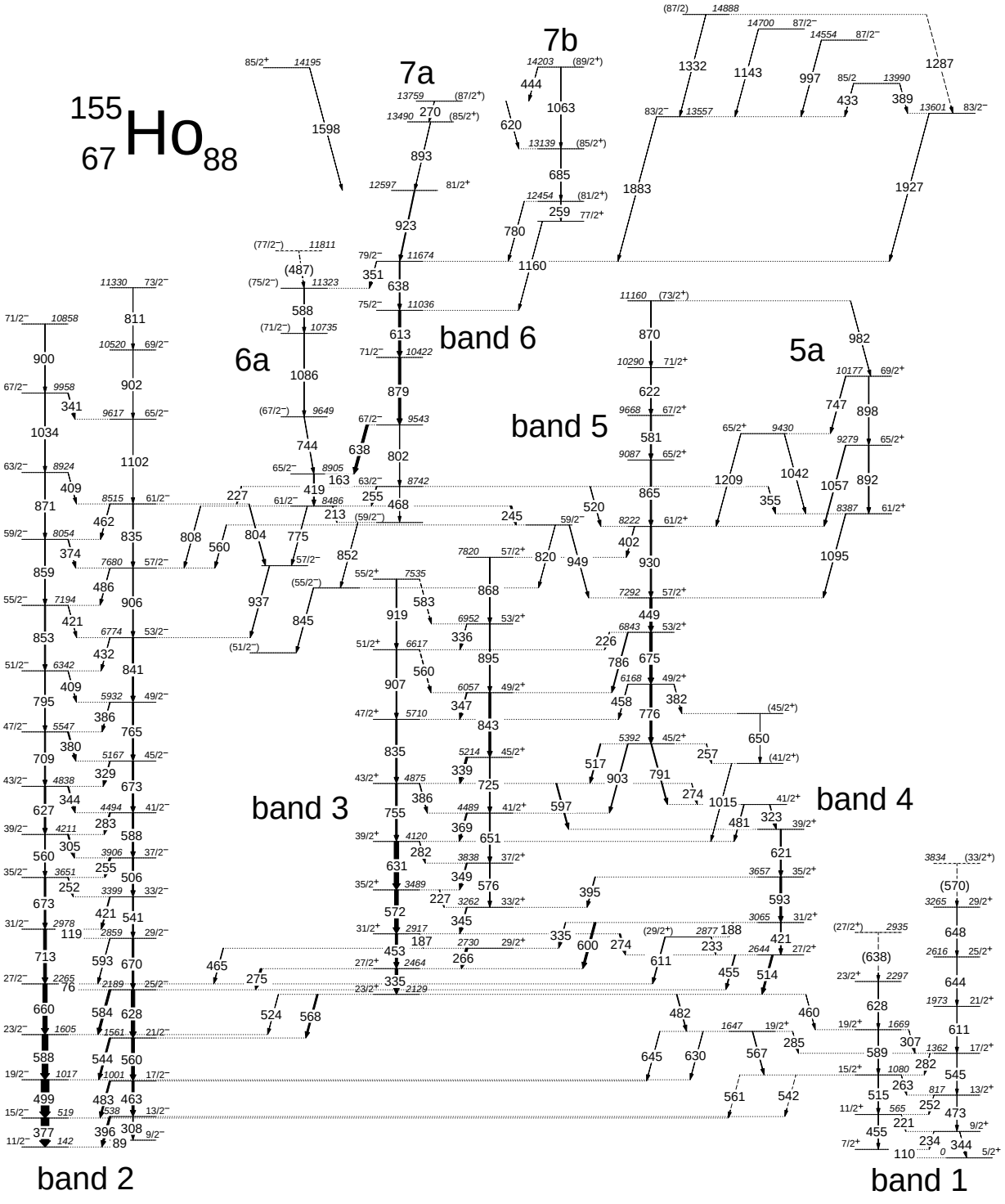

FIGURE 5.4: Level scheme deduced for ^{155}Ho from the present work showing all observed transitions. Energies are labelled in keV and the widths of the arrows are proportional to the transition intensities. Parenthesis indicate tentative assignments.

5.1.1 New states in ^{155}Ho, bands 1-5

For the coupled rotational bands, 1, 2 and 3, values for the branching ratio, $\lambda = I_\gamma(\Delta I = 1)/I_\gamma(\Delta I = 2)$, have been measured for many of the levels. This was achieved by applying double- or triple-gates above the level of interest, producing γ-ray spectra showing the competing dipole and quadrupole transitions depopulating the level. The branching ratios are presented in Table 5.2. $B(M1)/B(E2)$ ratios of reduced transition probabilities have been determined using the branching ratio measurements, and will be examined in more detail in the discussion section of this chapter.

Band 1

In the positive-parity band 1, which decays to the $I^\pi = 5/2^+$ ground state, both the $7/2^+$ and $9/2^+$ levels at 110 and 344 keV have been previously reported [85]. With the exception of the placement of a 473 keV transition, their ordering is corroborated by this work, and the band is now established up to spins of $(33/2^+)$, or $29/2^+$ excluding tentative transitions. The 472.5 keV transition reported by Foin *et al.* [86] was thought to feed the $7/2^+$ state, suggesting the existence of a $(11/2^+)$ state at 503 keV, linked to the $9/2^+$ level via a 238 keV transition. The energy is consistent with that of an observed 472.8 keV transition in this work. However, no 238 keV transition has been found associated with this structure, and coincidence relations show that the 473 keV transition feeds the $9/2^+$ state. Its angular-intensity ratio is typical of a stretched $E2$. The other γ rays observed in band 1 are previously unreported; the angular-intensity ratios it has been practicable to measure and the coincidence relations are consistent with the interlinking signature partners of a rotational band which decays to the $5/2^+$ ground state. The levels in band 1 are less favoured in energy than those in band 2 of similar spin, and are weakly populated by comparison.

Previous decay studies of ^{155}Er have shown a 31.8 keV $M2$ transition in ^{155}Ho linking the $11/2^-$ band-head of band 2 with the $7/2^+$ state of band 1 [85]. While it is not possible to see this transition in the current experiment, new transitions linking band 1 with band 3, and by extension the rest of the level scheme, show that the separation in energy between the $11/2^-$ and $7/2^+$ states is 31.9 keV. This consistency is further evidence that the proposed extensions to band 1 and the positions of the transitions linking band 1 to the previously known level scheme are correct. Fig. 5.1(a) is a sum of carefully chosen, 'clean' triple-gated spectra, using transitions in band 1 as gates.

Band 2

At low spin, band 2 is the most strongly populated of the structures evident in ^{155}Ho. Because it is relatively easy to populate compared to other structures examined here, the majority of the levels of band 2 are well documented. As such, much of what is presented here on band 2 is a confirmation of previous work. The band has, however, been extended to higher spins, and levels up to $I^\pi = 71/2^-, 73/2^-$ have been observed.

Band 2 is a rotational band consisting of both $\alpha = -1/2$ and $\alpha = +1/2$ signature components, though below $\sim 17\hbar$ the $\alpha = -1/2$ components lie significantly lower in energy. Due to this large staggering between the signature components, some of the interlinking $M1/E2$ transitions were too low in energy to observe. The multipolarities of many of the transitions have been confirmed, along with the coincidence relations and subsequent ordering of the transitions. Interlinking transitions between the signature components mean the transitions up to the highest spins are ordered with certitude. Decays are observed from bands 1, 3 and 4 to levels in band 2 below spin 29/2, and band 6 decays, in a rather fragmented manner, to $\alpha = +1/2$ levels in band 2 between spins 53/2 and 61/2.

Many of the band 2 transitions can be seen in the spectrum of Fig. 5.2(a), which is triple-gated using a list of transitions in bands 2 and 6. Fig. 5.2(b) is also a triple-gated spectrum, using transitions between the $\alpha = +1/2$ levels of band 2 as gates. The spectrum was produced by setting a 835 keV gate on the first axis of the hypercube, a 906 keV gate on the second, and a gate-list consisting of band 2 energies on the third. This spectrum shows the previously unreported 1102, 902, and 811 keV transitions between $\alpha = +1/2$ levels in band 2, as well as the 1034 keV transition in the $\alpha = -1/2$ signature band.

Band 3

The structure labelled band 3 decays to band 1 via four γ rays, three of which have angular-intensity ratios typical of $I \rightarrow I - 1$ dipole transitions. The absence of any quadrupole linking transitions suggests that those observed are electric dipole ($E1$) in character, and that this structure has positive parity. That it decays to the positive-parity band 1 via quadrupole transitions confirms its positive-parity assignment. Band 3 is observed between $23/2^+$ and $57/2^+$ and is yrast between $31/2^+$ and $39/2^+$. It is fed by decays from band 5 and to a lesser extent, at its lowest levels, band 4. The present analysis has confirmed previous assignments in band 3, and also extended it to higher spin.

Band 4

A short cascade of $E2$ transitions is observed between spins $39/2^+$ and $27/2^+$, and has been labelled band 4. Fed by decays from bands 3 and 5, it also decays to band 3, as well as band 2. The band has signature $\alpha = -1/2$, though a level tentatively assigned spin-parity $(29/2^+)$ at 2877 keV may belong to the signature partner of band 4.

Band 5

A further positive-parity structure, band 5, that is briefly yrast at spins $57/2^+$ and $61/2^+$ is also observed, and mainly decays to levels in band 3. The decays to the positive-parity band 3 include stretched $E2$ transitions (the 786 keV and 903 keV γ rays have angular-intensity ratios of 1.08(15) and 1.22(13), respectively), which indicates that band 5 also has positive-parity. The angular-intensity ratios measured for these linking transitions, as well as for transitions in band 5 itself, have made it possible to confidently assign spin-parity values to levels in band 5 up to $71/2^+$. While it has not been possible to make a measurement for the 870 keV transition that feeds this $71/2^+$ state, the level at 11160 keV can be labelled as $(73/2^+)$ through selection rules, since it also appears to decay to a $69/2^+$ state, though this does not completely rule out a lower spin assignment. There are two further structures loosely associated with band 5: one consists of two levels assigned as $(41/2^+)$ and $(45/2^+)$, and decays into band 3 via a 1015 keV transition, and the other has levels of spin $61/2^+$, $65/2^+$, and $69/2^+$. Band 6 decays to band 5 via two γ rays, of energy 520 keV and 949 keV, which have angular-intensity ratios typical of stretched dipoles.

5.1.2 New levels at high spin: bands 6, 7, and above

Levels in band 6 have been seen previously [87], though not linked to the rest of the level scheme. By extracting angular-correlation information for the more strongly populated transitions in the band, it has been possible to assign spin values with confidence up to the $79/2^-$ level. The presence of a 638 keV doublet in band 6 made it necessary to take care when selecting coincidence gates for the angular-correlation measurements. It was possible to extract an angular-intensity ratio of 1.10(7) for the higher-spin 638 keV transition, demonstrating that it is most likely a stretched $E2$. The measured ratio for the more intense $67/2^- \rightarrow 65/2^-$ 638 keV transition

was 0.51(3). In Fig. 3.8 of Chapter 3 the angular-distribution function 3.3 has been fitted for both 638 keV transitions.

Notable are the two high-energy (1883 keV and 1927 keV) transitions that feed the $79/2^-$ level. With angular-intensity ratios typical of stretched $E2$ transitions, (1.23(9) and 1.12(8), respectively) these indicate the presence of two high lying $83/2^-$ states. The $83/2^-$ state at 13.557 MeV is in turn fed by four γ rays. angular-correlation analysis shows that the 433 keV transition is a dipole, whereas the 997 keV and 1143 keV transitions are stretched $E2$ transitions. Thus, the highest-spin negative-parity levels reported in this work have spin 87/2, and lie at 14.554 MeV and 14.700 MeV above the ground state. The 433 keV transition indicates the presence of an $I = 85/2$ state, confirmed by the observation of a 389 keV dipole transition decaying to the other $83/2^-$ state. The 1332 keV transition proved to be too weakly populated to reliably extract angular-correlation information, and as such the level at 14.888 MeV is labelled $(87/2^-)$.

A cascade of γ rays, labelled 6a, decays parallel to band 6. It has not been possible to ascertain the spins of levels in 6a with confidence, and there is some doubt over the ordering of the 744 and 1086 keV transitions. The angular-intensity ratio measured for the 744 keV transition is indicative of a dipole, so the band is assumed to be a cascade of $E2$ transitions, which decays to band 6 via this 744 keV transition.

There are two further structures, labelled 7a and 7b, which lie higher in energy than the $79/2^-$ state. The structure labelled 7a consists of a 270 keV and 893 keV transition, and 7b consists of a cascade of three γ rays of energy 259, 685, and 1063 keV. The two are linked by two γ rays of energies 444 keV and 620 keV. Due to them being relatively weakly populated, it has not been possible to extract angular-intensity ratios for enough transitions to firmly establish the spin and parity of all the 'band' 7 levels up to the highest spins. The proposed, tentative, assignments

are consistent with these data, and are informed by the theoretical calculations presented in the next section. It is suggested the two structures terminate at two states of spin and parity $(87/2^+)$ and $(89/2^+)$. The angular-intensity ratios that have been measured are consistent with a change in parity in the decay from 7a and 7b to band 6; both the 923 keV and 1160 keV transitions have ratios typical of a stretched-$E1$ ($I \rightarrow I-1$) transition of 0.75(9) and 0.72(9), respectively.

Unplaced γ rays

Some transitions have been observed in coincidence with structures in ^{155}Ho, and have been included in Table 5.1, but it has not been possible to confidently place them in the level scheme. These include a 362 keV γ ray, which appears in coincidence with many transitions in bands 2 and 6, and may represent a linking transition between the two. There is also an 822 keV γ ray that appears in strong coincidence with band 2; it is also seen in coincidence with an unplaced 745 keV transition, thought to be be distinct from the 744 keV transition of band 6.

TABLE 5.1: Energies, intensities, angular-intensity ratios, and spin-parity assignments for the observed ^{155}Ho transitions. The band labels used in the final column correspond to those in Fig. 5.4.

E_γ (keV)[a]	I_γ[b]	R[c]	Multipolarity	Assignment			Band[d]
88.6	1.8			$9/2^-$	$\rightarrow$	$11/2^-$	2
110.1	9.9	0.53(7)	M1/E2	$7/2^+$	$\rightarrow$	$5/2^+$	1
119.0	3.20			$31/2^-$	$\rightarrow$	$29/2^-$	2
163.4	13.8	0.577(25)	M1/E2	$65/2^-$	$\rightarrow$	$63/2^-$	6
187.4	11.6	0.64(5)	M1/E2	$31/2^+$	$\rightarrow$	$29/2^+$	3
187.9	1.18			$31/2^+$	$\rightarrow$	$(29/2^+)$	4
213.0	2.2	0.66 (22)	M1/E2	$61/2^-$	$\rightarrow$	$59/2^-$	6
220.7				$11/2^+$	$\rightarrow$	$9/2^+$	1
226.3	2.47			$53/2^+$	$\rightarrow$	$51/2^+$	$5 \rightarrow 3$
226.6	5.61	0.540(21)	M1/E2	$63/2^-$	$\rightarrow$	$61/2^-$	$6 \rightarrow 2$
227.0	5.3	0.61(5)	M1/E2	$35/2^+$	$\rightarrow$	$33/2^+$	3
233.0	2.7			$(29/2^+)$	$\rightarrow$	$27/2^+$	4
234.0	2.4	0.82(9)	M1/E2	$9/2^+$	$\rightarrow$	$7/2^+$	1
244.8	18.1	0.68(4)	M1/E2	$61/2^-$	$\rightarrow$	$59/2^-$	6
251.7	8.6	0.58(3)	M1/E2	$35/2^-$	$\rightarrow$	$33/2^-$	2
252.1	1.1	0.94(11)	M1/E2	$13/2^+$	$\rightarrow$	$11/2^+$	1
254.7	20.0	0.585(16)	M1/E2	$37/2^-$	$\rightarrow$	$35/2^-$	2
255.4	7.4	0.686(19)	M1/E2	$63/2^-$	$\rightarrow$	$61/2^-$	6
256.5	6.1			$45/2^+$	$\rightarrow$	$(41/2^+)$	(5)
258.7				$(81/2^+)$	$\rightarrow$	$(77/2^+)$	$7b$
263.1	1.5			$15/2^+$	$\rightarrow$	$13/2^+$	1
265.5	25.4	0.62(22)	M1/E2	$29/2^+$	$\rightarrow$	$27/2^+$	3
269.6	2.0	0.91(23)	(M1/E2)	$(87/2^+)$	$\rightarrow$	$(85/2^+)$	$7a$
273.6	16.5			$31/2^+$	$\rightarrow$	$27/2^+$	$3 \rightarrow 4$
274.1	3.1			$43/2^+$	$\rightarrow$	$41/2^+$	$3 \rightarrow 4$
275.3	24.9	0.72(5)	E1	$27/2^+$	$\rightarrow$	$25/2^-$	$3 \rightarrow 2$
281.5				$17/2^+$	$\rightarrow$	$15/2^+$	1
281.9	5.3	0.79(9)	M1/E2	$39/2^+$	$\rightarrow$	$37/2^+$	3
282.6	12.9	0.63(3)	M1/E2	$41/2^-$	$\rightarrow$	$39/2^-$	2
285.3	1.5			$19/2^+$	$\rightarrow$	$17/2^+$	$3 \rightarrow 1$
293.2							
305.3	13.6	0.70(4)	M1/E2	$39/2^-$	$\rightarrow$	$37/2^-$	2
307.3	1.5			$19/2^+$	$\rightarrow$	$17/2^+$	1
307.6	8.8	1.00(8)	E2	$13/2^-$	$\rightarrow$	$9/2^-$	2
323.4	6.9	0.55(9)	M1/E2	$41/2^+$	$\rightarrow$	$39/2^+$	4
329.4	9.1	0.57(6)	M1/E2	$45/2^-$	$\rightarrow$	$43/2^-$	$2 \rightarrow 2$
334.8	6.0	0.78(10)	M1/E2	$31/2^+$	$\rightarrow$	$29/2^+$	$4 \rightarrow 3$
335.0	33.2	1.12(9)	E2	$27/2^+$	$\rightarrow$	$23/2^+$	3

TABLE 5.1 CONTINUED.

E_γ (keV)[a]	I_γ[b]	R[c]	Multipolarity	Assignment			Band[d]
335.6	2.7			$53/2^+$	$\rightarrow$	$51/2^+$	3
339.0	22.7	0.70(9)	M1/E2	$45/2^+$	$\rightarrow$	$43/2^+$	3
340.6	8.3			$67/2^-$	$\rightarrow$	$65/2^-$	2
344.1	12.2	0.66(3)	M1/E2	$43/2^-$	$\rightarrow$	$41/2^-$	2
344.1	1.2			$9/2^+$	$\rightarrow$	$5/2^+$	1
345.2	10.7	0.66(4)	M1/E2	$33/2^+$	$\rightarrow$	$31/2^+$	3
347.4	9.4	0.71(9)	M1/E2	$49/2^+$	$\rightarrow$	$47/2^+$	3
348.8	13.2	0.668(23)	M1/E2	$37/2^+$	$\rightarrow$	$35/2^+$	3
350.7	4.60			$79/2^-$	$\rightarrow$	$(75/2^-)$	6
354.9	3.28	0.57(10)	E1	$63/2^-$	$\rightarrow$	$61/2^+$	$6 \rightarrow 5$
362.0	≈ 1						
369.0	14.3	0.622(22)	M1/E2	$41/2^+$	$\rightarrow$	$39/2^+$	3
374.2	7.7			$59/2^-$	$\rightarrow$	$57/2^-$	2
376.7	100	0.983(21)	E2	$15/2^-$	$\rightarrow$	$11/2^-$	2
379.5	14.1			$47/2^-$	$\rightarrow$	$45/2^-$	2
381.6	4.7	0.73(9)	E2	$49/2^+$	$\rightarrow$	$(45/2^+)$	(5)
385.8	6.5			$49/2^-$	$\rightarrow$	$47/2^-$	2
386.3	7.1	0.75(11)	M1/E2	$43/2^+$	$\rightarrow$	$41/2^+$	3
388.7	0.7	0.70(10)	M1/E2	85/2	$\rightarrow$	$83/2^-$	c
395.0	8.3	1.04(9)	M1/E2	$35/2^+$	$\rightarrow$	$33/2^+$	$4 \rightarrow 3$
396.2	23	0.91(3)	M1/E2	$13/2^-$	$\rightarrow$	$11/2^-$	2
401.9	6.3	1.14(5)	E2	$61/2^+$	$\rightarrow$	$57/2^+$	$5 \rightarrow 3$
408.9	2.7	0.76(6)	M1/E2	$63/2^-$	$\rightarrow$	$61/2^-$	2
409.0	4.7			$51/2^-$	$\rightarrow$	$49/2^-$	2
418.8	12.3	1.04(17)	E2	$65/2^-$	$\rightarrow$	$61/2^-$	6
420.5	3.7			$55/2^-$	$\rightarrow$	$53/2^-$	2
420.9	10.9	1.1(3)	E2	$31/2^+$	$\rightarrow$	$27/2^+$	4
421.5	10.3			$33/2^-$	$\rightarrow$	$31/2^-$	2
432.2	4.8	0.69(16)	M1/E2	$53/2^-$	$\rightarrow$	$51/2^-$	2
432.8	0.7	0.80(9)	M1/E2	85/2	$\rightarrow$	$83/2^-$	c
443.7	1.2	0.84(5)	(M1/E2)	$(89/2^+)$	$\rightarrow$	$(87/2^+)$	$7b \rightarrow 7a$
448.7	28.4	1.17(3)	E2	$57/2^+$	$\rightarrow$	$53/2^+$	5
453.0	29.2	0.932(9)	E2	$31/2^+$	$\rightarrow$	$27/2^+$	3
454.5	10.6			$27/2^+$	$\rightarrow$	$25/2^-$	$4 \rightarrow 2$
454.7	1.8	1.01(15)	E2	$11/2^+$	$\rightarrow$	$7/2^+$	1
457.9	6.5			$49/2^+$	$\rightarrow$	$47/2^+$	$5 \rightarrow 3$
459.8	4.5	0.94(8)	E2	$23/2^+$	$\rightarrow$	$19/2^+$	$3 \rightarrow 1$
461.7	6.6			$61/2^-$	$\rightarrow$	$59/2^-$	2
463.3	29.3	0.970(11)	E2	$17/2^-$	$\rightarrow$	$13/2^-$	2
464.5	6.9	0.51(10)	E1	$29/2^+$	$\rightarrow$	$27/2^-$	$3 \rightarrow 2$
468.2				$63/2^+$	$\rightarrow$	$59/2^-$	6

TABLE 5.1 CONTINUED.

E_γ (keV)[a]	I_γ[b]	R[c]	Multipolarity	Assignment			Band[d]
472.8	3.0	1.02(9)	E2	$13/2^+$	$\rightarrow$	$9/2^+$	1
481.0	7.2			$41/2^+$	$\rightarrow$	$39/2^+$	$4 \rightarrow 3$
482.4	8.9	1.10(5)	E2	$23/2^+$	$\rightarrow$	$19/2^+$	3
482.8	19.5			$17/2^-$	$\rightarrow$	$15/2^-$	2
485.6	5.9			$57/2^-$	$\rightarrow$	$55/2^-$	2
487.0				$(77/2^-)$	$\rightarrow$	$(75/2^-)$	$6a$
495.5	8.0			$47/2^+$	$\rightarrow$	$45/2^+$	3
498.6	100	1.02(3)	E2	$19/2^-$	$\rightarrow$	$15/2^-$	2
506.2	18.0	1.17(7)	E2	$37/2^-$	$\rightarrow$	$33/2^-$	2
514.5	21.6			$27/2^+$	$\rightarrow$	$23/2^+$	$4 \rightarrow 3$
515.2	6.0	0.82(17)	E2	$15/2^+$	$\rightarrow$	$11/2^+$	1
516.7	11.1	0.83(19)	M1/E2	$45/2^+$	$\rightarrow$	$43/2^+$	$5 \rightarrow 3$
519.8	5.8	0.59(12)	E1	$63/2^-$	$\rightarrow$	$61/2^+$	$6 \rightarrow 5$
524.1	3.5			$23/2^+$	$\rightarrow$	$23/2^-$	$3 \rightarrow 2$
540.9	14.5			$33/2^-$	$\rightarrow$	$29/2^-$	2
541.7	1.2			$15/2^+$	$\rightarrow$	$13/2^-$	$1 \rightarrow 2$
543.8	20.6			$21/2^-$	$\rightarrow$	$19/2^-$	2
544.6	1.0	1.11(9)	E2	$17/2^+$	$\rightarrow$	$13/2^+$	1
559.6	6.7			$51/2^+$	$\rightarrow$	$49/2^+$	3
559.6	37.7	1.16(5)	E2	$21/2^-$	$\rightarrow$	$17/2^-$	2
559.8	4.9			$59/2^-$	$\rightarrow$	$57/2^-$	$6 \rightarrow 2$
559.9	12.3			$39/2^-$	$\rightarrow$	$35/2^-$	2
561.2	1.2			$15/2^+$	$\rightarrow$	$15/2^-$	$1 \rightarrow 2$
566.9	12.4			$19/2^+$	$\rightarrow$	$15/2^+$	$3 \rightarrow 1$
568.1	20.4	0.618(17)	E1	$23/2^+$	$\rightarrow$	$21/2^-$	$3 \rightarrow 2$
569.6				$(33/2^+)$	$\rightarrow$	$29/2^+$	1
572.3	48.2	1.09(6)	E2	$35/2^+$	$\rightarrow$	$31/2^+$	3
575.8	9.5			$37/2^+$	$\rightarrow$	$33/2^+$	3
581.1	22.7	0.67(4)	M1/E2	$67/2^+$	$\rightarrow$	$65/2^+$	5
583.0	23.3			$55/2^+$	$\rightarrow$	$53/2^+$	3
584.2	26.6	0.72(14)	M1/E2	$25/2^-$	$\rightarrow$	$23/2^-$	2
587.9	76	1.26(3)	E2	$23/2^-$	$\rightarrow$	$19/2^-$	2
587.9	19.6	1.13(3)	E2	$41/2^-$	$\rightarrow$	$37/2^-$	2
588.0	3.0			$(75/2^-)$	$\rightarrow$	$(71/2^-)$	6
589.4	4.5			$19/2^+$	$\rightarrow$	$15/2^+$	1
592.9	23.8			$35/2^+$	$\rightarrow$	$31/2^+$	4
593.3	6.0			$29/2^-$	$\rightarrow$	$27/2^-$	2
596.9	13.7			$43/2^+$	$\rightarrow$	$39/2^+$	$3 \rightarrow 4$
600.3	26.2			$31/2^+$	$\rightarrow$	$27/2^+$	$4 \rightarrow 3$
611.1	3.6	1.23(6)	E2	$21/2^+$	$\rightarrow$	$17/2^+$	1
611.5	9.0			$(29/2)^+$	$\rightarrow$	$27/2^-$	$4 \rightarrow 2$

Table 5.1 continued.

E_γ (keV)[a]	I_γ[b]	R[c]	Multipolarity	Assignment			Band[d]
613.5	33.6	1.25(7)	E2	$75/2^-$	$\rightarrow$	$71/2^-$	6
620.0				$(87/2^+)$	$\rightarrow$	$(85/2^+)$	$7a \rightarrow 7b$
620.9	15.6			$39/2^+$	$\rightarrow$	$35/2^+$	4
622.4	12.3	1.53(13)	E2	$71/2^+$	$\rightarrow$	$67/2^+$	5
626.7	21.0	1.19(6)	E2	$43/2^-$	$\rightarrow$	$39/2^-$	2
627.7	6.0	1.19(6)	E2	$23/2^+$	$\rightarrow$	$19/2^+$	1
628.1	46.0	1.2(7)	E2	$25/2^-$	$\rightarrow$	$21/2^-$	2
629.5	4.5			$19/2^+$	$\rightarrow$	$19/2^-$	$3 \rightarrow 2$
630.6	58.6	1.20(5)	E2	$39/2^+$	$\rightarrow$	$35/2^+$	3
638.1	32.0	0.51(3)	M1/E2	$67/2^-$	$\rightarrow$	$65/2^-$	6
638.3	18.0	1.10(7)	E2	$79/2^-$	$\rightarrow$	$75/2^-$	6
638.4	9.1			$(27/2^+)$	$\rightarrow$	$23/2^+$	1
643.8	1.5			$25/2^+$	$\rightarrow$	$21/2^+$	1
645.3	4.1			$19/2^+$	$\rightarrow$	$17/2^-$	$3 \rightarrow 2$
648.1				$29/2^+$	$\rightarrow$	$25/2^+$	1
650.0				$(45/2^+)$	$\rightarrow$	$(41/2^+)$	(5)
650.9	13.5	1.60(23)	E2	$41/2^+$	$\rightarrow$	$37/2^+$	3
660.1	55.9	1.15(4)	E2	$27/2^-$	$\rightarrow$	$23/2^-$	2
669.7	23.5			$29/2^-$	$\rightarrow$	$25/2^-$	2
673.2	21.8	1.21(3)	E2	$35/2^-$	$\rightarrow$	$31/2^-$	2
673.4	19.9			$45/2^-$	$\rightarrow$	$41/2^-$	2
675.4	34.7	1.13(8)	E2	$53/2^+$	$\rightarrow$	$49/2^+$	5
684.8	2.2	1.17(11)	E2	$(85/2^+)$	$\rightarrow$	$(81/2^+)$	$7b$
708.9	15.4	0.98(11)	E2	$47/2^-$	$\rightarrow$	$43/2^-$	2
712.5	38.2	1.14(4)	E2	$31/2^-$	$\rightarrow$	$27/2^-$	2
725.3	13.0	1.07(5)	E2	$45/2^+$	$\rightarrow$	$41/2^+$	3
743.7	6.0	0.70(10)	(M1/E2)	$(67/2^-)$	$\rightarrow$	$65/2^-$	$6a \rightarrow 6$
744.5	≈ 2						
746.8	6.9	1.08 (15)	E2	$69/2^+$	$\rightarrow$	$65/2^+$	$5a$
755.3	22.3	1.23(19)	E2	$43/2^+$	$\rightarrow$	$39/2^+$	3
765.3	17.2	1.12(5)	E2	$49/2^-$	$\rightarrow$	$45/2^-$	2
775.2	5.7	1.18(18)	E2	$61/2^-$	$\rightarrow$	$57/2^-$	$6 \rightarrow (2)$
776.1	26.2	0.99(7)	E2	$49/2^+$	$\rightarrow$	$45/2^+$	5
779.7	3.0			$(81/2^+)$	$\rightarrow$	$79/2^-$	$7b \rightarrow 6$
785.9	10.6	1.07(15)	E2	$53/2^+$	$\rightarrow$	$49/2^+$	$5 \rightarrow 3$
791.2	12.4	1.15(16)	E2	$45/2^+$	$\rightarrow$	$41/2^+$	$5 \rightarrow 4$
794.9	12.2	0.91(9)	E2	$51/2^-$	$\rightarrow$	$47/2^-$	2
801.8	5.4	1.07(16)	E2	$67/2^-$	$\rightarrow$	$63/2^-$	6
804.3	8.2			$61/2^-$	$\rightarrow$	$57/2^-$	$2 \rightarrow (2)$
807.6	4.5			$61/2^-$	$\rightarrow$	$57/2^-$	$6 \rightarrow 2$

TABLE 5.1 CONTINUED.

E_γ (keV)[a]	I_γ[b]	R[c]	Multipolarity	Assignment			Band[d]
810.8	5.3			$(73/2^-)$	$\rightarrow$	$69/2^-$	2
820.0	3			$59/2^-$	$\rightarrow$	$(55/2^-)$	(6)
822.3	≈ 2						
834.7	20.0	0.95(5)	E2	$47/2^+$	$\rightarrow$	$43/2^+$	3
835.2	10.0	1.04(26)	E2	$61/2^-$	$\rightarrow$	$57/2^-$	2
841.3	18.1	0.92(4)	E2	$53/2^-$	$\rightarrow$	$49/2^-$	2
842.8	26.1	0.93(17)	E2	$49/2^+$	$\rightarrow$	$45/2^+$	3
845.0	3			$(55/2^-)$	$\rightarrow$	$(51/2^-)$	$(6) \rightarrow (2)$
851.5	0.5			$59/2^-$	$\rightarrow$	$(55/2^-)$	$6 \rightarrow (6)$
852.7	16.0	1.10(11)	E2	$55/2^-$	$\rightarrow$	$51/2^-$	2
859.2	11.1	1.03(15)	E2	$59/2^-$	$\rightarrow$	$55/2^-$	2
864.9	18.0	1.18(11)	E2	$65/2^+$	$\rightarrow$	$61/2^+$	5
867.7	11.3	0.99(22)	E2	$57/2^+$	$\rightarrow$	$53/2^+$	3
869.7	6.5			$(73/2^+)$	$\rightarrow$	$71/2^+$	5
870.7	7.0			$63/2^-$	$\rightarrow$	$59/2^-$	2
879.1	31.3	1.18(10)	E2	$71/2^-$	$\rightarrow$	$67/2^-$	6
892.5	10.8	1.03(23)	E2	$65/2^+$	$\rightarrow$	$61/2^+$	5
892.7	6.2	1.02(5)	E2	$(85/2^+)$	$\rightarrow$	$81/2^+$	$7a$
895.1	12.9	1.11(18)	E2	$53/2^+$	$\rightarrow$	$49/2^+$	3
898.4	7.8	0.88(10)	E2	$69/2^+$	$\rightarrow$	$65/2^+$	$5a$
900.1	4.3			$(71/2^-)$	$\rightarrow$	$67/2^-$	2
902.1	3.7	1.19(12)	E2	$69/2^-$	$\rightarrow$	$65/2^-$	2
902.9	9.8	1.22(13)	E2	$45/2^+$	$\rightarrow$	$41/2^+$	$5 \rightarrow 3$
906.5	10.1	1.10(8)	E2	$57/2^-$	$\rightarrow$	$53/2^-$	2
906.9	12.1	0.95(17)	E2	$51/2^+$	$\rightarrow$	$47/2^+$	3
918.5	11.6	1.5(4)	E2	$55/2^+$	$\rightarrow$	$51/2^+$	3
922.9	7.2	0.75(9)	E1	$81/2^+$	$\rightarrow$	$79/2^-$	$7a \rightarrow 6$
930.1	18.5	1.13(8)	E2	$61/2^+$	$\rightarrow$	$57/2^+$	5
937.1	6.5	1.44(24)	E2	$57/2^-$	$\rightarrow$	$53/2^-$	$(2) \rightarrow 2$
948.8	6.1	0.51(9)	E1	$59/2^-$	$\rightarrow$	$57/2^+$	$6 \rightarrow 5$
982.2	3.4			$(73/2^+)$	$\rightarrow$	$69/2^+$	$5a$
997.4		0.92(14)	E2	$87/2^-$	$\rightarrow$	$83/2^-$	c
1015.4	2.0	0.51(4)	M1/E2	$(41/2^+)$	$\rightarrow$	$39/2^+$	$(5) \rightarrow 3$
1033.9	5.8	1.5(3)	E2	$67/2^-$	$\rightarrow$	$63/2^-$	2
1041.8	2.4			$(77/2^-)$	$\rightarrow$	$73/2^-$	2
1042.4	3.9			$65/2^+$	$\rightarrow$	$61/2^+$	$5a$
1057.1	8.8	0.97(3)	E2	$65/2^+$	$\rightarrow$	$61/2^+$	$5a \rightarrow 5$
1063.4	0.1			$(89/2^+)$	$\rightarrow$	$(85/2^+)$	$7b$
1086.2	5.0	1.28(16)	E2	$(71/2^-)$	$\rightarrow$	$(67/2^-)$	6
1095.1	6.2	1.16(4)	E2	$61/2^+$	$\rightarrow$	$57/2^+$	$5a \rightarrow 5$

TABLE 5.1 CONTINUED.

E_γ (keV)[a]	I_γ[b]	R[c]	Multipolarity	Assignment			Band[d]
1102.2	2.9	1.4(5)	E2	$65/2^-$	$\rightarrow$	$61/2^-$	2
1142.9	0.8	1.6(4)	E2	$87/2^-$	$\rightarrow$	$83/2^-$	c
1159.1	0.7	0.72(9)	E1	$77/2^+$	$\rightarrow$	$75/2^-$	$7b \rightarrow 6$
1208.8	3.5	1.20(12)	E2	$65/2^+$	$\rightarrow$	$61/2^+$	$5a \rightarrow 5$
1287.5				$(87/2^-)$	$\rightarrow$	$83/2^-$	c
1331.5				$(87/2^-)$	$\rightarrow$	$83/2^-$	c
1598.3		1.00(12)	E2	$85/2^+$	$\rightarrow$	$81/2^+$	c
1882.6	2.5	1.23(9)	E2	$83/2^-$	$\rightarrow$	$79/2^-$	$c \rightarrow 6$
1926.6	2.3	1.12(8)	E2	$83/2^-$	$\rightarrow$	$79/2^-$	$c \rightarrow 6$

[a] The γ-ray energies are estimated to be accurate to $\pm$0.3keV.

[b] Intensities quoted as a percentage of the 377 keV ($15/2^- \rightarrow 11/2^-$) γ ray. Errors are estimated to be less than 5% of the quoted values for strong transitions ($I_\gamma > 10$) and less than 10% of the quoted values for the weaker transitions. Intensities for the weakest transitions ($I_\gamma \ll 1$) are not shown.

[c] angular-intensity ratios, R. Pure stretched dipoles typically have $R = 0.7$, while quadrupoles have $R = 1.1$.

[d] Where a level does not clearly belong to a particular band structure, the number of the band it is most closely associated with is given in parentheses. Levels thought to be built on core-breaking excitations above the terminating $I = 79/2^-$ state, which not belonging to 7a or 7b, are labelled with the letter c.

5.2 Discussion

It is useful to be aware which orbitals lie near the Fermi surface for both protons and neutrons as it is these which are most likely to contribute to the underlying configurations of the observed band structures. Using the plots of theoretical single particle energies as a function of quadrupole deformation in Fig. 2.5, it can be seen that for a prolate shape ($\varepsilon_2 \sim 0.2$) in ^{155}Ho, the $N = 88$ Fermi level lies below the first $N_{\rm osc} = 6$ ($\nu i_{13/2}$) intruder orbital and above the first three $N_{\rm osc} = 5$ ($\nu f_{7/2}/h_{9/2}$) orbitals. For an oblate shape ($\varepsilon_2 \sim -0.2$), the $N = 88$ Fermi level lies above the first $\nu f_{7/2}$, $\nu h_{9/2}$, and $\nu i_{13/2}$ orbitals. The relevant high-j orbitals near the $Z = 67$ Fermi surface arise from states in the middle of the $N_{\rm osc} = 5$ subshell ($\pi h_{11/2}$) and from the states at the top of the $N_{\rm osc} = 4$ subshell ($\pi d_{5/2}/g_{7/2}$ and $\pi d_{3/2}$).

The rotational bands in ^{155}Ho may also be interpreted in terms of quasiparticle configurations within the framework of Woods-Saxon cranking calculations. Quasiparticle Routhians, e', are displayed as a function of frequency in Figures 5.5 and 5.6 for $\gamma = 0°$ and $\gamma = -20°$, respectively. The reason for performing the calculations twice using different values for the γ deformation will become apparent when discussing the staggering of band 2, and how the $\pi h_{11/2}$ proton can favour an axially asymmetric shape. The labelling convention set out in Table 5.3 will be used for quasiparticle configurations.

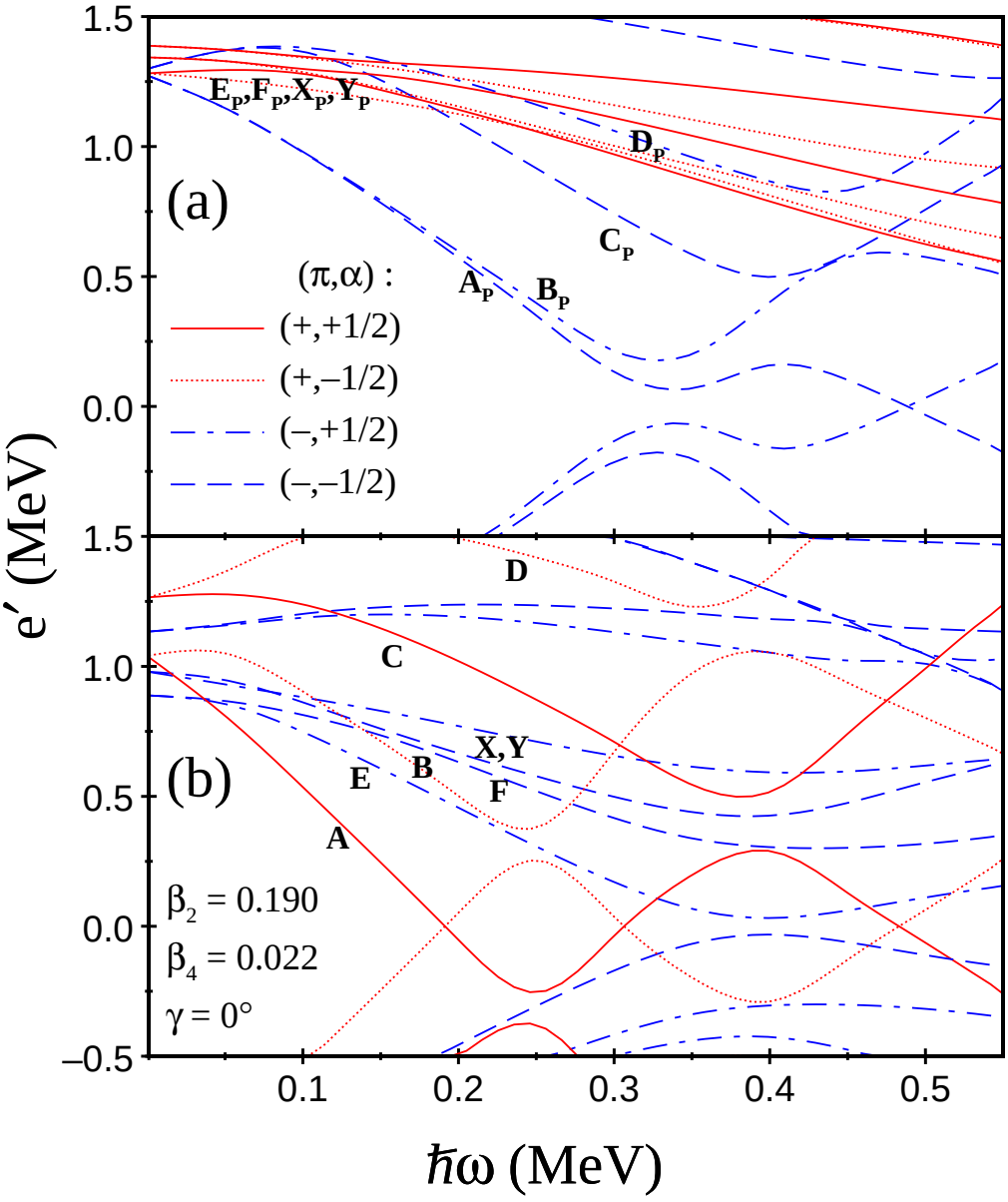

FIGURE 5.5: Cranked Woods-Saxon Routhian diagrams for ^{155}Ho, calculated using deformation parameters from Möller and Nix [29]. Axial symmetry ($\gamma = 0°$) is assumed. (a) Quasiprotons. (b) Quasineutrons.

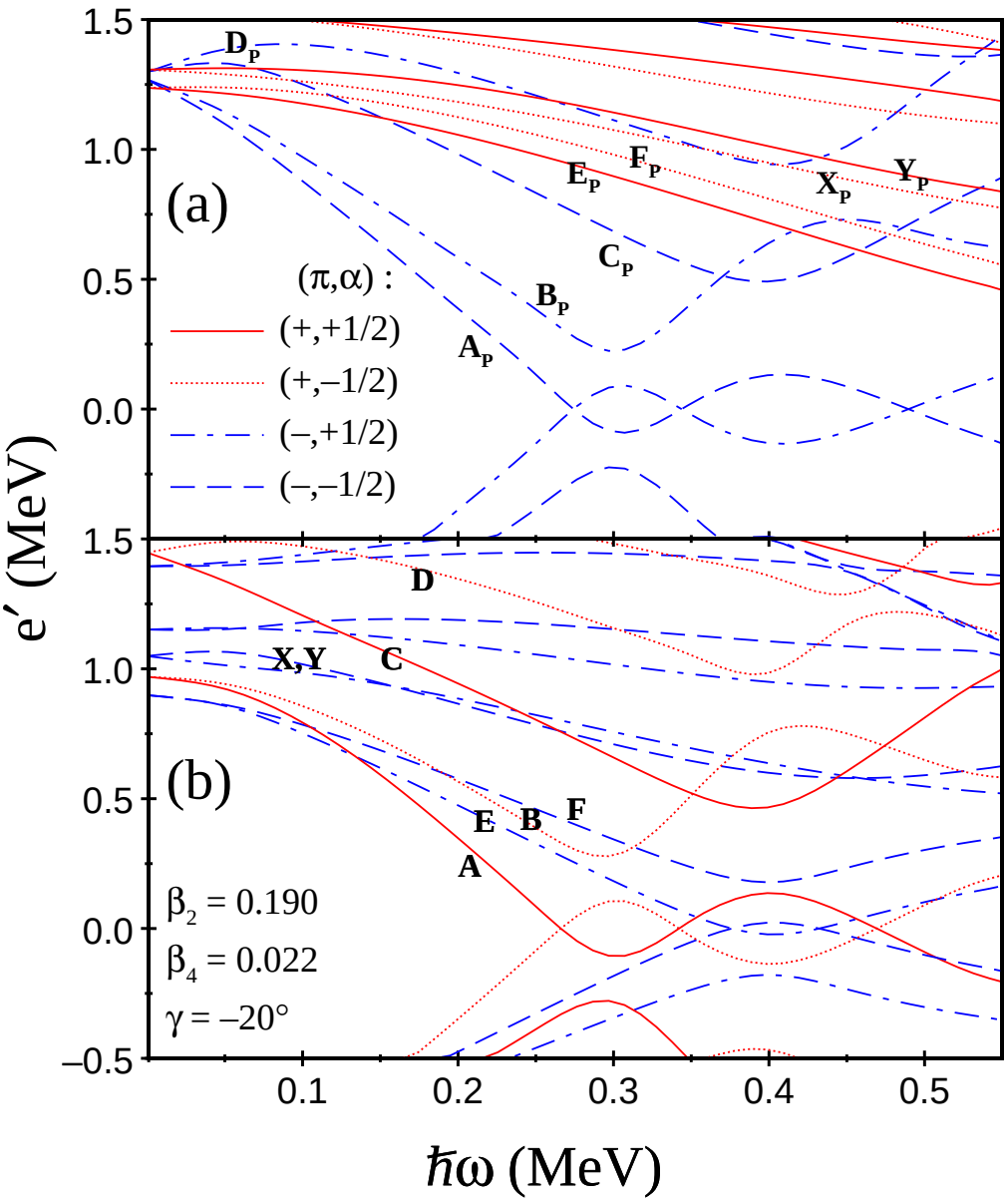

FIGURE 5.6: Cranked Woods-Saxon Routhian diagrams for ^{155}Ho, calculated using deformation parameters from Möller and Nix [29]. Slight triaxial deformation ($\gamma = -20°$) is assumed. (a) Quasiprotons. (b) Quasineutrons.

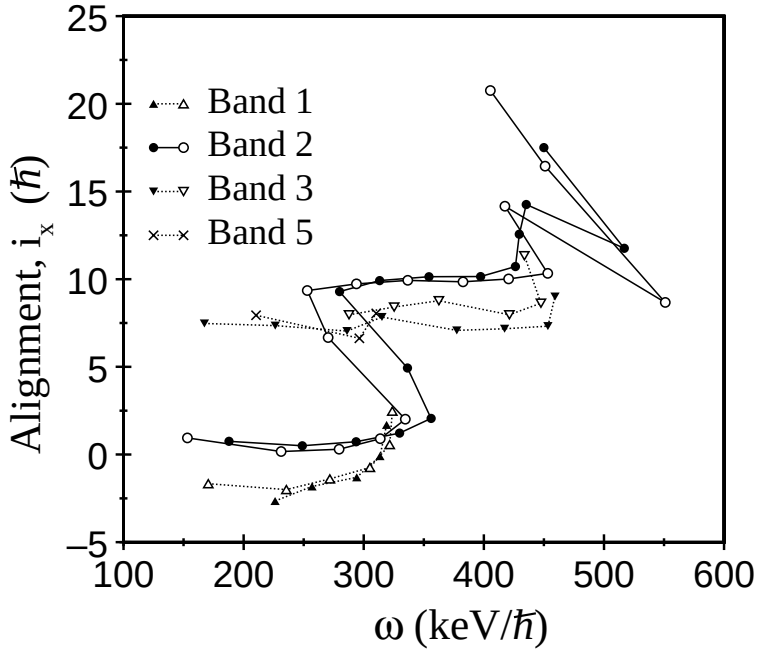

FIGURE 5.7: Experimental alignments, i_x, as a function of rotational frequency, ω, for the non-terminating bands 1-4. Harris parameters $\mathcal{J}_0 = 32.1\ \hbar^2\text{MeV}^{-1}$ and $\mathcal{J}_1 = 34.0\ \hbar^4\text{MeV}^{-3}$ have been used.

5.2.1 Alignment properties of the bands

In order to investigate the rotational properties of the bands in ^{155}Ho, the experimental alignments [27],

$$i_{\text{x}}(\omega) = I_{\text{x}}(\omega) - I_{\text{x,ref}}(\omega), \tag{5.2}$$

are shown in Fig. 5.7, plotted as a function of rotational frequency, $\omega = E_\gamma/\Delta I_x \approx E_\gamma/2\hbar$. At a given spin I, the aligned spin is $I_{\text{x}} = \sqrt{I(I+1) - K^2}$, while the rotational reference, $I_{\text{x,ref}}$, is given by

$$I_{\text{x,ref}}(\omega) = \omega(\mathcal{J}_0 + \mathcal{J}_1\omega^2). \tag{5.3}$$

Harris parameters [31] $\mathcal{J}_0 = 32.1\ \hbar^2\text{MeV}^{-1}$ and $\mathcal{J}_1 = 34.0\ \hbar^4\text{MeV}^{-3}$, obtained from ^{157}Ho [81], have been used.

TABLE 5.2: Measured Branching ratios, λ, and experimental $B(M1)/B(E2)$ ratios of reduced transition probabilities in ^{155}Ho.

I ($\hbar$)	$E_\gamma(I \to I-1)$ (keV)	$E_\gamma(I \to I-2)$ (keV)	Branching ratio λ $I_\gamma(M1)/I_\gamma(E2)$	$B(M1)/B(E2)$ $(\mu_N/eb)^2$
		band 1		
$9/2^+$	234	344	3.1(3)	0.81(8)
$11/2^+$	221	455	0.45(6)	0.56(7)
$13/2^+$	252	473	0.27(3)	0.28(3)
$15/2^+$	263	515	0.25(5)	0.35(7)
$17/2^+$	282	545	0.38(7)	0.57(10)
$19/2^+$	307	589	0.29(3)	0.49(5)
		band 2		
$13/2^-$	396	308	6.6(15)	0.20(4)
$17/2^-$	483	463	0.88(7)	0.116(9)
$21/2^-$	544	560	0.59(7)	0.142(18)
$25/2^-$	584	628	0.32(5)	0.109(16)
$27/2^-$	76	588	0.0067(6)	0.76(7)
$29/2^-$	593	670	0.36(4)	0.162(18)
$31/2^-$	119	713	0.0149(11)	1.14(8)
$33/2^-$	421	541	1.29(22)	0.56(9)
$35/2^-$	252	673	0.24(3)	1.45(17)
$39/2^-$	305	560	0.65(6)	0.88(9)
$47/2^-$	380	709	0.56(9)	1.28(19)
$49/2^-$	386	765	0.28(3)	0.90(9)
$51/2^-$	409	795	0.25(5)	0.80(16)
$53/2^-$	432	841	0.238(25)	0.87(9)
$55/2^-$	421	853	0.69(25)	2.3(7)
$57/2^-$	486	906	0.260(25)	0.97(9)
$61/2^-$	462	835	0.33(7)	0.95(21)
$63/2^-$	409	871	0.69(5)	3.5(3)
		band 3		
$31/2^+$	187	453	0.110(9)	0.224(19)
$35/2^+$	227	572	0.040(5)	0.146(19)
$37/2^+$	349	576	4.6(8)	4.9(9)
$39/2^+$	282	631	0.056(8)	0.174(24)
$41/2^+$	369	651	1.64(16)	2.7(3)
$43/2^+$	386	755	0.103(7)	0.308(22)
$45/2^+$	339	725	1.42(16)	5.1(6)
$49/2^+$	347	843	0.37(4)	2.6(3)

5.2.2 B(M1)/B(E2) Ratios

For the rotational bands 1, 2, and 3, which include levels of both $\alpha = -1/2$ and $\alpha = +1/2$ signature values, experimental $B(M1)/B(E2)$ cascade-to-crossover transition strength ratios have been determined from the measured branching ratios, $\lambda = I_\gamma(\Delta I = 1)/I_\gamma(\Delta I = 2)$. The $B(M1; I \rightarrow I-1)/B(E2; I \rightarrow I-2)$ ratio of reduced transition probabilities was calculated using

$$\frac{B(M1)}{B(E2)} = \frac{\lambda}{1.43} \frac{[E_\gamma(\Delta I = 2)]^5}{[E_\gamma(\Delta I = 1)]^3} (\mu_N/eb)^2, \tag{5.4}$$

with γ-ray energies in MeV. The $\Delta I = 1$ transitions were assumed to be pure stretched dipole in character, with an $E2/M1$ multipole mixing ratio $\delta \equiv 0$. Although for nonzero δ Eq. 5.4 should be modified by a factor of $(1+\delta^2)^{-1}$, the effect this has is small, since typically $\delta^2 \ll 1$. Indeed, the errors introduced by the experimental branching ratios λ are significantly larger than the effect of neglecting δ. The experimental $B(M1)/B(E2)$ ratios are presented in Table 5.2, together with the measured branching ratios, and are plotted in Fig. 5.8. Also presented in Fig. 5.8 are $B(M1)/B(E2)$ calculations performed using the geometric model of Dönau and Frauendorf [14] for the proposed configuration of each structure.

5.2.3 Rotational structures: bands 1-4

Specific configurations have been proposed for the rotational bands 1 to 4 based on their alignment properties and their relative energies. These are given in Table 5.4 in terms of quasiparticle configurations.

Band 1

The $I^\pi = 5/2^+$ ground state of ^{155}Ho corresponds to the [402]5/2 proton orbital at the top of the $\pi d_{5/2}$ subshell [88]. As such, band 1 may be interpreted as a rotational

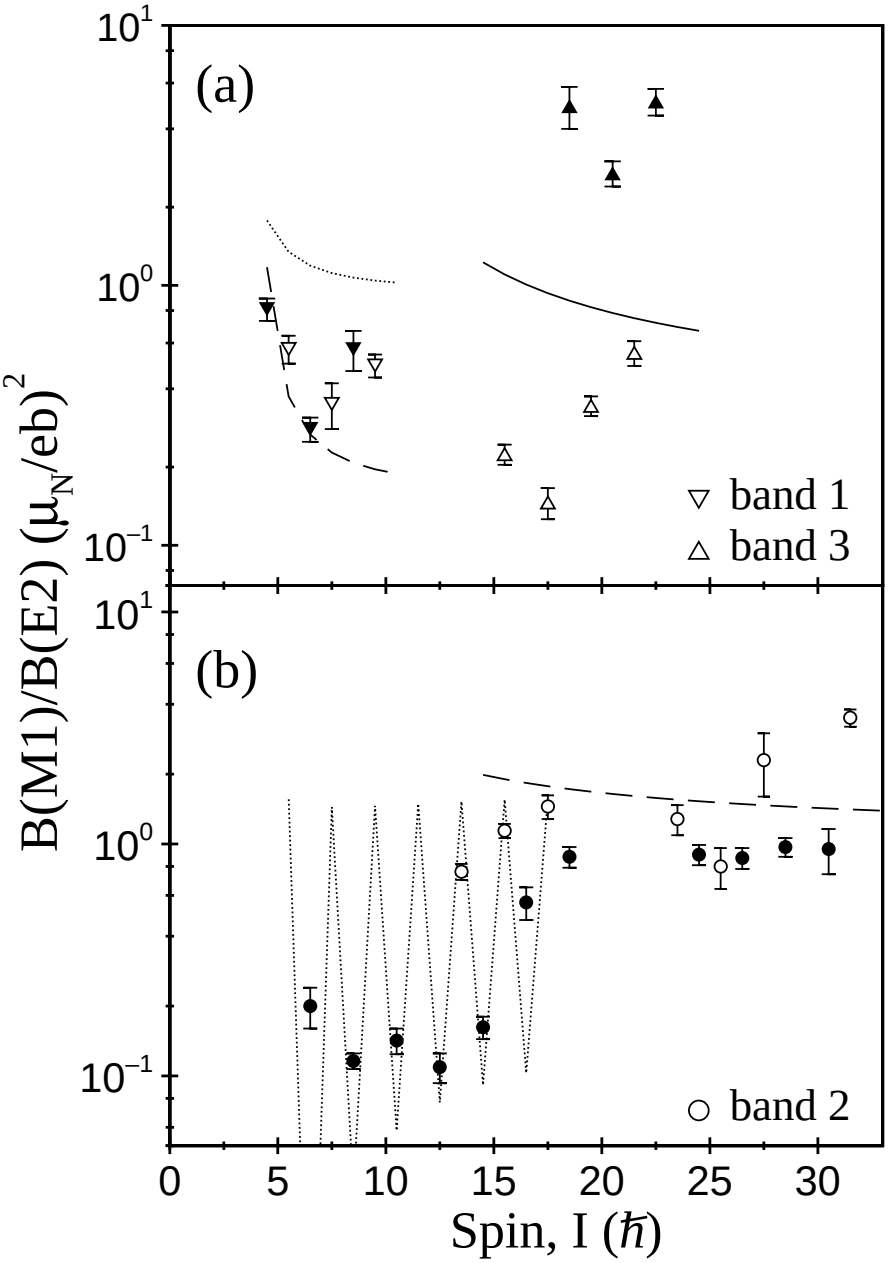

FIGURE 5.8: Values of $B(M1; I \rightarrow I-1)/B(E2; I \rightarrow I-2)$, calculated from measured γ-ray branching ratios for (a) positive-parity bands 1 and 3, and (b) the negative parity band 2. The results are listed in Table 5.2. The lines show the results of calculations using the geometric models of Dönau and Frauendorf [14]. In plot (a) calculations have been made for the $[402]5/2^+$ $\pi d_{5/2}$ orbital (dotted line), the $[404]7/2^+$ $g_{7/2}$ orbital (dashed), and the A_pAE quasiparticle configuration (solid.) In plot (b) the calculations are made for the $[523]7/2^+$ $\pi h_{11/2}$ orbital (dotted line) including a signature-splitting term, and for the same orbital plus an $i_{13/2}$ neutron alignment, this time with no signature splitting term. Filled and empty symbols represent $\alpha = +1/2$ and $\alpha = -1/2$ signatures, respectively.

TABLE 5.3: Quasiparticle labelling scheme for ^{155}Ho.

Label	$(\pi, \alpha)_n$	Main shell model component
	Quasineutrons	
A	$(+, +1/2)_1$	$i_{13/2}[651]3/2$
B	$(+, -1/2)_1$	$i_{13/2}[651]3/2$
C	$(+, +1/2)_2$	$i_{13/2}[660]1/2$
D	$(+, -1/2)_2$	$i_{13/2}[660]1/2$
E	$(-, +1/2)_1$	$h_{9/2}[521]3/2$
F	$(-, -1/2)_1$	$h_{9/2}[521]3/2$
X	$(-, +1/2)_2$	$h_{11/2}[505]11/2$
Y	$(-, -1/2)_2$	$h_{11/2}[505]11/2$
	Quasiprotons	
A_P	$(-, -1/2)_1$	$h_{11/2}[523]7/2$
B_P	$(-, +1/2)_1$	$h_{11/2}[523]7/2$
C_P	$(-, -1/2)_1$	$h_{11/2}[532]5/2$
D_P	$(-, +1/2)_1$	$h_{11/2}[532]5/2$
E_P	$(+, -1/2)_1$	$g_{7/2}[404]7/2$
F_P	$(+, +1/2)_1$	$g_{7/2}[404]7/2$
X_P	$(+, -1/2)_2$	$d_{5/2}[402]5/2$
Y_P	$(+, +1/2)_2$	$d_{5/2}[402]5/2$

band built on the [402]5/2 proton configuration, with the $7/2^+$ level located at 110 keV representing the first rotational level. However, Foin *et al.* [86] proposed that this state represents the [404]7/2 intrinsic state of the $\pi g_{7/2}$ subshell, decaying to the ground state via the 110 keV transition. The measured $B(M1)/B(E2)$ ratios for band 1, which are plotted alongside calculations for the two orbitals in Fig. 5.8, appear to support this interpretation, the values being in better agreement with the calculations for a $g_{7/2}$ proton than those for a $d_{5/2}$ proton. In Fig. 5.7 it can be seen that at $\omega \approx 0.3$ MeV/$\hbar$, band 1 experiences the beginnings of an upbend or backbend. This is the frequency expected for the AB quasiparticle alignment of two $i_{13/2}$ neutrons.

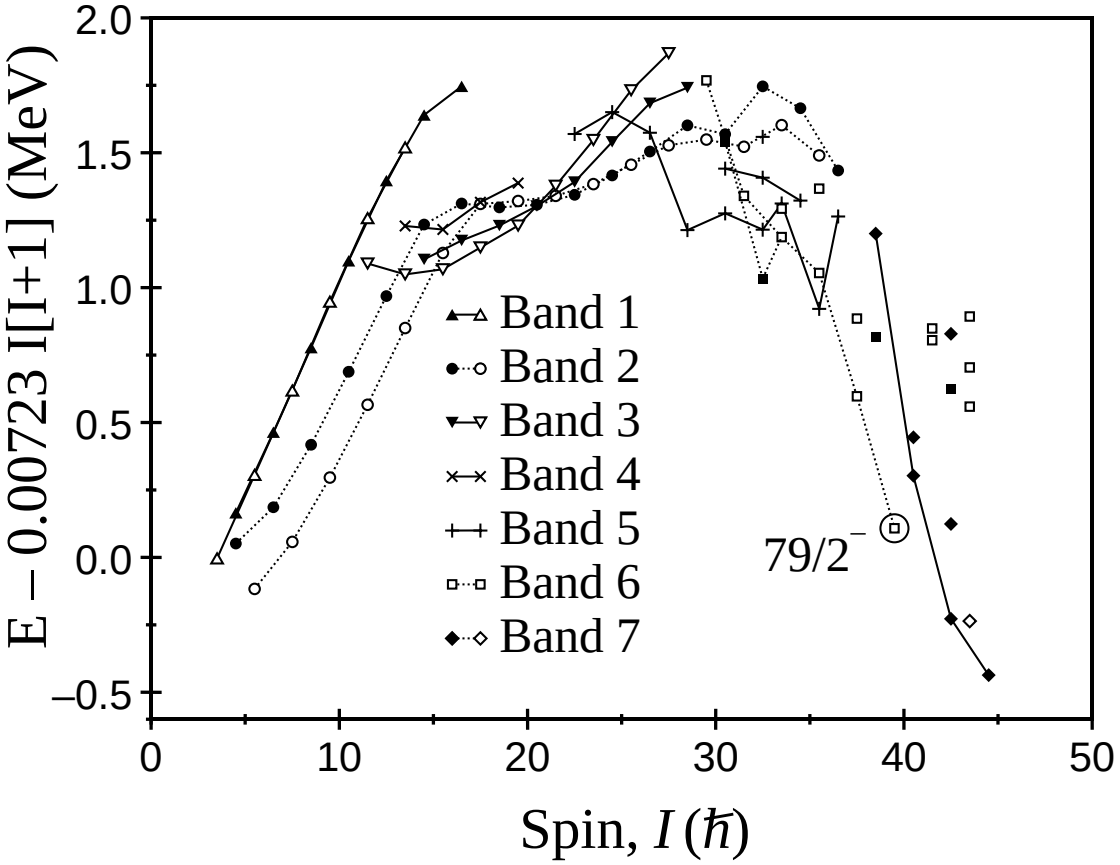

FIGURE 5.9: Level energies in ^{155}Ho, plotted as a function of spin, relative to a rotating reference.

Band 2

Band 2 is built on the $\pi h_{11/2}$ orbital $[523]7/2^-$ [86]. In Fig. 5.7 it can be seen that band 2 experiences a backbend, resulting in a gain in alignment at $\omega \approx 0.3$ MeV/$\hbar$ of $\sim 10\hbar$. This is understood in terms of a rotational alignment of a pair of $i_{13/2}$ neutrons. In the nomenclature of Table 5.3, band 2 has a A_P and B_P quasiparticle configuration below the backbend for its $\alpha = -1/2$ and $\alpha = +1/2$ signature components, respectively. Above the backbend its quasiparticle configuration is A_PAB and B_PAB.

Fig. 5.7 also shows what may be a second alignment corresponding to an upbend at $\omega \approx 0.45$ MeV/$\hbar$. Since the A_P (B_P) quasiproton is already present in the

$\alpha = -1/2$ ($\alpha = +1/2$) signature of band 2, an $A_P B_P$ alignment of two $h_{11/2}$ protons is blocked. The next allowed crossings are $B_P C_P$ for the $\alpha = -1/2$ levels, and $A_P D_P$ for the $\alpha = +1/2$ levels. The cranked Woods-Saxon calculations of Figures 5.5(a) and 5.6(a) show that both crossings are expected to occur at a frequency of approximately 0.4 MeV/$\hbar$. It was proposed by Radford *et al.* [89] that similar upturns in aligned angular momentum at the top of the $\pi h_{11/2}$ band of ^{157}Ho correspond to such $B_P C_P$ and $A_P D_P$ crossings. Another possibility, given the erratic nature of the increase in alignment, is that it may simply be another example of the breakdown in rotational behaviour in this nucleus at spin ~ 30.

Due to the low energy of the $\alpha = -1/2 \rightarrow \alpha = +1/2$ transitions, it has only been possible to measure the $B(M1)/B(E2)$ ratios of the highest of the $\alpha = -1/2$ levels, $27/2^-$, $31/2^-$ and $35/2^-$, before the backbend. Even so, the measured $B(M1)/B(E2)$ ratios exhibit a strong signature dependence which disappears in levels above the backbend. Calculations made using the geometric model of Dönau and Frauendorf reproduce signature dependence of this kind when a signature splitting term is introduced. Indeed, a notable feature of band 2 is the large signature-splitting it exhibits at low spin, of order 0.25 MeV, which disappears above the backbend at around spin 35/2. The calculations shown in Fig. 5.8 have been made for the [523]$7/2^-$ $\pi h_{11/2}$ orbital including a signature-splitting term, and for the same orbital plus an $i_{13/2}$ neutron alignment, this time with no signature splitting term.

In the quasiparticle level diagrams of Figures 5.5(a) and 5.6(a) it can be seen that the lowest energy positive-parity configurations (E_P, F_P, X_P, Y_P) and the lowest energy negative-parity configurations (A_P, B_P) are very close in energy at $\hbar\omega = 0$, that is when the nucleus is not rotating. With increasing angular frequency, $\hbar\omega$, A_P and B_P quickly become the favoured configurations. Experimentally it is seen that above the positive-parity $\pi d_{5/2}$ ground state, the negative-parity band 2 is yrast.

The difference in steepness in the positive and negative-parity quasiparticle levels manifests itself in the fact that band 2 has greater alignment, i_x than band 1, with $\Delta i_x \approx 2\hbar$, $\mathrm{A}_P/\mathrm{B}_P$ having a gradient approximately twice that of $\mathrm{E}_P/\mathrm{F}_P$.

Band 3

The positive-parity band 3 passes through the AB crossing region without experiencing any increase in aligned angular momentum, which suggests the AB crossing is blocked and its quasiparticle configuration already involves an $i_{13/2}$ neutron. Its gain in alignment of $\sim 8\hbar$ relative to the band 2 $\pi h_{11/2}$ configuration is consistent with a $\pi(h_{11/2})\otimes\nu(i_{13/2}h_{11/2})$ configuration. Strangely, the measured $B(M1)/B(E2)$ values show a striking signature dependence; the $\alpha = -1/2$ levels are strongly populated from $\alpha = +1/2$ decays, but the decays in the opposite direction are few in comparison. By introducing a signature splitting term to the A_PAE geometric model calculations, such signature dependence can be reproduced, but the splitting must be approximately 0.2 MeV in magnitude, with $\alpha = +1/2$ being the favoured signature. In reality, while some splitting is observed, it is much smaller (less than 0.1 MeV) and there is a reversal in the favoured signature at $I \approx 21$, below which $\alpha = -1/2$ is favoured. Cranked shell model calculations put this three-quasiparticle configuration at the lowest energy, lower in fact than the $\mathrm{A}_P\mathrm{AB}$ configuration, which tallies with the fact that the band is yrast at spins $31/2 \rightarrow 39/2$, and makes other interpretations of its structure unlikely. The effects of triaxiality on the signature dependence of $B(M1)/B(E2)$ ratios has been discussed in Ref. [90].

Band 4

Band 4 has $\alpha = -1/2$ and has a similar alignment to band 3. When the energies of band 4 are plotted as a function of spin in Fig. 5.9, it can be seen that it is higher in energy than band 3, lying at a similar energy to band 2 at the AB neutron

TABLE 5.4: Proposed quasiparticle configurations of rotational bands in ^{155}Ho.

Band	(π, α)	Configuration
1	$(+, -1/2)$	E_P
	$(+, +1/2)$	F_P
2	$(-, -1/2)$	$A_P \rightarrow A_PAB \rightarrow A_PB_PC_PAB$
	$(-, +1/2)$	$B_P \rightarrow B_PAB \rightarrow A_PB_PD_PAB$
3	$(+, +1/2)$	A_PAE
	$(+, -1/2)$	B_PAE
4	$(+, -1/2)$	A_PAF

crossing. The A_PAF three-quasiparticle configuration is predicted to be at a higher energy than the A_PAE configuration, and to be competitive with the A_PAB configuration. Relative to the $h_{11/2}[523]7/2^-$ proton, the A_PAF configurations would be expected to have a gain in alignment similar to that of the A_PAE configuration, which agrees with what is seen in Fig. 5.7. For these reasons, it is proposed that band 4 corresponds to the A_PAF three-quasiparticle configuration.

5.2.4 Signature splitting and total Routhian calculations

A staggering parameter, $S(I)$, which characterizes the degree of splitting between the energies of the $\alpha = 1/2$ and $\alpha = -1/2$ signature components of a band [91], has been measured for the rotational bands 1-3 (see Fig. 5.10) and is defined as:

$$S(I) = E(I) - E(I-1) - \frac{1}{2}[E(I+1) - E(I) + E(I-1) - E(I-2)]. \qquad (5.5)$$

While band 1 exhibits little staggering, there is a large signature splitting observed in band 2, which disappears at $I \approx 15$ at the first $i_{13/2}$ neutron alignment. At the highest spins in band 2, the staggering returns, perhaps reflecting a further change in its structure. Band 3 exhibits some signature splitting, though not to the same

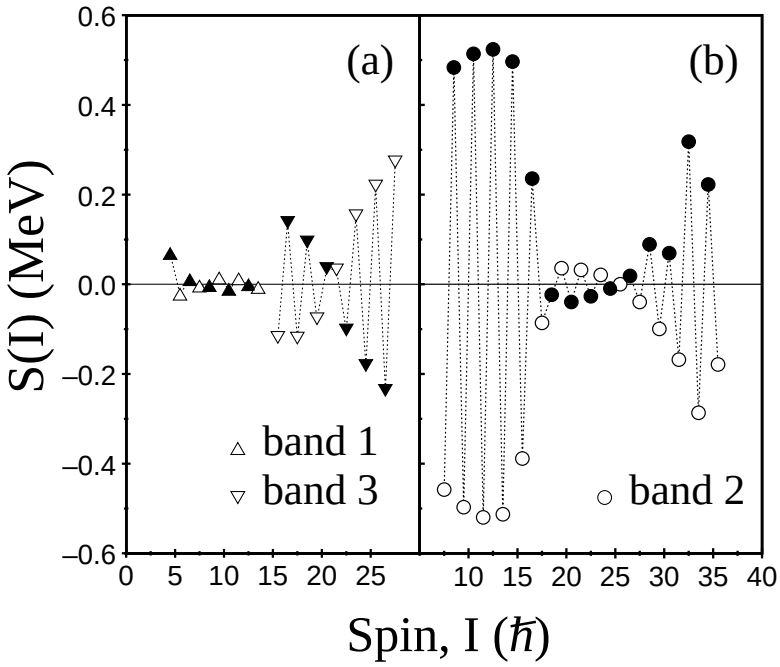

FIGURE 5.10: Staggering parameter $S(I)$ as a function of spin I for (a) positive parity bands 1 and 3, and (b) negative parity band 2 in ^{155}Ho. The solid and open symbols represent $\alpha = +1/2$ and $\alpha = -1/2$ signatures, respectively.

extent as band 2, with a signature inversion occurring at $I \approx 21$, below which the $\alpha = -1/2$ signature component is favoured.

The unusually large signature splitting observed in band 2 demands explanation and, previously, it has been interpreted as evidence of triaxiality at low spin [1, 92]. Large staggering between the signature partners of a configuration corresponding to a $h_{11/2}$ proton can be reproduced in cranked shell model calculations by allowing the nucleus to adopt an axially asymmetric shape, expressed by a non-zero value for the γ deformation. Fig. 5.11 shows calculations for the total Routhians of different quasiparticle configurations, calculated by summing the single-particle Routhians from cranked shell model calculations using a Modified Harmonic Oscillator potential with a γ-dependent reference [92]:

$$E'(\omega, \gamma) = \sum_{\mu} e'_{\mu}(\omega, \gamma) + E'_{ref}(\omega, \gamma). \tag{5.6}$$

In this equation, e'_μ are the single-particle energies calculated using the cranked shell model, and E'_{ref} is the γ-dependent reference, determined using

$$E'_{ref}(\omega,\gamma) = \frac{1}{2}V_{PO}\cos(3\gamma) - \frac{2}{3}\omega^2\left(J_0 + \frac{1}{2}\omega^2 J_1\right)\cos^2(\gamma + 30^\circ), \qquad (5.7)$$

where V_{PO} is the prolate-oblate energy difference (-0.4 MeV has been used here) and $\mathcal{J}_{0,1}$ are the Harris parameters used in Fig. 5.7. An angular frequency of $\omega = 0.2$ MeV/$\hbar$ has been used. The calculations show that the $\pi h_{11/2}$ configuration (A_P and B_P in Fig. 5.11(b)) has minimum energy at $\gamma \approx -22.5^\circ$. Moreover, at this favoured deformation there is significant splitting between the A_P and B_P configurations, which represent the signature partners of the $\pi h_{11/2}$ configuration, $\alpha = -1/2$ being the favoured signature. This agrees with experiment, as the $\alpha = -1/2$ levels of band 2 lie lower in energy than the $\alpha = +1/2$ levels. The Woods-Saxon cranking calculations of Fig. 5.6(a) also show that an axially asymmetric shape ($\gamma = -20^\circ$) coincides with splitting of the A_P and B_P levels.

In contrast, very little splitting is predicted for the $\pi d_{5/2}/g_{7/2}$ configurations. Adding the AB $i_{13/2}$ neutron alignment to the $h_{11/2}$ proton (A_PAB and B_PAB in Fig. 5.11(b)) has the effect of quenching both the γ deformation and the signature splitting. This is in accord with the large staggering observed at the bottom of band 2, but not above the backbend. Similarly, The calculations for the configurations corresponding to band 3, a $h_{11/2}$ proton coupled to the a $\nu(i_{13/2}h_{11/2})$ configuration (A_PAE and B_PAE in Fig. 5.11(a)) show quenching of the signature-splitting and γ deformation. The highest levels of band 2 have been interpreted as a $\mathrm{A}_P\mathrm{B}_P\mathrm{C}_P$AB and $\mathrm{A}_P\mathrm{B}_P\mathrm{D}_P$AB configuration for the $\alpha = -1/2$ and $\alpha = +1/2$, respectively. The total Routhian calculations for these configurations show a return of signature splitting, in agreement with the staggering observed at the top of band 2, and favour an axially symmetric shape ($\gamma = 0^\circ$).

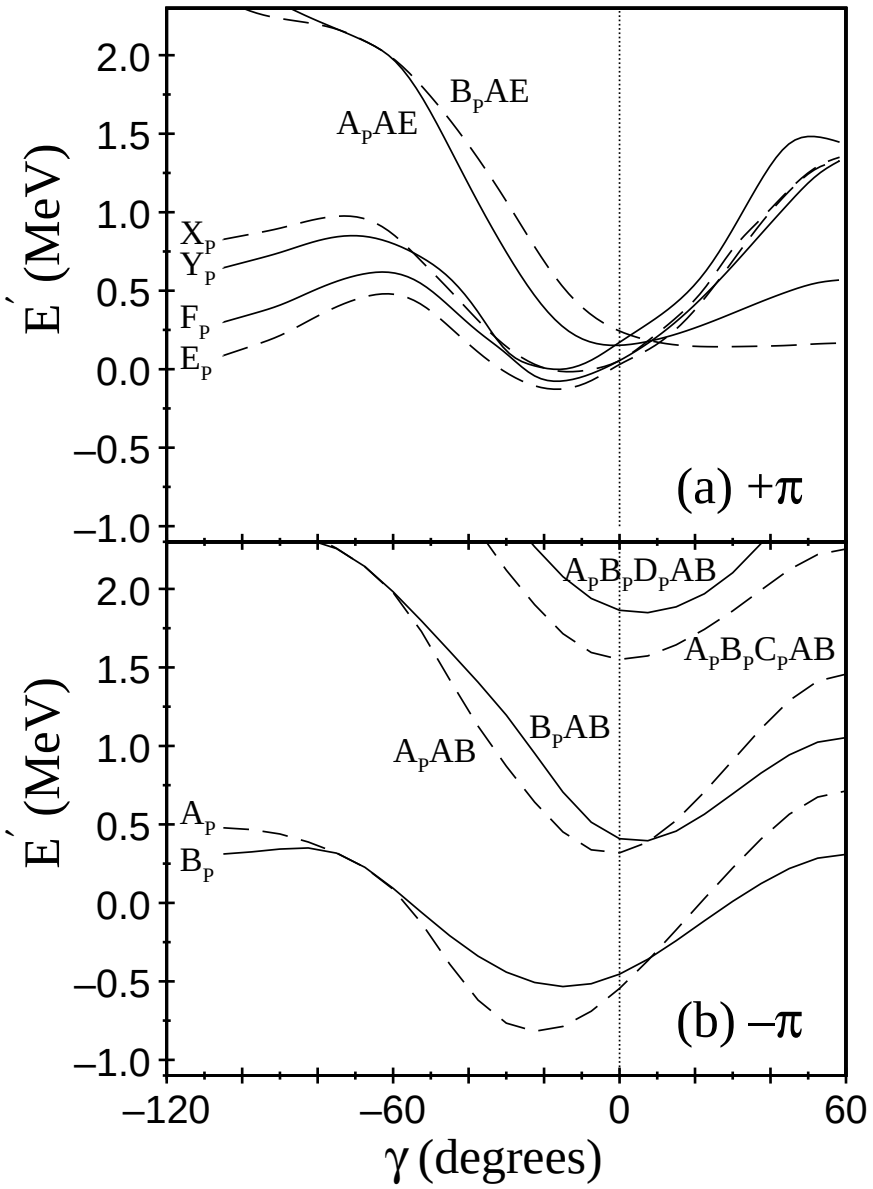

FIGURE 5.11: Cranked shell model calculations made using a modified harmonic oscillator potential. Total Routhians presented as function of γ deformation for (a) positive-parity configurations and, (b) negative-parity configurations. Solid lines signify $\alpha = +1/2$ signature and dashed, $\alpha = 1/2$ signature.

In this light, the signature splitting observed at low spins can be seen as indirect evidence of triaxiality in ^{155}Ho, driven by the $\pi h_{11/2}$ orbital. A complex picture emerges of the shape evolution of ^{155}Ho, in which competing triaxial and prolate shapes, built on $h_{11/2}$ and $d_{5/2}/g_{7/2}$ protons respectively, coexist at low spin, with a triaxial-prolate transition occurring in band 2 at the $\nu i_{13/2}$ alignment.

Signature-splitting in $\pi h_{11/2}$ bands is observed in other nuclei in this region, and has been interpreted similarly [93, 94, 95]. Fig. 5.12 shows the staggering of band 2 with that of $\pi h_{11/2}$ bands of neighbouring $N = 88$ isotones [93, 96, 97] and holmium isotopes [89, 94]. In all the nuclides shown staggering is observed at low spin, which largely disappears at spin $\sim 15\hbar$. While staggering of a similar magnitude is seen for the $N = 88$ isotones, increasing the number of neutrons lessens the observed signature splitting of the $\pi h_{11/2}$ band. As discussed in the previous chapter, ^{155}Ho, like ^{156}Er, lies in a transitional region: between $N = 88$ and $N = 92$ there is a move from γ-softness to prolate rotational behaviour.

Comparing the staggering of the $\pi h_{11/2}$ band of ^{155}Ho to that of the $\pi h_{11/2}$ band of ^{157}Ho in Fig. 5.12(b) reveals that the return of staggering at spin $\sim 28\hbar$ in band 2 of ^{155}Ho is also seen in ^{157}Ho. This similarity in behaviour supports the view that ^{155}Ho experiences the same $B_P C_P$ and $A_P D_P$ crossings at the top of band 2 that have been reported in ^{157}Ho [89].

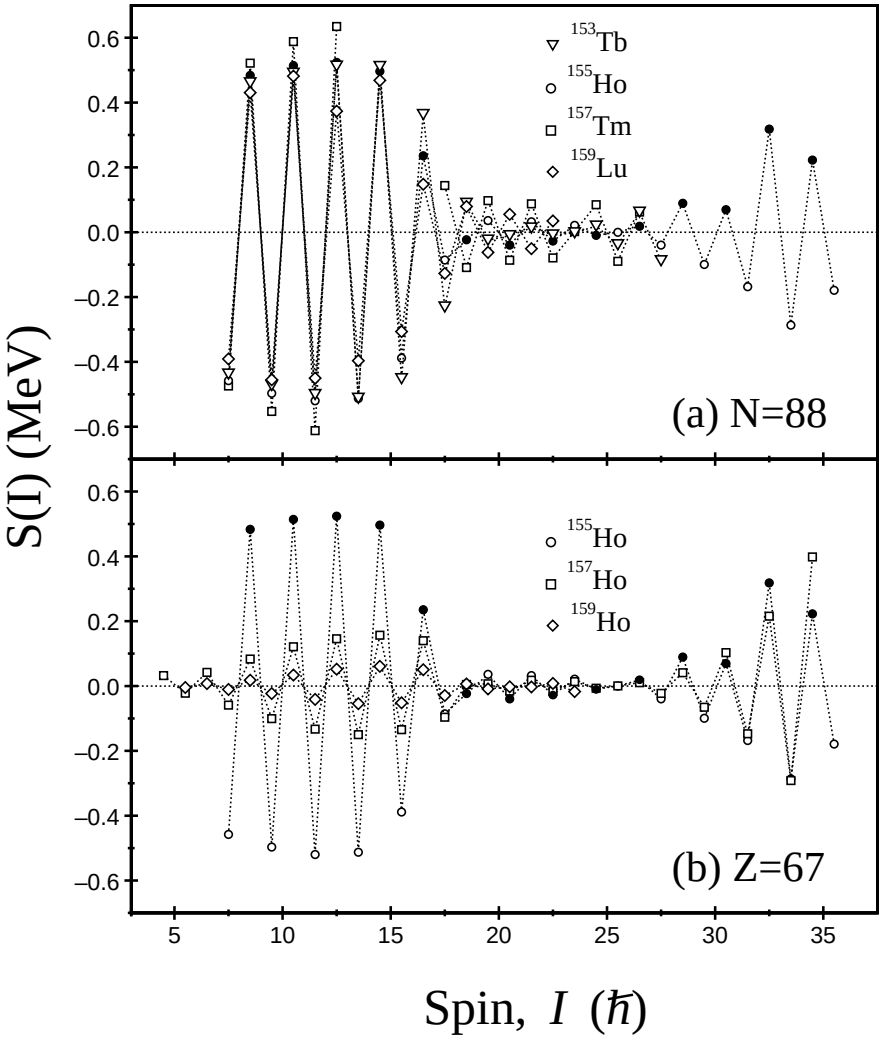

FIGURE 5.12: Staggering parameter $S(I)$ as a function of spin I for (a) $N = 88$ isotones and (b) $Z = 67$ (holmium) isotopes. The solid and open symbols of ^{155}Ho represent $\alpha = +1/2$ and $\alpha = -1/2$ signatures, respectively.

5.2.5 Terminating structures

Cranked Nilsson Strutinsky calculations

To help interpret the high-spin behaviour of ^{155}Ho, theoretical calculations have been performed in the framework of the configuration-dependent cranked Nilsson-Strutinsky (CNS) formalism [5, 32] by I. Ragnarsson [103]. For the κ and μ Nilsson model parameters, which define the $\mathbf{l}\cdot\mathbf{s}$ and $\mathbf{l}^2$ strengths of the modified oscillator potential, the A=150 parameters of Ref. [21] have been used. The calculations do not take into account the effect of pairing, and as a result can only be considered realistic at relatively high spin ($I \geq 30\hbar$). In Fig. 5.14 energy calculations are shown alongside the experimental energies of levels in bands 2, 6, 6a, 7a, and 7b, and levels lying above the $79/2^-$ state of band 6.

Terminating structures in band 6 and above

When the energy levels of band 6 are drawn relative to a rotating reference, as in Figures 5.9 and 5.14, the band slopes strongly downwards, and terminates at a particularly favoured state at $I = 79/2$. Termination is expected at $I = 79/2$ since this is the highest spin that can be formed in ^{155}Ho from the nine valence nucleons (three protons and six neutrons) outside the spherical ^{146}Gd core. Studies into the band terminating properties of other $N = 88$ isotones have shown there is a terminating neutron configuration which generates a spin contribution of 26^+. This configuration can be written as $\nu\left\{(i_{13/2})^2_{12}(f_{7/2})^2_6(h_{9/2})^2_8\right\}$, and is stable over a large Z range, from ^{152}Gd to ^{158}Yb [98, 99, 100]. Coupled to this neutron contribution, three unpaired protons in the $h_{11/2}$ subshell will result in a negative-parity terminating state. For oblate deformation (negative ε_2) the highest possible spin is generated by filling the 3 lowest orbitals of the $h_{11/2}$ subshell, which have spin projections m_i=11/2, m_i=9/2 and m_i=7/2. This results in a spin-parity contribution from the

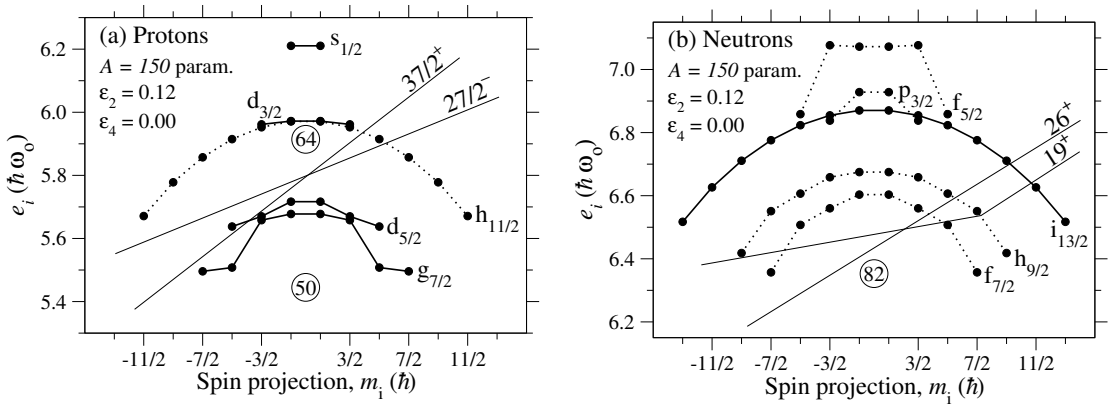

FIGURE 5.13: Tilted Fermi-surface diagrams for (a) protons and (b) neutrons at oblate shape, showing the configurations of the yrast $I^\pi = 79/2^-$ and $I^\pi = 89/2^+$ terminating states in ^{155}Ho, built from $27/2^-$ and $37/2^+$ proton configurations coupled to a 26^+ neutron configuration. The $I^\pi = 65/2^-$ favoured state of band 6 is built from the $27/2^-$ proton configuration coupled to a 19^+ neutron configuration. Adapted from Ref. [3]

protons of $27/2^+$. Occupying any higher $h_{11/2}$ or even $d_{3/2}$ orbitals would have the effect of reducing the total angular momentum. To generate higher spins, protons would need to be excited from the $d_{5/2}/g_{7/2}$ orbital, which would mean breaking the ^{146}Gd core. This terminating configuration in ^{155}Ho, which results in a fully aligned $79/2^-$ state, may be written in full as

$$\pi\{(h_{11/2})^3_{27/2}\}_{27/2^-} \otimes \nu\{(i_{13/2})^2_{12}(f_{7/2})^2_6(h_{9/2})^2_8\}_{26^+}. \tag{5.8}$$

The filling of the valence orbitals in the fully aligned $I = 79/2^-$ state is illustrated in the tilted Fermi-surface diagram [15] of Fig. 5.13. In Chapter 4, it was noted that in ^{156}Er, the favoured terminating state has $I^\pi = 42^+$, which represents the same configuration as above coupled to an extra proton in the $m_i = 5/2$ orbital of the $h_{11/2}$ subshell. It can be seen in Fig. 5.14(a) that CNS calculations for ^{155}Ho reproduce clearly the highly favoured $79/2^-$ terminating state.

The downward trend of band 6 in Fig. 5.14(b) is not completely smooth, there is a particularly favoured $I^\pi = 65/2^-$ state, the only negative-parity, $\alpha = +1/2$, yrast state above spin $\sim 30\hbar$. In addition the $67/2^-$ level is also somewhat lower

in energy than a backward extrapolation from the $79/2^-$ state would suggest. It is proposed that these states are formed at oblate shape with the spin vector of a specific valence nucleon in the opposite direction to the total spin vector [101, 102]. Relative to the fully aligned $79/2^-$ state, an $I^\pi = 65/2$ state is achieved by shifting one $f_{7/2}/h_{9/2}$ neutron from an $m_i = 7/2$ to an $m_i = -7/2$ orbital. The configuration of this $65/2^-$ state is given in Table 5.5. Likewise, the $67/2^-$ state can be formed by shifting a $f_{7/2}/h_{9/2}$ neutron from an $m_i = 5/2$ to an $m_i = -7/2$ orbital. In the tilted Fermi-surface diagram (Fig. 5.13) it is shown how the $I = 65/2^-$ state can be produced in terms of the occupation of specific orbitals, i.e. from a 19^+ neutron configuration coupled to the fully aligned $27/2^-$ proton configuration. The CNS calculations of Fig. 5.14(a) agree with experiment, in that they predict favoured $65/2^-$ and $67/2^-$ states, though experimentally the $67/2^-$ appears less favoured than in the calculations. A similar pattern of favoured angular momentum values is observed in ^{156}Er, including the corresponding configurations to the $I = 65/2, 67/2$ levels in ^{155}Ho, $7\hbar$ and $6\hbar$ below the terminating $I = 42$ state, respectively.

The strong 638 keV transition which feeds the $65/2^-$ favoured state in ^{155}Ho is notable for having a particularly low angular-distribution ratio of 0.51(3). Fitting the angular-distribution function (Eq. 3.3) for this γ ray yields $A_2 = -0.68(9)$, which indicates that the $M1/E2$ transition has a large, negative mixing ratio. In ^{157}Er there is a $77/2^-$ state which corresponds to the $65/2^-$ state in ^{155}Ho coupled to an extra $m_i = 5/2$ $h_{11/2}$ proton and an extra $m_i = 7/2$ $h_{9/2}$ neutron [104]. It too is particularly favoured and is also fed by a $M1/E2$ transition with an unusual angular-distribution coefficient of $A_2 = -0.875(15)$, indicating a large, negative mixing ratio [105].

Band 6 is not the only structure evident at high spin; there are the positive parity 'bands' labelled 7a and 7b, and a cluster of negative parity states that decay to the $79/2^-$ terminating state via the 1883 keV and 1927 keV γ rays. In terms

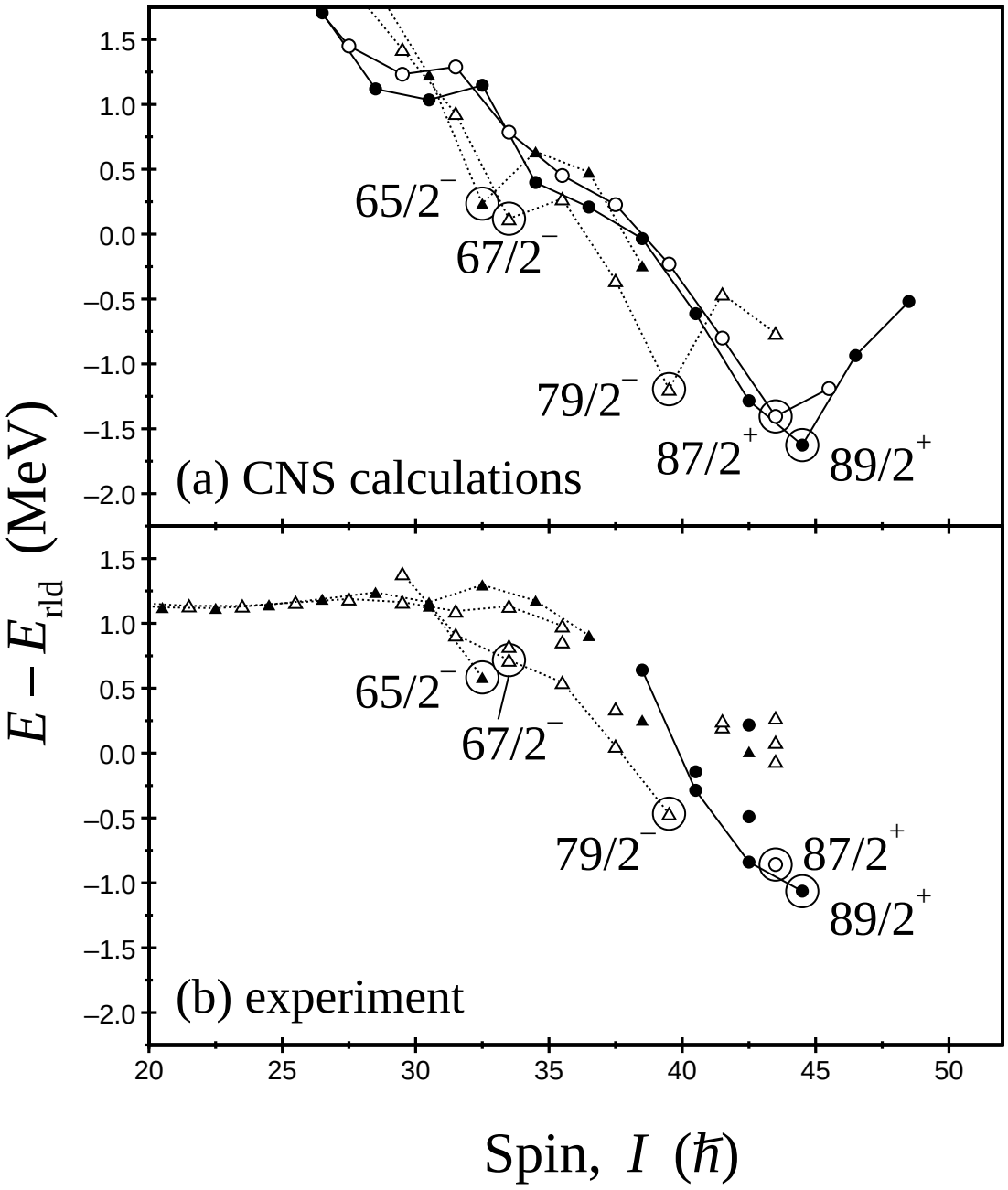

FIGURE 5.14: (a) CNS energy calculations, plotted relative to a rotating reference. For each of the four combinations of spin and parity only the one lowest in energy at high spin is shown. The energies of levels in band 2, band 6, and levels above the $79/2^-$ band termination are shown in (b), relative to a rotating reference. Positive parity is indicated by circles and solid lines, and negative parity by triangles and dotted lines. Filled and empty symbols represent $\alpha = +1/2$ and $\alpha = -1/2$ signatures, respectively.

TABLE 5.5: Observed terminating configurations in ^{155}Ho and neighbouring nuclei.

Nucleus	I^π	Aligned configuration		
^{155}Ho	$65/2^-$	$\pi\{(h_{11/2})^3_{27/2}\}_{27/2^-}$	$\otimes$	$\nu\{(i_{13/2})^2_{12}(f_{7/2})^3_{15/2}(h_{9/2})^1_{9/2}\}_{19^+}$
^{155}Ho	$79/2^-$	$\pi\{(h_{11/2})^3_{27/2}\}_{27/2^-}$	$\otimes$	$\nu\{(i_{13/2})^2_{12}(f_{7/2})^2_{6}(h_{9/2})^2_{8}\}_{26^+}$
^{155}Ho	$87/2^+$	$\pi\{(d_{5/2}/g_{7/2})^{-1}_{3/2}(h_{11/2})^4_{16}\}_{35/2^+}$	$\otimes$	$\nu\{(i_{13/2})^2_{12}(f_{7/2})^2_{6}(h_{9/2})^2_{8}\}_{26^+}$
^{155}Ho	$89/2^+$	$\pi\{(d_{5/2}/g_{7/2})^{-1}_{5/2}(h_{11/2})^4_{16}\}_{37/2^+}$	$\otimes$	$\nu\{(i_{13/2})^2_{12}(f_{7/2})^2_{6}(h_{9/2})^2_{8}\}_{26^+}$
$Z = 67$ holmium isotopes [106, 107, 89]				
^{156}Ho	41^+	$\pi\{(h_{11/2})^3_{27/2}\}_{27/2^-}$	$\otimes$	$\nu\{(i_{13/2})^2_{12}(f_{7/2})^3_{15/2}(h_{9/2})^2_{8}\}_{55/2^-}$
^{156}Ho	42^+	$\pi\{(h_{11/2})^3_{27/2}\}_{27/2^-}$	$\otimes$	$\nu\{(i_{13/2})^2_{12}(f_{7/2})^2_{6}(h_{9/2})^3_{21/2}\}_{57/2^-}$
^{157}Ho	$87/2^-$	$\pi\{(h_{11/2})^3_{27/2}\}_{27/2^-}$	$\otimes$	$\nu\{(i_{13/2})^2_{12}(f_{7/2})^3_{15/2}(h_{9/2})^3_{21/2}\}_{30^+}$
$N = 88$ isotones [11, 99, 108]				
^{154}Dy	36^+	$\pi\{(h_{11/2})^2_{10}\}_{10^+}$	$\otimes$	$\nu\{(i_{13/2})^2_{12}(f_{7/2})^2_{6}(h_{9/2})^2_{8}\}_{26^+}$
^{154}Dy	42^-	$\pi\{(d_{5/2}/g_{7/2})^{-1}_{5/2}(h_{11/2})^3_{27/2}\}_{16^-}$	$\otimes$	$\nu\{(i_{13/2})^2_{12}(f_{7/2})^2_{6}(h_{9/2})^2_{8}\}_{26^+}$
^{154}Dy	48^+	$\pi\{(d_{5/2}/g_{7/2})^{-2}_{6}(h_{11/2})^4_{16}\}_{22^-}$	$\otimes$	$\nu\{(i_{13/2})^2_{12}(f_{7/2})^2_{6}(h_{9/2})^2_{8}\}_{26^+}$
^{156}Er	42^+	$\pi\{(h_{11/2})^4_{16}\}_{16^+}$	$\otimes$	$\nu\{(i_{13/2})^2_{12}(f_{7/2})^2_{6}(h_{9/2})^2_{8}\}_{26^+}$
^{156}Er	46^+	$\pi\{(d_{5/2}/g_{7/2})^{-1}_{5/2}(h_{11/2})^4_{16}(d_{3/2})^1_{3/2}\}_{20^+}$	$\otimes$	$\nu\{(i_{13/2})^2_{12}(f_{7/2})^2_{6}(h_{9/2})^2_{8}\}_{26^+}$

of rearranging protons, the simplest way of achieving greater angular momentum than 79/2 is to excite a proton across the $Z = 64$ shell gap from a $d_{5/2}/g_{7/2}$ orbital, which lies closest to the Fermi surface, to a vacant orbital in the $h_{11/2}$ subshell. This necessarily involves a change in parity, which is why it is suggested the structures labelled 7a and 7b have positive-parity. The spin-parity assignments for the structures labelled 7a and 7b are tentative, some transitions being too weakly populated to perform an angular-correlation analysis. However, the decay to band 6 and the angular-distribution ratios that have been extracted are consistent with 7a and 7b being positive parity, terminating at a $(89/2^+)$ state.

If the assignments are correct, then band 7 most likely represents a particle-hole excitation across the $Z = 64$ shell gap, $\pi(d_{5/2}/g_{7/2} \rightarrow h_{11/2})$. When their energies are plotted relative to a rotating reference, both 7a and 7b slope downward, terminating

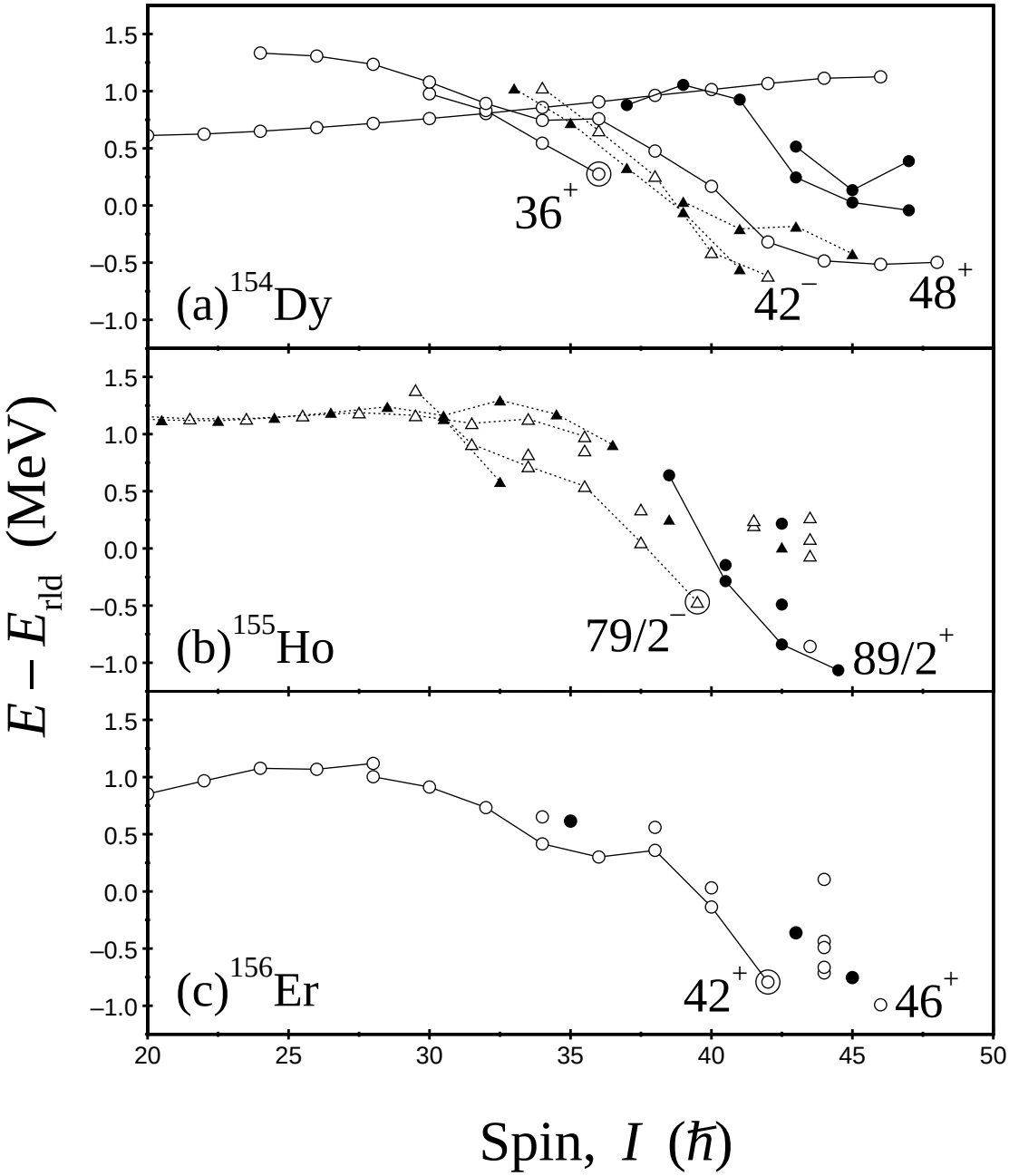

FIGURE 5.15: Energy plotted relative to a rotating liquid-drop reference, E_{rld} for (a)^{154}Dy, (b)^{155}Ho and (c)^{156}Er. Only selective states are shown for all three nuclei (i.e. states near valence-space band termination).

at favoured $(87/2^+)$ and $(89/2^+)$ states. The configuration of the terminating $89/2^+$ state is given in Table 5.5. Specifically, relative to the $79/2^-$ valence-space terminating state, the $89/2^+$ state represents a proton being excited from an $m_i = -5/2$ $d_{5/2}/g_{7/2}$ state to the $m_i = 5/2$ state of the $h_{11/2}$ subshell, and results in an additional spin contribution of $5\hbar$. The resulting $37/2^+$ proton configuration is shown in the tilted Fermi-surface diagram, Fig. 5.13(a). The calculations of Fig. 5.14(a) show particularly favoured terminating $87/2^+$ and $89/2^+$ states.

In the negative-parity level scheme, there are two at $I^\pi = 83/2^-$ states that lie almost 2 MeV above the $79/2^-$ terminating state, decaying to the $79/2^-$ state via the 1883 and 1927 keV γ rays. Above the $83/2^-$ states there are at least two $87/2^-$ states, another of spin 85/2, and a fourth which has tentatively been assigned as $(87/2^-)$. In the discussion of structures 7a and 7b, it was noted that the easiest way to generate spins greater than 79/2 involves exciting a single proton from the $d_{5/2}/g_{7/2}$ subshell to the lowest vacant $h_{11/2}$ orbital, necessarily involving a change of parity. The negative parity states above the $79/2^-$ state, which lie more than 500 keV higher in energy than their positive-parity counterparts, may then correspond to less favoured excitations, such as two protons being excited from the $d_{5/2}/g_{7/2}$ subshell to $h_{11/2}$ orbitals, or a single proton being excited to the $d_{3/2}$ subshell, or similarly energetically expensive rearrangements of the neutrons.

Possible favoured configurations in band 5

In ^{155}Ho, band 5 is also thought to represent a prolate-oblate shape transition, culminating in a favoured $71/2^+$ state. Above this is a less obviously favoured $(73/2^+)$ state. A proposed terminating configuration is the $I^\pi = 27/2^-$ proton configuration coupled to a negative-parity $I^\pi = 22, 23^-$ neutron configuration, which can be expressed as $\nu\{(h_{9/2}/f_{7/2})^5_{31/2,33/2}(i_{13/2})^1_{13/2}\}_{22,23^-}$. This corresponds to two positive-parity $I = 71/2, 73/2$ terminating states. Coupled to an extra proton in the

$m_i = 5/2$ orbital of the $h_{11/2}$ subshell, these become the predicted negative-parity $I = 38, 39$ terminating states in ^{156}Er, of which only the spin 38 state has been experimentally verified [3].

Comparison to neighbouring N=88 isotones

In Fig. 5.15 the energies relative to a rotating reference of the highest spin negative-parity ^{155}Ho states are plotted alongside the positive-parity levels in ^{154}Dy and ^{156}Er at valence-space band termination. The $79/2^-$ terminating state of ^{155}Ho has been indicated. For comparison, the favoured positive-parity terminating state in ^{156}Er, at $I^\pi = 42^+$ is also shown, which represents the same configuration coupled to an extra proton in the $m_i = 5/2$ orbital of the $h_{11/2}$ subshell. Similarly, the 36^+ level in ^{154}Dy has been indicated, which represents the $79/2^-$ ^{155}Ho configuration with one less m_i=7/2 $h_{11/2}$ proton. The configurations of these states, relative to the doubly magic ^{146}Gd core, are given in full in Table 5.5.

5.3 Conclusions

A high-statistics, high-spin experiment has been performed to study the level structure of the $^{155-157}$Ho nuclei. Many previously unreported γ-ray transitions have been established in ^{155}Ho and a comprehensive level scheme has been built from high-fold coincidence analysis. At low spin, a positive-parity $\pi g_{7/2}$ rotational band, observed for the first time in this nucleus, has been established up to $(33/2^+)$. The more favoured (and well established) $\pi h_{11/2}$ band has been extended to $I^\pi = 57/2^-$. A positive-parity rotational structure has been established to $I^\pi = 57/2^-$ and interpreted as being based on a $\nu(i_{13/2}h_{9/2})$ structure coupled to the $h_{11/2}$ proton. $B(M1)/B(E2)$ ratios of reduced transition probabilities have been calculated from observed branching ratios for all three bands and compared to geometric model calculations for specific particle configurations. While these are mostly in agreement, the $B(M1)/B(E2)$ ratios measured for the $\pi(h_{11/2}) \otimes \nu(i_{13/2}h_{9/2})$ band exhibit a striking signature dependence, which cannot be fully explained by the observed energy-splitting between the $\alpha = +1/2$ and $\alpha = -1/2$ signature components.

The $\pi h_{11/2}$ configuration has been discussed as favouring a negative-γ triaxial deformation, which gives rise to the considerable signature splitting in the band up to spin ~ 15, at which point it is quenched by the $(\nu i_{13/2})^2$ alignment. Comparisons to the staggering of $\pi h_{11/2}$ bands in neighbouring isotopes and isotones show that this effect is common to many nuclei in this region, and that the effect is diminished with increasing N.

Above spin $\sim 59/2$ band termination in ^{155}Ho has been investigated. Several energetically favoured terminating states built on specific particle configurations were identified, including a state at $I^\pi = 79/2^-$, which corresponds to valence-space band termination in ^{155}Ho. Relative to the ^{146}Gd core the full configuration of this

state can be written as

$$\pi\{(h_{11/2})^3_{27/2}\}_{27/2^-} \otimes \nu\{(i_{13/2})^2_{12}(f_{7/2})^2_6(h_{9/2})^2_8\}_{26^+}.$$

Positive-parity states of higher spin and excitation energy are thought to correspond to further predicted favoured states at oblate deformation, with $I^\pi = 87/2^+, 89/2^+$. These are built on $\pi(d_{5/2}/g_{7/2} \rightarrow h_{11/2})$ particle-hole excitations across the $Z = 64$ shell gap, and their full configurations are

$$\pi\{(d_{5/2}/g_{7/2})^{-1}_{3/2,5/2}(h_{11/2})^4_{16}\}_{25/2^-,27/2^-} \otimes \nu\{(i_{13/2})^2_{12}(f_{7/2})^2_6(h_{9/2})^2_8\}_{26^+}.$$

The observed favoured states are in agreement with those predicted by the Cranked Nilsson Strutinsky calculations.

Two negative-parity 83/2 states have been established almost 2 MeV above the $79/2^-$ terminating state, and decay to the $79/2^-$ state via two 1883 and 1927 keV γ rays. Above the $83/2^-$ states there are at four further negative-parity states, with spins as high as 87/2. It is proposed these negative-parity levels above the $79/2^-$ terminating state are generated by more energetically expensive excitations than the positive-parity levels, such as two protons being excited from the $d_{5/2}/g_{7/2}$ subshell to $h_{11/2}$ orbitals, a single proton being excited from the $d_{5/2}/g_{7/2}$ subshell to the higher $d_{3/2}$ subshell, or similarly energetically expensive rearrangements of the neutrons.

Up to this point, the γ-soft behaviour exhibited by ^{156}Er (Chapter 4), and the band termination seen in both nuclei have been treated quite separately. After all, the theoretical approach to each is very different, relating to collective rotation-vibration models in the first case and specific Nilsson orbitals of the shell model in the second. The argument for γ-softness in ^{156}Er rested on the relative energies of the low spin levels, while the evidence for band termination in ^{156}Er and ^{155}Ho concerns

levels of the highest observed spins in these nuclei. There are, however, similarities between the two phenomena. Both γ-softness and the favoured band terminations have been discussed here in terms of the few (nine or ten) valence nucleons outside the ^{146}Gd core. In Chapter 4, ^{156}Er was said to exist in a 'transitional' region where nuclear collectivity changes from vibrational (near the spherical core) to rotational (towards mid-shell regions). With band termination, the number of valence nucleons determines the maximum spin that can be achieved without breaking the core. At higher values of N and Z terminating states are predicted to become less favoured, shell effects becoming less dominant.

It can be seen in the calculated potential energy surfaces of Fig. 4.13 how, in ^{156}Er, competition between oblate-favouring single-particle configurations and prolate-favouring rotational structures can result in a potential markedly soft to γ-deformation. This accounts for the γ-soft behaviour observed in ^{156}Er at low spin and, when a critical spin ($\sim$ 30) is reached, the transition from prolate-deformed rotational behaviour to oblate-deformed single-particle behaviour at terminating states in ^{156}Er and ^{155}Ho.

Bibliography

[1] G. B. Hagemann, J. D. Garrett, B. Herskind, J. Kownacki, B. M. Nyako, P. L. Nolan, J. F. Sharpey-Schafer, P. O. Tjom, Nucl.Phys. **A424**, 365 (1984).

[2] C. W. Beausang and J. Simpson, J. Phys. G. Nucl. Part. Phys. **22**, 527 (1996).

[3] E. S. Paul *et al.*, Phys. Rev. C **79**, 044324 (2009).

[4] J. M. Rees *et al.*, Phys. Rev. C **83**, 044314 (2011).

[5] A. V. Afanasjev, D. B. Fossan, G. J. Lane, and I. Ragnarsson, Phys. Rep. **322**, 1 (1999).

[6] I. Ragnarsson, V. P. Janzen, D. B. Fossan, N. C. Schmeing, and R. Wadsworth, Phys. Rev. Lett. **74**, 3935 (1995).

[7] T. Bengtsson and I. Ragnarsson, Phys. Scr. **T5**, 165, (1983).

[8] C. Baktash *et al.*, Phys. Rev. Lett. **54**, 978 (1985).

[9] I. Ragnarsson, T. Bengtsson, W. Nazarewicz, J. Dudek, and G. A. Leander, Phys. Rev. Lett. **54**, 982 (1985).

[10] J. Dudek and W. Nazarewicz, Phys. Rev. C **31**, 298 (1985).

[11] H. W. Cranmer-Gordon *et al.*, Nucl. Phys. **A465**, 506 (1987).

[12] A. O. Evans *et al.*, Phys. Rev. Lett. **92**, 252502 (2004).

[13] M. A. Riley *et al.*, Phys. Scr. **T125**, (2006).

[14] F. Dönau and S. Frauendorf, Proc. Conf. on high angular momentum properties of nuclei, Oak Ridge, Tenn., 1982, ed. N.R. Johnson (Harwood Academic, New York, 1983); F. Dönau, Nucl. Phys. A **471**, 469 1987).

[15] G. Andersson, S. E. Larsson, G. Leander, P. Moller, S. G. Nilsson, I. Ragnarsson, S. Aberg, R. Bengtsson, J. Dudek, B. Nerlo-Pomorska, K. Pomorski, and Z. Szymanski Nucl. Phys. **A268**, 205 (1976).

[16] K. F. Krane, *Introductory Nuclear Physics* (Wiley, 1988).

[17] W. Nazarewicz, J. Dudek, R. Bengtsson, and I. Ragnarsson, Nucl. Phys. **A435**, 397 (1985).

[18] S. Cwiok, J Dudek, W. Nazarewicz, W. Skalski, and T. Werner, Comp. Phys. Comm. **46**, 379 (1987).

[19] M. G. Mayer, Phys. Rev. **75**, 1969 (1949).

[20] O. Haxel, J. H. D. Jensen and H. E. Suess, Phys. Rev. **75**, 1766 (1949).

[21] R. Bengtsson, Nucl. Phys. **A512**, 124 (1990).

[22] R. F. Casten, *Nuclear Structure from a Simple Perspective* (Oxford University Press, 1990).

[23] S. G. Nilsson and I. Ragnarsson, *Shapes and Shells in Nuclear Structure*, (Cambridge University Press, 1995).

[24] S. G. Nilsson *et al.*, Nucl. Phys. **A31** 1 (1969).

[25] D. R. Inglis, Phys. Rev. **96**, 1059 (1954).

[26] A. Bohr and B. R. Mottelson, *Nuclear Structure, Vol. II* (Benjamin, 1975).

[27] R. Bengtsson and S. Frauendorf, Nucl. Phys. **A327**, 139 (1979).

[28] R. Bengtsson, S. Frauendorf, and F. R. May, At. Data Nucl. Data Tables **35**, 15 (1986).

[29] P. Möller, J. R. Nix, W. D. Myers and W. J. Swiatecki, Atomic Data Nucl. Data Tables **59**, 185(1995).

[30] R. Bengtsson *et al.*, Phys. Lett. B **57**, 301 (1975).

[31] S. M. Harris, Phys. Rev. **138**, B509 (1965).

[32] R. Bengtsson and I. Ragnarsson, Nucl. Phys. **A436**, 14 (1985).

[33] B. G. Carlsson and I. Ragnarsson, Phys. Rev. C **74**, 011302(R) (2006).

[34] E. S. Paul, Postgraduate lecture notes, University of Liverpool (2010).

[35] A. S. Davydov and G. F. Filippov, Nucl. Phys. **8**, 237 (1958).

[36] L. Wilets and M. Jean, Phys. Rev. **102**, 788 (1956).

[37] R. F. Casten, P .Von Brentano, K. Heyde, P. Van Isacker, and J. Jolie, Nucl. Phys. A **439**, 289 (1985).

[38] C. Baktash *et al.*, Phys. Rev. C **18**, 131 (1978).

[39] N. V. Zamfir and R. F. Casten, Phys. Lett. B **260**, 265 (1991).

[40] A. Bohr and B. R. Mottelson. *Nuclear Structure, Vol. I* (World Scientific, 1998).

[41] H. Ejiri and M. J. A. de Voigt, *Gamma-Ray and Electron Spectroscopy in Nuclear Physics* (Oxford University Press, 1989).

[42] J. R. Grover. Phys. Rev. **157**, 832 (1967).

[43] A. Gavron, Phys. Rev. C **21**, 230 (1980).

[44] O. B. Tarasov and D. Bazin, Nucl. Instrum. and Methods Phys. Res. B **204**, 174 (2003).

[45] I. Y. Lee, Nucl. Phys. A **520**, 641c (1990).

[46] I. Y. Lee, Prog. Part. Nucl. Phys. **38** 65 (1997).

[47] M. A. Riley, *Gammasphere Online Booklet Homepage*, Florida State University Physics Department, `http://nucalf.physics.fsu.edu/~riley/gamma` (Accessed 2013).

[48] D. C. Radford, Nucl. Instrum. and Methods Phys. Res. A **361**, 297 (1995).

[49] D. C. Radford, M. Cromaz, and C. J. Beyer, in *Proceedings of the Nuclear Structure '98 Conference, Gatlinburg, 1998*, edited by C. Baktash (American Institute of Physics CP481, 1999), p. 570.

[50] J. Cresswell, *Event Format [Sorting + Storage] - EDOC073*, 2001.

[51] D. C. Radford, Nucl. Instrum. and Methods Phys. Res. A **361**, 306 (1995).

[52] J. Cresswell and J. Sampson, *MTsort Language - EDOC033*, 2009.

[53] C. W. Beausang *et al.*, Nucl. Instrum. Methods Phys. Res. A **364**, 560 (1995).

[54] D. C. Radford, *Notes on the use of the program gf3*, RADWARE site, Oak Ridge National Laboratory, `http://radware.phy.ornl.gov/gf3` (Accessed 2013).

[55] E. S. Paul *et al.*, Phys. Rev. Lett. **98**, 012501 (2007).

[56] P. J. Nolan and J. F. Sharpey-Schafer, Rep. Prog. Phys. **42**, 1 (1979).

[57] K. Schiffer, B. Herskind, and J. Gascon, Z. Phys. A **332**, 17 (1989).

[58] T. Yamazaki, Nucl. Data A **3**, 1 (1967).

[59] E. Der Mateosian and A. W. Sunyar, At. Data Nucl. Data Tables **13**, 391 (1974).

[60] R. F. Casten, D. D. Warner, D. S. Brenner, and R. L. Gill, Phys. Rev. Lett. **47**, 1433 (1981).

[61] A. Faessler and W. Greiner, Z. Phys. **168**, 425 (1962).

[62] X. Wang *et al.*, Phys. Lett. B **702**, 127 (2011).

[63] J. P. Revill *et al.*, Phys. Rev. C **88**, 031304(R) (2013).

[64] P. Aguer, C. F. Liang, J. Libert, P. Paris, A. Peghaire, A. Charvet, R. Duffait, and G. Marguier, Nucl. Phys. A **252**, 293 (1975).

[65] C. W. Reich, Nucl. Data Sheets **99**, 753 (2003), and references therein.

[66] D. R. Zolnowski, M. B. Hughes, J. Hunt, and T. T. Sugihara, Phys. Rev. C **21**, 2556 (1980).

[67] J. Jolie, R. F. Casten, P. Cejnar, S. Heinze, E. A. McCutchan, and N. V. Zamfir, Phys. Rev. Lett. **93**, 132501 (2004).

[68] O. Scholten, F. Iachello, and A. Arima, Ann. Phys. (NY) **115**, 325 (1978).

[69] J. A. Sheikh, G. H. Bhat, Y. Sun, G. B. Vakil, and R. Palit, Phys. Rev. C **77**, 034313 (2008).

[70] P. E. Garrett, J. Phys. G **27**, R1 (2001).

[71] I. Ragnarsson and R. A. Broglia, Nucl. Phys. A **263**, 315 (1976).

[72] J. F. Sharpey-Schafer *et al.*, Nucl. Phys. A **834**, 45c (2010).

[73] J. F. Sharpey-Schafer *et al.*, Eur. Phys. J. A **47**, 5 (2011).

[74] J. F. Sharpey-Schafer, T. E. Madiba, S. P. Bvumbi, E. A. Lawrie, J. J. Lawrie, A. Minkova, S. M. Mullins, P. Papka, D. G. Roux, and J. Timar, Eur. Phys. J. A **47**, 6 (2011).

[75] Evaluated Nuclear Structure Data File, National Nuclear Data Center, Brookhaven National Laboratory, `http://www.nndc.bnl.gov/ensdf` (Accessed 2013).

[76] I. Ragnarsson and B. G. Carlsson. *Calculating high-spin states using the configuration-dependent cranked Nilsson-Strutinsky (CNS) formalism.* Private communication, 2013.

[77] K. Dusling *et al.*, Phys. Rev. C **73**, 014317 (2006).

[78] G. D. Dracoulis *et al.*, Phys. Rev. C **81**, 054313 (2010).

[79] E. A. McCutchan, N. V. Zamfir, and R. F. Casten, Phys. Rev. C **69**, 064306 (2004).

[80] C. Baktash *et al.*, Phys. Rev. C **18**, 131 (1978).

[81] J. Simpson *et al.*, J. Phys. G: Nucl. Phys. **12**, L67 (1986).

[82] G. D. Dracoulis, B. Fabricius, P. M. Davidson, A. O. Macchiavelli, J. Oliviera, J. Burde, F. Stephens, and M. A. Deleplanque, in *International Conference on Nuclear Structure at High Angular Momentum, Ottawa, 1992* (AECL-10613, 1992) Vol 2, p. 94.

[83] J. Thomson *et al.*, Phys.Rev. C **81**, 014307 (2010).

[84] K. Lagergren *et al.*, Phys. Rev. C **83**, 014313 (2011).

[85] C. W. Reich, Nucl. Data Sheets **104**, 1 (2005), and references therein.

[86] C. Foin, S. Andre, D. Barneoud, J. Boutet, G. Bastin, M. G. Desthuilliers, J. P. Thibaud, Nucl. Phys. **A324**, 182 (1979).

[87] H. Helppi, D. C. Radford, R. Holtzmann, R. V. F. Janssens, T. L. Khoo, R. Broda, P. J. Daly, Z. Grabowski, Proceedings Intern. Nucl. Phys. Conf., Harrogate, UK p115 (1986).

[88] J. P. Torres, P. Paris, D. Lecouturier and P. Kilcher, Nucl. Phys. **A189**, 609 (1972).

[89] D. C. Radford *et al.*, Nucl. Phys. A. **545**, 665-719 (1992).

[90] E. S. Paul *et al.*, J. Phys. G. **17**, 605-617 (1991).

[91] A. J. Kreiner, M. A. J. Mariscotti, C. Baktash, E. der Mateosian, and P. Thieberger, Phys. Rev. C **23**, 748 (1981).

[92] S. Frauendorf and F. R. May, Phys. Lett. B. **125**, 245 (1983).

[93] Ma Yingjun *et al.*, J. Phys. G: Nucl. Part. Phys. **21**, 937 (1995).

[94] Ma Ying-Jun *et al.*, J. Phys. G: Nucl. Part. Phys. **26**, 43 (2000).

[95] R. Holzmann, M. Loiselet, M. A. Van Hove and J. Vervier, Phys. Rev. C **31**, 421 (1985).

[96] D. J. Hartley *et al.*, Phys. Rev. C **58**, 1321 (1998).

[97] M. A. Riley *et al.*, Phys. Rev. C **51**, 1234 (1995).

[98] D. B. Campbell *et al.*, Phys. Rev. C **75**, 064314 (2007).

[99] W. C. Ma *et al.*, Phys. Rev. C **65**, 034312 (2002).

[100] S. B. Patel, F. S. Stephens, J. C. Bacelar, E. M. Beck, M. A. Deleplanque, R. M. Diamond, and J. E. Draper, Phys. Rev. Lett. **57**, 62 (1986).

[101] I. Ragnarsson and T. Bengtsson, Nucl. Phys. **A447**, 251 (1985).

[102] I. Ragnarsson, Z. Xing, T. Bengtsson, and M. A. Riley, Phys. Scr. **34**, 651 (1986).

[103] I. Ragnarsson, Lund Institute of Technology, private communication (2003).

[104] S. J. Gale *et al.*, J. Phys. G **21**, 193 (1995).

[105] A. O. Evans *et al.*, Phys. Rev. C **73**, 064303 (2006).

[106] D. M. Cullen *et al.*, Phys. Rev. C **57**, 2170 (1998).

[107] P. Hampson *et al.*, (unpublished).

[108] F. S. Stephens, M. A. Deleplanque, R. M. Diamond, A. O. Macchiavelli, and J. E. Draper, Phys. Rev. Lett. **54**, 2584 (1985).